Hydrodynamics of colloidal ellipsoids and helices under shear flow and active deformation

Inaugural-Dissertation

zur
Erlangung des Doktorgrades
der Mathematisch-Naturwissenschaftlichen Fakultät
der Universität zu Köln
vorgelegt von

Run Li
aus Bijie, China

Köln
2019

Berichterstatter: **Prof. Dr. Gerhard Gompper**

(Gutachter) **Prof. Dr. Matthias Sperl**

Dr. Marisol Ripoll

Tag der mundlichen Prufung: 6. May 2019

Abstract

Colloidal suspensions widely exit in our daily life, in the form of food, medicaments, biological materials, or cosmetics, among other examples. Hydrodynamic interactions in colloids suspensions at non-equilibrium give rise to many intriguing phenomena, where the shape of colloidal particles plays an important role. For instance, colloidal ellipsoids tumble and kayak in shear flow. Flexible polymers deform, or multicomponent systems in various phases. Besides the tumbling of elongated colloids, further characteristics are expected in shear flow when the particles are chiral, like a helical structures which display a drift in the vorticity direction. Furthermore, the helix may generate locomotion, when external actuation is able to deform its shape in non-reciprocal ways. Artificial systems have been recently synthesized showing that it is possible to generate net motion by smoothly deforming their helical body, as a response to changing temperature.

We combine a theoretical approach based on the Smoluchowski equation and flow-dichroism experiments to measure hydrodynamic aspect ratios and polydispersity of nano particles, which is not feasible with standard methods similar to light scattering. A mesoscale hydrodynamics simulations are used to study the transport of helix in shear flow and swimming of deformable helix at low Reynolds numbers. The particle-based approach of multi-particle collision dynamics also enables simulations of colloids at non-equilibrium where thermal fluctuations are not negligible.

The first part of tis thesis investigates the validity of flow dichroism as a characterization tool by employing dispersions of prolate and oblate quantum dots (QDs). Flow dichroism quantifies the tumbling motion of QDs in shear flow by optical means, which provides a characteristic signature of the particle shape, hydrodynamic friction, and size distribution. Particle size, shape, polydispersity, and shear rate have an important effect on the temporal evolution of the flow-induced alignment which we discuss in detail on the basis of numerical solutions of the Smoluchowski equation describing the QDs motion in the basis of the probability of the orientation of colloids in shear flow. This combination of flow dichroism and the Smoluchowski equation approach is not only useful for determining shape and anisotropic of colloidal QDs, but also for other nanoscale systems.

The second part of this thesis discusses the transport of a deformable helical polymer in a uniform shear flow. The rigidity of the helix essentially affects its configuration under shear stress. The deformable structure still keep helicity while it is compressed and stretched periodically (breathing), and tumble simultaneously in the shear flow below certain shear stress, above which the helix performs noticeable chaotic motion. The tumbling motion follows Jefferys theory for rigid rod-like particles, although with an effective aspect ratio value which depends on flexibility and chirality parameters. The lateral drift shows to be a hydrodynamic effect with a maximum impact between rod and tube limits, obtained by changing the geometry of rigid helix. The flexibility also plays an important role on the lateral drift because its geometry and chirality keep changing.

Finally, we investigate the transport of a perfectly deforming helix interacting with a viscous fluid by hydrodynamic simulations. Maintaining the helical structure and a single

handedness along its entire length, we first discuss how the deformation periods, helix configuration, and fluid viscosity impact the net rotational swimming stroke and identify its principle direction of motion. We then explore how the presence of confinement in a planar slit influences the rotation speed, trajectory, and position of the deformable helix. Interestingly the active helix shows to consistently migrate to the channel center while passive helix and helix with reciprocal deformation do not show significant migration in any direction. These results including second part provide important criteria to consider in the design and optimization of helical machines at the nanoscale, and in the understanding of some biological functions, for example of flagellated structures.

In summary, non-equilibrium dynamics of anisotropic colloids are studied, which include rods and helices in shear flow, and actuated helices. These results show the importance of shape anisotropy in hydrodynamics of colloidal suspensions, which has significant potential in practical applications and solution of some fundamental questions.

Zusammenfassung

Wir begegnen in unserem täglichen Leben häufig kolloiden Suspensionen in Form von Essen, Medikamenten, biologischen Materialien oder Kosmetik. Hydrodynamische Wechselwirkungen in kolloiden Suspensionen rufen außerhalb des Gleichgewichtszustandes viele faszinierende Phänomene hervor, wobei die Form des kolloiden Teilchens eine wichtige Rolle spielt. Beispiele hierfür sind das Taumeln ellipsoidaler Kolloide und die Paddelbewegung in Scherströmungen. Flexible Polymere verformen sich und Systeme, die aus mehreren Komponenten bestehen, ergeben verschiedene Phasen. Weitere Merkmale neben der Taumelbewegung werden in Scherströmungen erwartet, wenn das Teilchen eine spiralförmige Struktur besitzt. Ein Beispiel hierfür ist ein Drift in Vertizitätsrichtung. Die Helix kann Bewegung erzeugen, wenn äußere Kräfte ihre Form nicht zu sehr deformieren. Helikale Kolloide wurden kürzlich synthetisiert und zeigen eine Netto-Bewegung durch reibungsloses Verformen der Helix als Reaktion auf Temperaturänderung.

In dieser Arbeit verbinden wir einen theoretischen Ansatz basierend auf der Smoluchowski Gleichung mit den Messungen der Experimente zum Flussdichroismus. Dabei ist das Ziel, hydrodynamische Seitenverhältnisse und Polydispersität von Nanopartikeln zu vergleichen, welche nicht mit Standardmethoden wie den Lichtstreuverfahren umsetzbar sind. Mesoskale hydrodynamische Methoden werden verwendet, um den Transport einer Helix in einer Scherströmung und das Schwimmen einer verformbaren Helix bei niedrigen Reynolds-Zahlen zu simulieren. Der teilchen-basierte Ansatz der Vielteilchenkollisionsdynamik ermöglicht Simulationen eines Kolloids im Nichtgleichgewichtszustand, wobei thermische Fluktuationen nicht vernachlässigbar sind.

Im ersten Teil dieser Arbeit wird die Dispersion von Stäbchen und scheibenförmigen quantum dots (QDs) als Modellsystem eingesetzt, um die Gültigkeit des Flussdichroismus zu untersuchen. Flussdichroismus quantifiziert die Taumelbewegung von QDs in Scherströmungen durch optische Methoden, welche charakteristische Eigenschaften wie die Teilchenform, die hydrodynamische Reibung und die Verteilung der Teilchengröße bestimmen lassen. Teilchengröße, Form, Polydispersität und Scherrate haben einen wichtigen Einfluss auf die zeitliche Entwicklung der strömungsinduzierten Ausrichtung. Dies wird auf Basis der numerischen Lösung der Smoluchowski Gleichung, welche die zeitliche Änderung der Wahrscheinlichkeit der Orientierung von Kolloiden in Scherströmungen beschreibt, ausführlich erörtert. Diese Verbindung von Flussdichroismus und dem Ansatz der Smoluchowski Gleichung wird nicht nur für die Bestimmung der Form und der Anisotropie von kolloiden QDs, sondern ebenfalls für Systeme im Nanobereich, nützlich sein.

Im zweiten Teil der Arbeit untersuchen wir den Transport eines verformbaren und spiralförmigen Polymers in einer gleichförmigen Scherströmung. Die Steifheit der Helix beeinflusst im Wesentlichen ihre Konfiguration unter Scherung. Die verformbare Struktur behält ihre spiralförmige Gestalt solange sie periodisch zusammengedrückt und gestreckt wird (breathing) und taumelt gleichzeitig in der Scherströmung unterhalb einer bestimmten Strömungsspannung. Oberhalb dieser Spannung zeigt die Helix

chaotisches Verhalten. Die Taumelbewegung folgt weiterhin der Jeffery Theorie für rigide stäbchenförmige Teilchen, wenn auch mit einem effektivem Wert für das Seitenverhältnis, welcher von der Flexibilität und dem Chiralitätsparameter abhängig ist. Der laterale Drift zeigt sich als hydrodynamischer Effekt mit einer maximalen Auswirkung zwischen den Grenzwerten von Stab und Rohr, welche durch die Änderung der Helixgeometrie erhalten werden. Die Flexibilität spielt ebenfalls für den lateralen Drift eine wichtige Rolle, da sich Geometrie and Chiralität stetig ändern.

Inspiriert von diesen Systemen untersuchen wir den Transport einer sich ideal verformenden Helix in einer viskosen Flüssigkeit mit hydrodynamischen Simulationen. Die spiralförmige Struktur und die Händigkeit wird entlang ihrer ganzen Länge aufrecht erhalten, um zu diskutieren wie sich die Perioden der Verformung, die Helix-Konfiguration und die Viskosität der Flüssigkeit auf die Netto- Rotation eines Schwimmschlags auswirken und um die prinzipielle Bewegungsrichtung zu identifizieren. Wir untersuchen daraufhin, wie sich eine einschränkende Geometrie in Form eines Spaltes auf die Rotationsgeschwindigkeit, die Trajektorie und die Position der verformbaren Helix auswirken. Interessanterweise wandert die aktive Helix durchgängig zum Zentrum des Kanals, während eine passive Helix und eine Helix mit wechselseitigen Verformungen keine wesentliche Bewegung in eine ausgezeichnete Richtung zeigen. Diese Ergebnisse bieten ein wichtiges Kriterium für die Gestaltung und die Optimierung spiralförmiger Kolloide im Nanobereich und ein Verständnis biologischer Funktionen wie zum Beispiel die gegeoßelter Strukturen.

Es wurde die Nichtgleichgewichtsdynamik von anisotropen Kolloiden studiert, welche Stäbe und Helices in Scherströmung beinhalten. Die Ergebnisse heben die Bedeutung von anisotropen Formen in der Hydrodynamik von kolloiden Suspensionen hervor, welche großes Potential in der praktischen Anwendung und Lösung grundlegender Fragestellungen haben.

Contents

List of Figures

List of Tables

Nomenclature

Greek Symbols

α	Stochastics rotation angle
α_h	Helix angle
χ_s	Orientation angle
$\dot{\gamma}$	Shear rate
η_s	Viscosity
$\kappa_{\text{bond}}, \kappa_{\text{bend}}, \kappa_{\text{tors}}$	Bond, bending, torsional force constants
μ	Kinetic viscosity
ω	Angular velocity
ϕ	Phase between the two oscillations
σ	Degree of polydispersity
τ	Torsional angle
θ	Bending angle

Matrix or tensors

Γ	Gradient velocity tensor
$\hat{\Re}$	Rotational Operator
$\hat{\mathbf{I}}$	Identity tensor
Ω	Velocity gradient tensor of simple shear flow
σ_s	Stress tensor

$\mathbf{T}$ Deviatic stress tensor

E Velocity gradient tensor of elongational flow

G Velocity gradient tensor

Roman Symbols

$2l$ Total length of helix

$\mathbf{U}_{LJ}$ Lennard-Jones potential

$\mathbf{X}$ Location of monomer

c Pitch of helix

C_T, C_N Coefficient of drag forces

D_r Rotational diffusion coefficient

$D_{\parallel}$ Parallel diffusion coefficient

$D_{\perp}$ Perpendicular diffusion coefficient

f Deformation frequency of helix

h Collision time step

L_e End-to-end length of helix

M Mass of monomer

m Mass of solvent particle

p Aspect ratio of rod

$P(\mathbf{r}, t)$ Probability density function

Pe_r Peclet number

Pe_r Pressure

R Radius of helix

Re Reynolds number

s Arc length of helix

T Tumbling period

t time

T_H Deformation period of helix

$W_{\hat{\mathbf{u}}}(t)$ Mean-squared displacement

Vectors

$\hat{\mathbf{u}}$ Long axis of particle

$\hat{\mathbf{v}}$ Velocity of particle

$\hat{\mathbf{v}}_{\parallel}$ Parallel component of velocity of particle

$\hat{\mathbf{v}}_{\perp}$ Perpendicular component of velocity of particle

$\mathbf{D}$ Diffusion tensor

$\mathbf{F}_s, \mathbf{F}_h, \mathbf{F}_{Br}$ Force

$\mathbf{g}$ Pressure tensor

$\mathbf{M}_{\theta}$ Strength of the vector field

$\mathbf{r}$ Position of particle

$\mathbf{U}$ Flow velocity

Chapter 1

Introduction

Colloidal suspensions are systems of particles immersed in a solvent, also commonly referred to as *complex fluids*, in which the solute particles move significantly slower than the solvent particles. As shown in Fig 1.1, the sizes of the colloidal particles roughly range from a few nanometers up to the micrometer scale, whereas typical solvent molecules, such as water, are in the Ångström range. In the early day of condensed-matter physics, the observation of the undirected and seemingly erratic motion of colloidal particles has led to a strong backing of the atom hypothesis [1, 2]. As discussed in Ref. [3], "It has allowed calculation of the size and number of molecules driving the *Brownian motion* [4]. Despite the undirected and irregular nature of the movements, Einsteins and Smoluchowskis predictions of a linearly growing mean square displacement has been verified by Perrin [1, 2, 4], who was, at the same time, able to calculate Avogadros number". The huge difference in the typical time scales of motion of a solvent molecule and a colloidal particle leads to a separation of the dynamics. This fact allows one to regard the influence of the suspending medium as a very short-time correlated random process. Moreover, one typically defines the *Brownian time*, τ_B, describing the time that is needed for a particle to cover a distance of its own size. Beyond this time, the motion can be considered overdamped, which means that the motion is no longer systematically ballistic in its character.

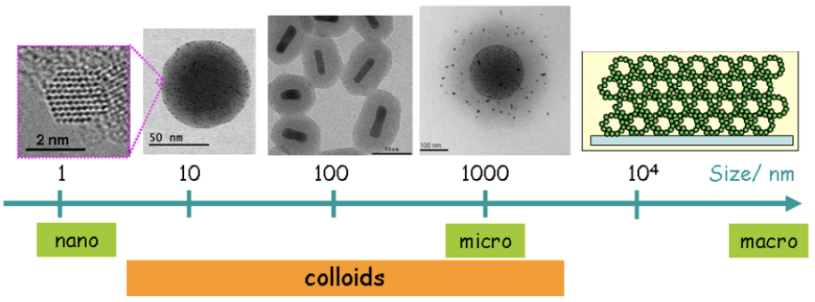

FIGURE 1.1: The skematic of colloids' length scales. The particles from left to right: Au nanoparticles, metal composite particles, Au nanorod+silica shell, core-shell microgels, porous structure of catalyst . Figure taken from Ref. [5]

As a colloidal particle translates or rotates, it induces a fluid flow in the solvent which affects other Brownian particles in their motion. These interactions are mediated via the solvent and standardly called as *hydrodynamic interactions*, which lead to rich phenomena of particles motion. This dynamics strongly depends on particle shape and relevant examples of our interest are rod-like colloids or structure with chiral symmetry such as helices. Rods tumble and kayak in shear flow [3, 6–9]. Chiral particles migrate in vorticity direction of shear flow [10–12]. Helical microorganisms can translate or rotate in solvent by a non-reciprocal deformation [13–17].

1.1 Application of colloids system

There are plenty of colloidal products in our daily lives as shown in Fig. 1.1, such as dairy products [18], cosmetics and paint, recent advances in chemical synthesis allow production of functional colloids as well as self-propelled or complexly shaped particles [19]. On one hand, there are practical considerations for the use of colloids in a variety of fields, such as microfluidics, material design, pharmaceutics or drug delivery [20]. On the other hand, fascinating systems can be designed to address fundamental relevant questions. Mutually attached spheres, for example, are sometimes referred to as colloidal molecules as they resemble atomic molecules in their shapes and it is possible to control the bond-angles and overall size and shape [21]. Thus, colloids may be regarded as models for atomic or molecular systems, which simplify the investigation of analogous systems due to slower time scales and larger sizes of the particles [22]. Moreover, on this fundamental level, colloids enable the understanding of the mechanisms of phase transitions and arrested states [23].

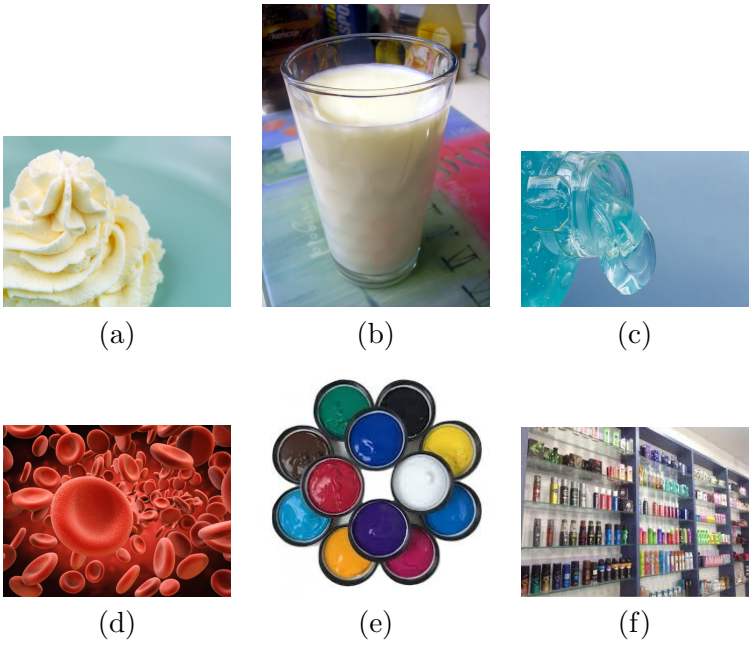

(a) (b) (c)

(d) (e) (f)

FIGURE 1.2: Types of colloids in our daily life. (a) Icecream (b) milk (c) hydrogel (d) blood (e) paints (f) cosmetics. Copy right @ prochemicalanddye.net

1.2 Anisotropic colloids' shape and non-equilibrium dynamics

In general, colloidal particles are anisotropic in shape, which was considered in the light of mineral sheets, rod-like viruses and flexible polymer chains by Perrin and Onsager in the 1930s and 1940s [24, 25]. Suspensions of anisotropic particles have been studied by many researchers, e.g. spherocylinders as models for micro-organisms [26, 27]. Recent advances in the chemical synthesis and fabrication of colloidal particles have resulted in a wide variety of shape and size of shape-anisotropic particles, such as rods [28, 29], plates [30], dumbbells [31], hollow objects, microcapsules, patchy particles, cubes [32], octahedra [33], tetrahedra [34], nanostars [35], and colloidal caps, [34] as illustrated in Fig. 1.2.

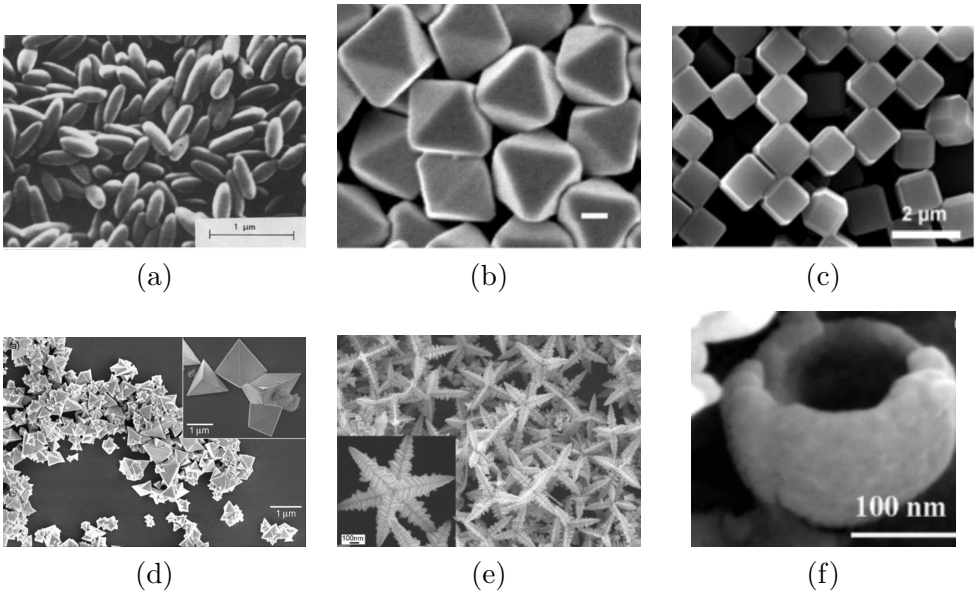

FIGURE 1.3: Scanning electron micrographs of particles. (a) rod (b) octahedra (c) cube (d) tetrahedra (e) stars (f) cap. Figures taken from [28, 32, 34, 34, 35]

In equilibrium, anisotropy gives rise to novel phases, such as the PC or rotator phase, nematic or liquid crystalline states [36, 37]. At different temperature, for example rod-like liquid crystal molecules exhibits different levels of orientational and positional order as shown in Fig. 1.4. Furthermore, the anisotropy of the suspended particles may be of great importance for dynamical quantities as well as structural formation under external fields [38, 39].

Fascinating phenomena are observed in colloids under the influence of external fields [41]. In processing suspensions, various kinds of external fields are applied to colloids, which may be electrical [42], magnetic [43], also flow fields [44] or gravity [45], to name a few [46]. In fact, even walls or confining boundaries can be seen as a method of external control. The application of external fields can change the equilibrium of the system [47], lead to non-equilibrium steady states or drive the system into full transient non-equilibrium [48]. Under gravity, for example, the coexistence of different phases may be observed due to density gradients [49].

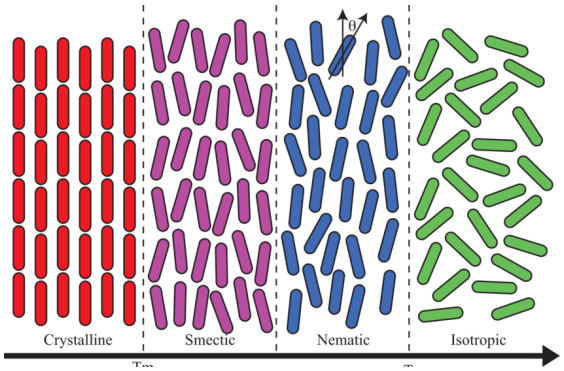

FIGURE 1.4: Illustration of rod-like liquid crystal molecules exhibiting different levels of orientational and positional order in the crystal, smectic, nematic, and isotropic phases as a function of increasing temperature with melting and clearing points noted. Figure recreated from [40]]

A very important class of external fields are flow fields, which can be quite complex. This spatial or temporal complexity is strongly dependent on the boundary conditions and the driving forces causing media to flow. One of the most elementary flows is the simple shear flow, where the velocity is unidirectional and depends linearly on the distance from the walls. *Couette flow* is the laminar solution for fluid confined between two plates one of which is moving and the other is fixed at a certain distance with no-slip boundary conditions [50]. Shear flows are very common in processing and transport of material as they are inevitably present due to typical boundary conditions on the flowing medium. In order to analyse the response of a medium to shear, one typically chooses simple shear with an oscillatory or steady time dependence. In the context of colloidal flow, shear can lead to a multitude of phenomena: shear fields may be used to induce crystallisation in colloidal hard sphere glasses, [51] or drive gelation in dilute suspensions of charge-stabilised particles [52]. It may be desirable to prevent crystallisation or glass formation in a process, as solidification can hamper the transport of material. The behaviour of particles under shear have rich phenomena. In Fig. 1.5, for example, semi-flexible polymers exhibit tumbling motion, i.e., they undergo a cyclic stretch and collapse dynamics, with a characteristic frequency which depends on the shear rate and their internal relaxation time [44].

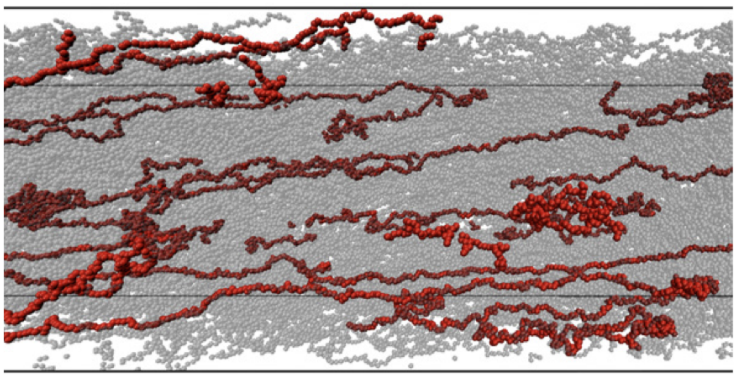

FIGURE 1.5: Snapshot of semiflexible polymers under shear flow. Figure taken from Ref. [44]

1.3 Rheo-optical approach for particle charaterization

The knowledge of the precise size and shape of colloidal particles is frequently important, as they have a strong effect on the rheological, optical, and/or mechanical properties of suspensions. Preparation of samples for electron microscopy is often laborious and expensive and the analysis of the images is not trivial. Light-scattering methods, as used in many commercial particle-sizing instruments, are not designed to assess particle shapes. Special methods requiring multiple detectors are needed for this purpose, as the angular dependence of the scattered light needs to be analyzed [53]. Measurements of changes in the polarization state of the scattered light provide a possible alternative for nonspherical particles with a given orientation. The establishment of new approaches to determine size and shape of colloids is therefore timely and relevant.

Particle dynamics is governed by the particle geometry, which for example determines the manner of rotation in the flow. For a given particle, the angular velocity is not necessarily constant in time. If the particle is elongated it slows down as its orientation approaches the flow direction and it increases whne it is not oriented. It has been shown that polarimetry measurements of birefringence and especially linear conservative dichroism can be used to study the dynamics of dilute colloidal suspensions in simple shear flow [54–56] .

Linear conservative or scattering dichroism is a property related to anisotropic scattering of light. It is defined as the difference in the principal eigenvalues of the imaginary part of the refractive-index tensor. In a dilute system of nonspherical particles, the magnitude of the linear conservative dichroism reflects the degree of alignment induced by the shear flow. Here, however, it is more convenient and simple to consider evolution of the average orientation angle χ, which is given by the projection of the principle axis of the imaginary part of the refractive-index tensor in the flow-velocity gradient plane. It is a purely geometrical property, the determination of which is not affected by the size for samples with uniform optical properties. For that reason it is more suited to characterize suspensions of nonspherical particles. Existing methods have shown that the combination of rheo-optical approach and theoretical results of particle orientation can obtain aspect ratios and polydispersity of particles under assumptions of nearly spherical particles, narrow distribution of size, negligible Brownian motion [57, 58] illustrated in Fig. 1.3.

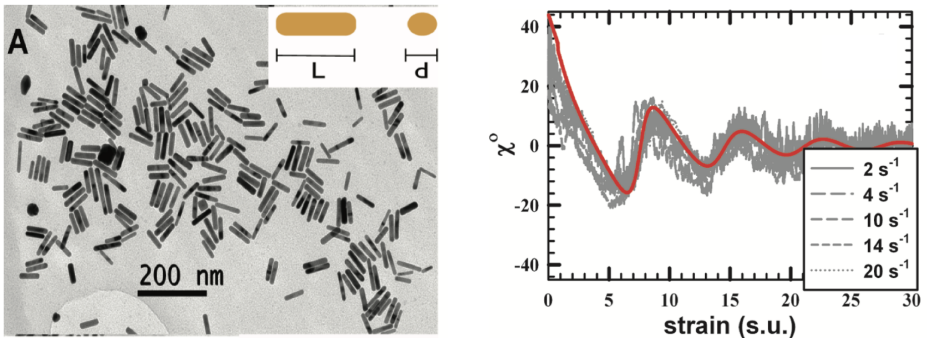

(a) (b)

FIGURE 1.6: (a) Transmission electron micrographs of nonspherical gold nanoparticles. (b) Orientation angle χ as a function of strain for (a). Figures taken from Ref. [58]

1.4 Motion of chiral objects

A chiral object has two distinct forms that are mirror images to each other, but each can not be converted into the other by pure spatial rotations as shown in Fig. 1.7. The study of the dynamics and interactions of chiral obejcts is an interesting and fascinating subject. The pioneering observation by Louis Pasteur in 1848 linked the chirality of the sodium ammonium salt crystals to light polarization [59]. Chirality in macromolecules has led to many important structural properties, especially in liquid crystals [60]. As for example, the double helix of DNA is chiral and always right handed [61]. All but one of natural amino acids, the building blocks of proteins, are chiral and are only in the left-handed forms. Many other molecules important to life are chiral, and it is still a mystery why only one of the two enantiomers is used by living organisms [62].

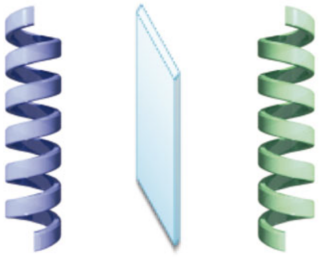

FIGURE 1.7: Illustration of chirality by helices. Figure taken from Ref. [63]

Recently, synthetic helical particles at the nanoscale, with radii smaller than 100nm have become available [64, 65]. Controlled and directed motion of chiral particles has important applications as in the case of targeted delivery of genetic material and drugs, this is since such particles can be tailored to facilitate their efficient uptake by various cells or tissues. Controlled motion and cargo transport of magnetic helical particles has been demonstrated [43]. Application of time-dependent magnetic fields on magnetic screw-like particles induces a torque that rotates the particle and propels it in the fluid. Manipulation of the direction of the rotating magnetic fields makes it possible to load microspheres as cargo into the holder of a helical particle, transport the cargo and then release it at a preferred site [43]. In the interesting work shown in Fig. 1.8, externally

driven microhelices can be used to assists sperm to delivery on immotile live cell [66], see Fig. 1. 8.

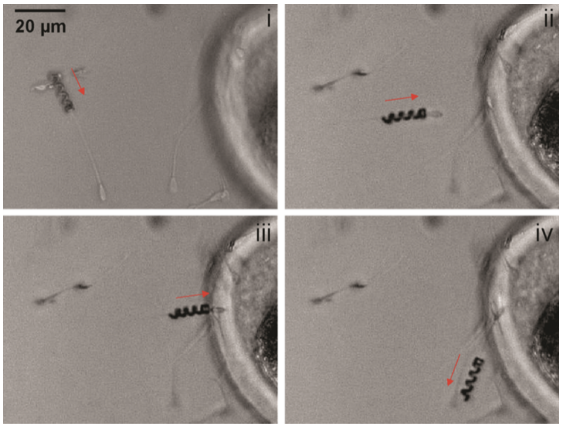

FIGURE 1.8: (i) Sperm cell captured by by magnetic helcal micro particle (ii) transport (iii) approach to the oocyte membrane (iv) and release. Figure taken from Ref. [66]

Chemical syntheses of chiral molecules in laboratories usually produce roughly equal amounts of the two enantiomers, such that separation of enantiomers becomes an important issue inspite of difficult process. Currently, the main methods consist in driving the enantiomer mixtures through specific chiral filling materials, often with not so satisfactory efficiencies [67, 68]. Motion and kinetics of chiral objects are largely determined by their spatial anisotropy since it leads to a coupling between the translational and rotational degrees of freedom. De Gennes already suggested dragging by external forces an enantiomer crystal along the surface of a liquid or solid [69]. As illustrated in Fig. 1.9, the friction on helix under shear could then produce a chiral-specific lateral forces, although it was noted that the crystal needs to be macro-sized to overcome the thermal fluctuations. It was then proposed that a microfluidic flow with spatially varied vorticity could separate enantiomers, due to intricate interplay between the particle transport and thermal fluctuating diffusive motions [70].

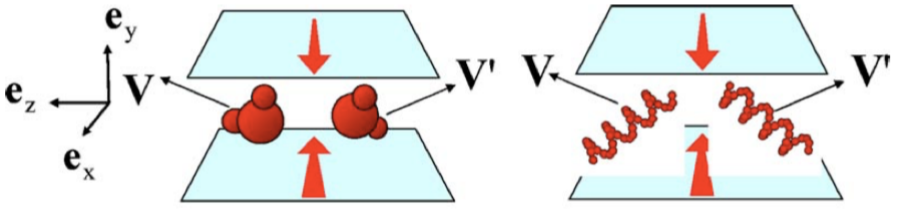

FIGURE 1.9: Motion of chiral particles placed in shear flow. If the particle P moves with the velocity $\mathbf{V}$ in the shear flow, the mirror-imaged particle P will move with the velocity $\mathbf{V}'$, which is the mirror image of V. Figure taken from Ref. [71]

1.5 Microswimmer at low Reynolds number

Active matter is a fascinating new field in soft matter physics. It concerns the macroscopic properties of interacting active particles, which are individually able to convert energy into directed motion. As disccussed in Ref. [72], "Locomotion is a major achievement of biological evolution and is an essential aspect of life. Search for food, orientation toward light, and spreading of the own species are only possible due to locomotion. The spectrum of biological active system in microscopic world is vast, ranging from spermatozoa [73], bacteria [72, 74], to the cytoskeleton in living cells [75–78]. Yet, highly active systems are not just limited to examples from nature and the development of synthetic microswimmers is recently making an enormous progress [79]". Hence, studying the dynamics of active matter is a key element on the way to a better understanding of autonomous biological systems, the development of novel biomedical technologies, and new designs of microfluidic devices. A common characteristics of active matter is the utilization of energy from the environment for, or the internal conversion of chemical energy into, directed propulsion [72, 74, 79–83].

The physics of microswimmers is fairly different from that we experience in our macroscopic world. While for, e.g., swimming humans, inertia is dominating over the viscous forces, for microswimmers it is the other way around. The ratio between the inertial and viscous forces is known as Reynolds number. The value of the Reynolds number spans over several orders of magnitude from 10^6 of swimming humans to 10^{-5} of bacteria. At high Reynolds numbers, the momentum transferred from the swimming body to the surrounding fluid convects and slowly dissipates from larger to smaller length scales. At low Reynolds numbers there is almost no inertial delay in time between the applied forces and the fluid response. Therefore, at zero Reynolds number, every reciprocal motion, i.e., every periodic motion, which after time reversal is identical to its original dynamics, will not lead to self-propulsion. This property is known as the scallop theorem [14, 82].

Artifical microswimmers can be constructed by using similar design principles as those found in biological systems. As explained in Ref. [72], "A by now classical example is a swimmer which mimics the propulsion mechanism of a sperm cell [84]. The flagellum is constructed from a chain of magnetic colloid particles and is attached to a red blood cell, which mimics the sperm head. This artificial swimmer is set into motion by an alterating magnetic field, which generates a sidewise oscillatory deflection of the flagellum. However, the swimming motion is not the same as for a real sperm cell; the wiggling motion is more a wagging than a travelling sine wave, and generates a swimming motion toward the tail end, opposite to the swimming direction of sperm. A recent example of a biohybrid swimmer which mimics the motion of sperm has been presented by Williams *et al.* [85]. In this case, the microswimmer consists of a polydimethylsiloxane filament with a short, rigid head and a long, slender tail on which cardiomyocytes (heart-muscle cells) are selectively cultured. The cardiomyocytes contract periodically and deform the filament to propel the swimmer. This is a true microswimmer because it requires no external force fields. The swimmer is about 50 μm long and reaches a swimming velocity up to 10 μm/s". A more recent experimental work [86] has shown for the purposefully shaped microhydrogels that the kinematics of a cyclic body shape

variation can be tuned to differentiate between the forward and the backward motion as shown in Fig. 1.5. Thus, the first deformation stroke (upon heating) is not reciprocated by the second deformation stroke (during cooling), even though the cycle ends up at its starting configuration. Based on this, a light-fueled and light-controlled microswimmer has been designed, which can rotate and move forward by its body deformation.

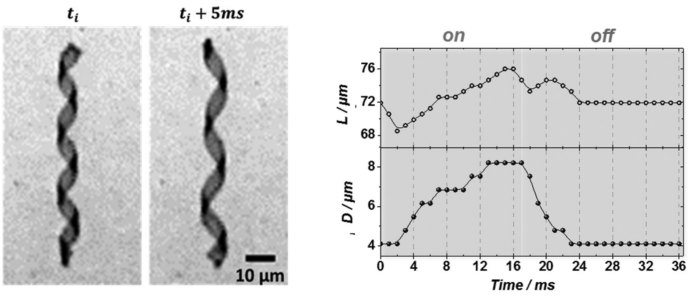

(a) (b)

FIGURE 1.10: Actuation characteristics of a microgel ribbon helix under stroboscopic irradiation. a) Microscopy images from time-lapse videos of the helix during irradiation. b) Instantaneous helix length and diameter during one irradiation cycle. The left part corresponds to when the light is on, while the right part corresponds to when the light is off. Figures taken from [86]

1.6 Objectives and outline of the thesis

Chapter 2: The related theoretical framework will be introduced by including the dynamics of shape-anisotropic colloids, hydrodynamics in Stokes regime, and some theoretical methods applied in microswimmers. Then a hybrid simulation method will be introduced, which combines multi-particle dynamics with molecular dynamics.

Chapter 3: Since the hydrodynamic aspect ratios and polydispersity of particles are important for the application of nano-particles, a charaterization technology is developed. The Smoluchowski equation can be generalized on arbitrary aspect ratios, polydispersity, and include thermal fluctuation, which goes beyond the limits of the existing methods [57, 58]. The numerical results of Smoluchowski equation contain the shear rate, the equivalent hydrodynamic aspect ratio, and the associated polydispersity. Then they can be obtained from a fit to the experimental data, as will be demonstrated for a model system containing quantum dots.

Chapter 4: The non-equilibrium dynamics of helix have been studied [11, 45, 71]. For example, the study has shown that twisted ribbons can be separated by shear flow as illustrated in Fig. 1.6. Previous studies are still restricted to rigid particles or flexible tetrahedron. Therefore, open questions still include how the chiral geometry and flexibility of helix affect the efficiency and migration speed. We address these issues by Molecular dynamics coupled Multi-particles dynamics simulation [87, 88], which intrinsically involve thermal fluctuations hydrodynamic interactions and varying flexibility.

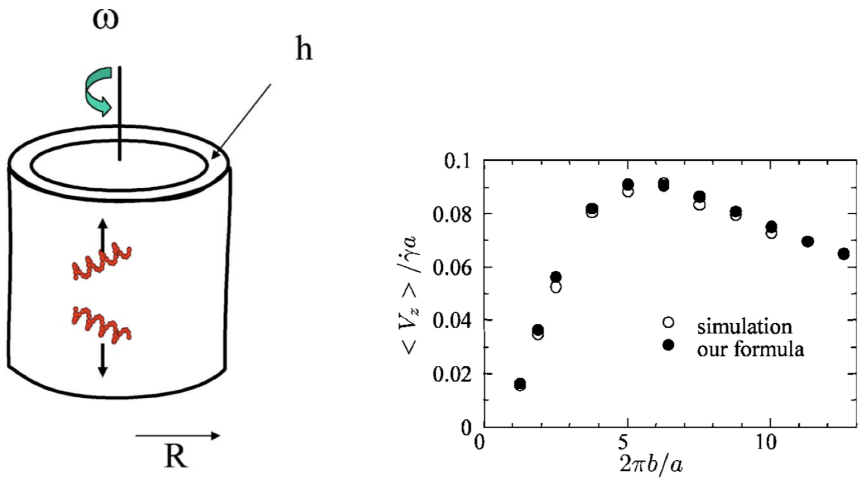

(a) (b)

FIGURE 1.11: (a) Sketch of the rheological separator. (b) Mean migration velocity of twisted ribbon of length in the limit of large Peclet number is plotted against the pitch. Figures taken from Ref. [71]

Chapter 5: Aritifical microswimmers have a huge potential applications in drug delivery and micro-robots. Recent experimental work developed a novel gel which can deform by responsing to temperature as shown in Fig. 1.5. As a results the actively driven helix has a net rotation. Later theoretical work [89] demonstrated that the net rotation is due to non-reciprocal deformation of helix. However, the effect of fluid viscosity and walls on the swimming and migration of helix was not considered. Therefore, we investigate these issues, including the effect of helix configuration, fluid viscosity, deformation periods on the propulsion of helix herein by the same former simulation method.

Chapter 2

Theoretical background and simulation Methods

2.1 Theoretical Background

2.1.1 Dynamics of dilute non-spherical colloids

Shear flow is typical case where the dynamical behavior can be investigated in a stationary nonequilibrium state. Shear flow affects microstructural order of colloidal systems in two respects : center-to-center correlations are affected by flow and flow can induce changes in orientational order. For spherical colloids, flow-induced changes of macroscopic properties find their origin entirely in shear-induced changes of center-to-center correlations. For non-spherical colloidal particles, flow also tends to align single colloidal particles due to the torque that the flowing solvent exerts on their cores. For very elongated colloids, single particle alignment is dominant over shear-induced changes of center-to-center correlations. For such systems, equations for one-particle orientational distribution functions, with the neglect of flow-induced distortions of center-to-center correlations, are sufficient to predict their macroscopic behaviour under flow. For spherical colloidal particles, however, one-particle distribution functions are not affected by flow, so that theory for spheres should be based on equations for correlation functions.

2.1.1.1 The velocity gradient tensor

A linear flow profile is characterized by means of the velocity gradient tensor $\mathbf{G}$, where the flow velocity $\mathbf{U}$ at position $\mathbf{r}$ is written as $\mathbf{U} = \mathbf{G} \cdot \mathbf{r}$. In case of simple shear flow, the gradient velocity tensor is usually denoted as Γ, and is equal to

$$\mathbf{\Gamma} = \dot{\gamma} \begin{pmatrix} 0 & 1 & 0 \\ 0 & 0 & 0 \\ 0 & 0 & 0 \end{pmatrix}, \quad \text{simple shear flow.} \tag{2.1}$$

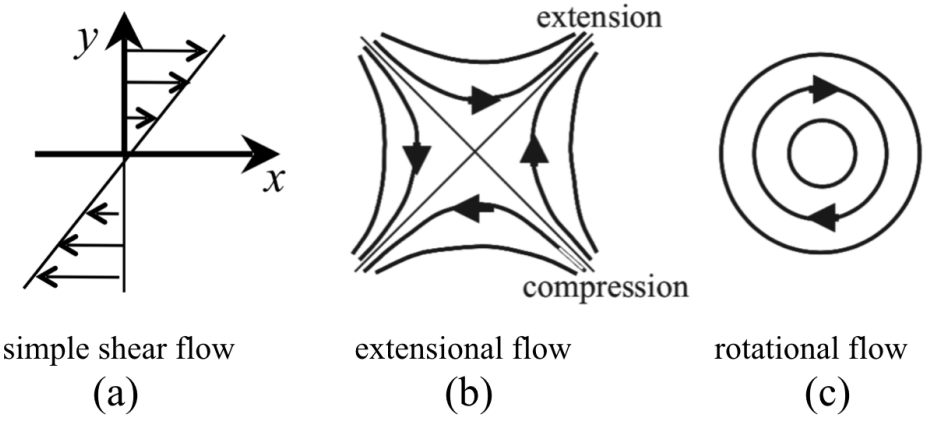

FIGURE 2.1: (a) Simple shear flow. (b) Elongational flow, sometimes also referred to as extensional flow (where the elongational and compression axes are indicated), and (c) Rotational flow. Arrows indicate the flow direction.

The corresponding flow profile is a flow in the x-direction, with its gradient in the y-direction, as sketched in Fig. 2.1a. The z-direction is commonly referred to as the vorticity direction. The strength of the flow is characterized by the shear rate , which equals the spatial gradient $\partial U_x/\partial y$ of the flow velocity U_x in the x-direction. For elongational or extensional flow, the velocity gradient tensor is denoted as $\mathbf{E}$, and reads,

$$\mathrm{E} = \frac{1}{2}\dot{\gamma}\begin{pmatrix} 0 & 1 & 0 \\ 1 & 0 & 0 \\ 0 & 0 & 0 \end{pmatrix}, \quad \text{elongational flow.} \tag{2.2}$$

the corresponding flow is sketched in Fig. 2.1b. In such an elongational flow, deformable objects tend to elongate along the so-called extensional axis, and compressed along the compressional axis. With this coordinate these two directions are in the diagonal of $x-y$ axis as indicated in fig. 2.1b. Whenever it is not specified whether simple shear flow or elongational flow is considered, the velocity gradient tensor can be generally denoted as $\mathbf{G}$.

It is instructive to use velocity calculus method, which allow to decouple any arbitrary matrix in its symmetry $\mathbf{G}^{\mathrm{S}}$ and asymmetry $\mathbf{G}^{\mathrm{A}}$ parts $\mathbf{G}$, $\mathbf{G} = \mathbf{G}^{\mathrm{S}} + \mathbf{G}^{\mathrm{A}}$ with $\mathbf{G}^{\mathrm{S}} = \frac{1}{2}(\mathbf{G} + \mathbf{G}^{\mathrm{T}})$ and $\mathbf{G}^{\mathrm{A}} = \frac{1}{2}(\mathbf{G} - \mathbf{G}^{\mathrm{T}})$, where the superscript T stands for the transpose of the corresponding tensor. For elongational flow, the velocity gradient tensor is already symmetric, such that $\mathbf{G}^{\mathrm{S}} = \mathbf{E}$ and $\mathbf{G}^{\mathrm{A}} = \mathbf{0}$. For simple shear flow we have $\mathbf{G}^{\mathrm{S}} = \frac{1}{2}\mathbf{E}$ and $\mathbf{G}^{\mathrm{A}} = \frac{1}{2}\mathbf{\Omega}$ with $\mathbf{\Omega}$ the rotation matrix:

$$\mathbf{\Omega} = \frac{1}{2}\dot{\gamma}\begin{pmatrix} 0 & 1 & 0 \\ -1 & 0 & 0 \\ 0 & 0 & 0 \end{pmatrix}, \quad \text{simple shear flow} \tag{2.3}$$

The flow velocities corresponding to rotational flow in Eq. 2.3 are sketched in fig. 2.1c, Note that,

$$\mathbf{\Gamma} = \mathbf{E} + \mathbf{\Omega} \tag{2.4}$$

so that simple shear flow can be decomposed into a linear combination of elongational and rotational flow, which is relevant to explain the rotate polymer dynamics.

2.1.1.2 Translational diffusion

For non-spherical colloids, the friction coefficient is not isotropic since it depends on the orientation of the rod/plate relative to it's velocity. The orientation of a rod is characterized by a unit vector $\hat{\mathbf{u}}$ along it's long axis (see Fig. 2.2a). When the rod moves through the fluid along $\hat{\mathbf{u}}$, the friction coefficient $\zeta_{||}$ is different from the friction coefficient $\zeta_{\perp}$ when the rods moves in a direction perpendicular to $\hat{\mathbf{u}}$. A velocity $\mathbf{v}$ with arbitrary direction can be decomposed in it's components $\mathbf{v}_{||}$ parallel to it's long axis and it's perpendicular component $\mathbf{v}_{\perp}$. The parallel component is equal to $\mathbf{v}_{||} = \hat{\mathbf{u}}\hat{\mathbf{u}} \cdot \mathbf{v}$, while the perpendicular component is equal to $\mathbf{v}_{\perp} = \mathbf{v} - \mathbf{v}_{||} = [\hat{\mathbf{I}} - \hat{\mathbf{u}}\hat{\mathbf{u}}] \cdot \mathbf{v}$ (where $\hat{\mathbf{I}}$ is the identity tensor). The friction force $\mathbf{F}^h$ is thus equal to [90],

$$\mathbf{F}^h = -\zeta_{||}\mathbf{v}_{||} - \zeta_{\perp}\mathbf{v}_{\perp} = -\left\{\zeta_{||}\hat{\mathbf{u}}\hat{\mathbf{u}} + \zeta_{\perp}\left[\hat{\mathbf{I}} - \hat{\mathbf{u}}\hat{\mathbf{u}}\right]\right\} \cdot \mathbf{v}, \tag{2.5}$$

A colloid moving in a fluid with constant velocity has no net applied force such that $\mathbf{F}^h + \mathbf{F}^{Br} = 0$ (where the superscript "Br" stands for "Brownian"),

$$\mathbf{F}^{Br} = -k_B T \nabla \ln P(\mathbf{r}, t). \tag{2.6}$$

By combination of Eq. 2.5 and Eq. 2.6, we can get

$$\mathbf{v} = -\mathbf{D}(\hat{\mathbf{u}}) \cdot \nabla \ln P(\mathbf{r}, t), \tag{2.7}$$

with the diffusion tensor

$$\mathbf{D} = D_{||}\hat{\mathbf{u}}\hat{\mathbf{u}} + D_{\perp}\left[\hat{\mathbf{I}} - \hat{\mathbf{u}}\hat{\mathbf{u}}\right] \tag{2.8}$$

where $P(\mathbf{r}, t)$ is the probability density function (pdf) of colloid the center-of-mass position $\mathbf{r} = (x, y, z)$ of a colloidal particle, at time t and,

$$D_{||} = \frac{k_B T}{\zeta_{||}} \quad , \quad D_{\perp} = \frac{k_B T}{\zeta_{\perp}}. \tag{2.9}$$

are the parallel and perpendicular diffusion coefficients. According the continuty equation [91, 92], we thus finally arrive at the diffusion equation for translational motion of a non-sperical particle,

$$\frac{\partial}{\partial t}P(\mathbf{r},t) = \nabla \cdot \mathbf{D}(\hat{\mathbf{u}}) \cdot \nabla P(\mathbf{r},t) \tag{2.10}$$

The most simple average that characterizes Brownian motion is the so-called *mean − squared displacement* $W(t) = \langle r^2 \rangle$ (with $r = |\mathbf{r}|$ the distance of the center-of mass from the origin). $W(t)$ can be calculated by first multiplying Eq. 2.10 on both sides with r^2. Since $W(t=0) = 0$, this implies that,

$$W(t) = 6Dt. \tag{2.11}$$

In order to analyze the motion of a rod we therefore need a similar diffusion equation for the orientation of the rod.

2.1.1.3 Rotational diffusion

For non-spherical macromolecules it is not only the center-of-mass that exhibits random Brownian motion due to collisions with fluid molecules, but also it's orientation changes as a result of these interactions.

We consider a rod-like Brownian particle, the orientation of which is specified by a unit-vector $\hat{\mathbf{u}}$. For a rod-like particle this vector lies along the long axis of the rod, while for a platelet this vector can be chosen to be perpendicular to the face of the platelet (see Fig. 2.2)a The tip of the unit-vector $\hat{\mathbf{u}}$ lies on a unit-spherical surface. Changes in orientation leads to motion of the tip of $\hat{\mathbf{u}}$. on a unit-spherical surface (as depicted in Fig. 2.2b). We define the probability density function (pdf) $P(\hat{\mathbf{u}},t)\mathrm{d}\hat{u}$ is the probability that $\hat{\mathbf{u}}$ takes a value within the small surface area element $\mathrm{d}\hat{u}$ on the unit-spherical surface (see Fig. 2.2c). The rotational diffusion equation:

$$\frac{\partial}{\partial t}P(\hat{\mathbf{u}},t) = D_r\hat{\mathcal{R}}^2 P(\hat{\mathbf{u}},t) \tag{2.12}$$

where D_r is rotational diffusion coefficient. The rotational operator is defined as,

$$\hat{\mathcal{R}}(\cdots) = \hat{\mathbf{u}} \times \nabla_{\hat{u}}(\cdots) \tag{2.13}$$

The time dependence of the average of the orientation vector $\hat{\mathbf{u}}$ can be obtained from Eq.2.12 by multiplying both sides with $\hat{\mathbf{u}}$ and integrating over the unit-spherical surface,

$$\frac{\mathrm{d}\left\langle \hat{\mathbf{u}} \right\rangle (t)}{\mathrm{d}t} = D_r \oint d\hat{\mathbf{u}}\hat{\mathbf{u}}\hat{\mathcal{R}}^2 P(\hat{\mathbf{u}},t) = D_r \oint d\hat{\mathbf{u}} P(\hat{\mathbf{u}},t)\hat{\mathcal{R}}^2\hat{\mathbf{u}} = -2D_r \left\langle \hat{\mathbf{u}} \right\rangle (t) \tag{2.14}$$

A partial integration is performed in the second equality. The orientational equivalent of mean-squared displacement is $W_{\hat{u}}(t) = \left\langle |\hat{\mathbf{u}} - \hat{\mathbf{u}}_0|^2 \right\rangle$, where $\hat{\mathbf{u}}_0$ is the orientation of the particle at the initial time. From the above results is found that,

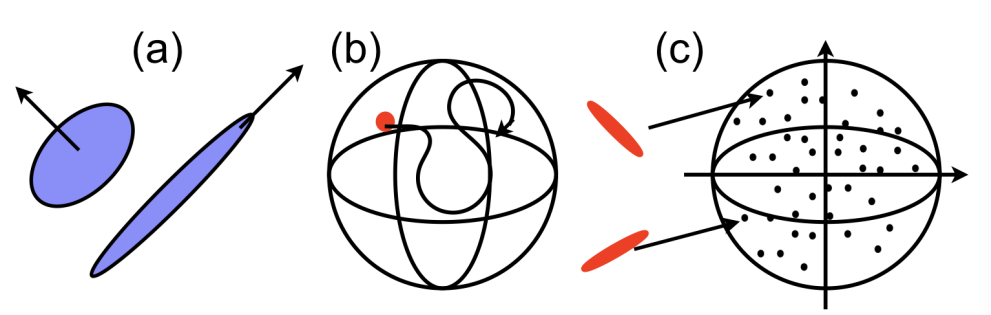

hbt!

FIGURE 2.2: (a) A platelet (left) and rod-like (right0 colloidal particle, where the unit vector "$\hat{\mathbf{u}}$" defines their orientations. (b) The tip of the unit vector $\hat{\mathbf{u}}$, in red, lies on an unit-spherical surface (the surface of as sphere with radius unity). The red "point-particle" exerts Brownian motion on the unit-spherical surface. (c) The orientations of two rods are mimicked as different points on the unit-spherical surface

$$W_{\hat{u}}(t) = \left\langle \hat{\mathbf{u}}^2 \right\rangle + \hat{\mathbf{u}}_0^2 - 2\left\langle \hat{\mathbf{u}} \right\rangle \hat{\mathbf{u}}_0 = 2\left[1 - \exp\left\{-2D_r t\right\}\right] \tag{2.15}$$

For small times, with $D_r t \ll 1$, $W_{\hat{u}}(t)$is the displacement of the tip of $\hat{\mathbf{u}}$ on the two-dimensional plane perpendicular to $\hat{\mathbf{u}}_0$. Expanding the exponent function (using that $\exp x = 1 + x + \cdots$) leads to $W_{\hat{u}(t)} = 4D_r t$, which indeed complies to Eq. 2.11 for translational diffusion in two dimensions.

2.1.1.4 Diffusion in the presence of shear flow

In the present section we discuss probability density functions (pdfs) and orientational order parameter matrices for a single Brownian rod subjected to flow. On applying a stationary flow, the orientational pdf of a single rod attains a stationary form. This time independent pdf is determined by the interplay of the aligning effect of the flow and isotropy-restoring rotational diffusion. The stationary form of the Smoluchowski equation [91] for a single rod reads,

$$0 = \hat{\mathcal{R}}^2 P(\hat{\mathbf{u}}) - Pe_r \hat{\mathcal{R}} \cdot \left[P(\hat{\mathbf{u}})\hat{\mathbf{u}} \times (\mathbf{G} \cdot \hat{\mathbf{u}})\right], \tag{2.16}$$

where the dimensionless parameter Pe_r is commonly referred to as the rotational Peclet number, which is defined as,

$$Pe_r = \frac{\hat{\gamma}}{D_r} \tag{2.17}$$

This Peclet number is a measure for the effect of the shear flow relative to isotropy-restoring rotational diffusion. For small Peclet numbers, rotational diffusion is relatively fast, so that the pdf is only slightly anisotropic.

The stationary equation of motion can be solved in closed analytical form when the velocity gradient tensor $\mathbf{G}$ is symmetric (as for elongational flow). When the velocity gradient tensor is not symmetric (as for simple shear flow), the solution cannot be obtained in a simple closed analytical form, but must be obtained by numerical methods. However, expansion of the orientational pdf for small Peclet numbers is feasible.

In case of shear flow and for small rotational Peclet numbers the deviation of the pdf from the isotropic solution is small, so that the solution of the stationary equation of motion 2.16 can be expanded as,

$$P(\hat{\mathbf{u}}) = \frac{1}{4\pi} + Pe_r P_1(\hat{\mathbf{u}}) + Pe_r^2 P_2(\hat{\mathbf{u}}) + \cdots. \tag{2.18}$$

Substitution of this expansion into Eq. 2.16 and equating coefficients of equal powers of Pe_r, one readily finds the following recursive set of differential equations for the as yet unknown functions P_j,

$$\hat{\mathcal{R}}^2 P_j(\hat{\mathbf{u}}) = \hat{\mathcal{R}} \cdot [P_{j-1}(\mathbf{u})\mathbf{u} \times (\Gamma \cdot \mathbf{u})] \quad , \quad j \geq 1, \tag{2.19}$$

where $P_0(\hat{\mathbf{u}}) = 1/4\pi$ is the isotropic pdf without shear flow. Normalization requires that,

$$\oint d\hat{\mathbf{u}} P_j(\hat{\mathbf{u}}) = 0 \ , \ j \geq 1. \tag{2.20}$$

Let us consider the first two terms in the expansion 2.18. For $j = 1$, using that $P_0(\hat{\mathbf{u}}) = 1/4\pi$, Eq. 2.19 reads,

$$\hat{\mathcal{R}}^2 P_1(\hat{\mathbf{u}}) = \frac{1}{4\pi}\hat{\mathcal{R}} \cdot [\hat{\mathbf{u}} \times (\Gamma \cdot \hat{\mathbf{u}})] = -\frac{3}{4\pi} (\hat{\mathbf{u}} \cdot \mathbf{E} \cdot \hat{\mathbf{u}}) , \tag{2.21}$$

where $\hat{\mathbf{E}}$ is the symmetric part of the gradient velocity tensor $\hat{\Gamma}$ in Eq. 2.1, that is, $\hat{\mathbf{E}} = \frac{1}{2}(\hat{\Gamma} + \hat{\Gamma}^T)$. The above equation follows from the relations given in [91, 92]. Using these relations once more immediately leads to the expression in a spherical coordinates,

$$P_1(\hat{\mathbf{u}}) = \frac{1}{8\pi} (\hat{\mathbf{u}} \cdot \mathbf{E} \cdot \hat{\mathbf{u}}) = \frac{1}{8\pi} \sin^2(\theta) sin(\phi) cos(\phi), \tag{2.22}$$

Substitution of this solution for P_1 into Eq. 2.19 for $j = 2$ yields,

$$\hat{\mathcal{R}}^2 P_2(\hat{\mathbf{u}}) = \frac{1}{8\pi}\hat{\mathcal{R}} \cdot \left[(\hat{\mathbf{u}} \cdot \mathbf{E} \cdot \hat{\mathbf{u}}) \left(\hat{\mathbf{u}} \times \hat{\Gamma} \cdot \hat{\mathbf{u}} \right) \right] = \frac{1}{8\pi} \left[\hat{u}^2 - 5(\hat{\mathbf{u}} \cdot \mathbf{E} \cdot \hat{\mathbf{u}})^2 \right] . \tag{2.23}$$

The solution to Eq. 2.23 is given by,

$$
\begin{aligned}
P_2(\hat{\mathbf{u}}) &= \frac{1}{32\pi}\left[(\hat{\mathbf{u}}\cdot\mathbf{E}\cdot\hat{\mathbf{u}} + \frac{1}{3}(\hat{u}_1^2 - \hat{u}_2^2) - \frac{1}{15})\right] \\
&= \frac{1}{32\pi}\left[\sin^4(\theta)\sin^2(\phi)\sin^2(\phi) + \frac{1}{3}\sin^2(\theta)(\cos^2(\phi) - \sin^2(\phi)) - \frac{1}{15}\right],
\end{aligned}
\tag{2.24}
$$

The constant 1/15 between the square brackets is the result of considering the normalization constraint 2.20.

Summarizing the previous results, we thus obtain the following small Peclet number expansion (valid up to $\mathcal{O}(Pe_r^3)$),

$$
P(\hat{\mathbf{u}}) = \frac{1}{4\pi} + Pe_r\frac{1}{8\pi}(\hat{\mathbf{u}}\cdot\mathbf{E}\cdot\hat{\mathbf{u}}) + Pe_r^2\frac{1}{32\pi}\left[(\hat{\mathbf{u}}\cdot\mathbf{E}\cdot\hat{\mathbf{u}} + \frac{1}{3}(\hat{u}_1^2 - \hat{u}_2^2) - \frac{1}{15})\right] \tag{2.25}
$$

For small Peclet numbers, rods spend most of their time in a direction where $\chi = 45°$ (angle between the director and the flow direction) and eventually perform some rotations. This is the result of the interplay between the Brownian torque on the rod and the torque that the fluid exerts on the rod. A preferred alignment along the flow direction implies a strongly peaked orientational pdf. Brownian torque tends to diminish the strongly peaked pdf in the flow direction, while the fluid torque tends to make it more peaked [90, 91].

2.1.2 Hydrodynamics

Most every day soft matter systems, such as gel-like structures, are typically multi-component systems, and the forming objects, polymers, colloids, etc. are dissolved in a fluid solvent. This fluid significantly influences or even dominates the dynamical behavior of the embedded objects. Fluid motion induced by the displacement of the embedded particle leads to a dynamical response of other particles due to the long-range character of the fluid-mediate interactions. Those are the well-know hydrodynamic interactions.

A theoretical description of hydrodynamic interactions is challenging because of the large length-scale difference between a fluid particle, e.g., a water molecule, and the embedded nano- to micro-meter size particle. Hence, the fluid is often described in terms of linearized Navier-Stokes equations, which can be solved analytically.

2.1.2.1 Navier-stokes equations

The Navier-Stokes equations on large length and time scales of an incompressible fluid determind the mass and momentum conservation of a fluid element and read as [91, 93]:

$$\rho \nabla \mathbf{u} = 0, \tag{2.26}$$

$$\rho \left(\frac{\partial \mathbf{u}}{\partial t} + (\mathbf{u} \cdot \nabla)\mathbf{u} \right) = -\nabla p_s + \eta_s \nabla^2 \mathbf{u} + \mathbf{f}(t) \tag{2.27}$$

where p_s and η_s are pressure and solvent viscosity, respectively. The terms ρ and $\mathbf{u} = \mathbf{u}(\mathbf{r}, t)$ are mass density and velocity field of the fluid at position $\mathbf{r}$ and time t, respectively. Eq. 2.26 is the mass conservative or continuity equation. Eq. 2.27 is the conservative of momentum equation. The additionally assumed incompressibility, which is justified in most applications. The nonlinear term $(\mathbf{u} \cdot \nabla)\mathbf{u}$ is the convection acceleration of fluid. The left hand-side of equation 2.27 expresses the inertia for the system. The term $-\nabla p$ is the pressure gradient. The sign indicates that the force on the fluid is towards the lower pressure. The term $\eta_s \nabla^2 \mathbf{u}$ is the viscous friction forces which appear as restricting forces due to velocity gradients within the fluid. Viscous friction and pressure gradient ($-\nabla p_s + \eta_s \nabla^2 \mathbf{u}$) follow by the divergence from the stress tensor, which is defined as

$$\sigma_s = p_s \mathbf{I} + \mathbf{T} \tag{2.28}$$

The tensors $\mathbf{I}$ and $\mathbf{T}$ are the identity tensor and deviatoric stress tensor, respectively. The gradient of the shear stress tensor gives $\eta_s \nabla^2 \mathbf{u}$. The last term in equation 2.27, $\mathbf{f}(t)$, is related with any external volume force, e.g., gravity.

2.1.2.2 Stokes equation

In order to analyze the contributions of the various terms in the Navier-Stokes equations, we rescale

$$\mathbf{u}' = \mathbf{u}/V_0, \mathbf{r}' = \mathbf{r}/L_0, t' = t/T_0 \tag{2.29}$$

where V_0 is a typical velocity, L_0 is a typical length and T_0 is the timescale of the problem at hand. In those new variables and after multiplying by $L_0^2/(\eta_s V_0)$, the Navier-Stokes equations read

$$\frac{\rho L_0^2}{\eta_s T_0} \frac{\partial \mathbf{u}'}{\partial t'} + \mathrm{Re}\ \mathbf{u}' \cdot (\nabla' \mathbf{u}') = -\nabla' p_s' + \Delta' \mathbf{u}' + \ \mathbf{f}'(t) \tag{2.30}$$

where we defined the dimensionless pressure $p' = L_0^2 \eta^{-1} V_0^{-1} p$, the dimensionless force $\mathbf{f} = L_0^2 \eta_s^{-1} V_0^{-1} \mathbf{f}$, and $\nabla' = \partial / \partial \mathbf{r}'$. Furthermore, we introduced a dimensionless number, the Reynolds number Re

$$\mathrm{Re} = \frac{\rho V_0 L_0}{\eta_s}, \tag{2.31}$$

For $\mathrm{Re} \ll 1$ we can neglect the nonlinear advective term in Eq. 2.27, yielding the linearized Navier-Stokes equations

$$\rho \frac{\partial \mathbf{u}}{\partial t} = -\nabla p + \eta \Delta \mathbf{u} + \mathbf{f} \tag{2.32}$$

For small Reynolds numbers and on the diffusive time scale, the Navier-Stokes equation 2.26 and 2.27, therefore simplifies to,

$$0 = \nabla \cdot \mathbf{u} \tag{2.33}$$

$$0 = -\nabla p + \eta \Delta \mathbf{u} + \mathbf{f} \tag{2.34}$$

The Stokes equations are also known as creeping flow equations. They are time-independent and linear. The latter allows for superposition of solutions, which greatly simplifies the theory. To describe hydrodynamic interactions, where nano- to micrometer size objects are dissolved in a fluid, the convection term is typically neglected, i.e., low Reynolds number fluids are considered [91], or the inertia term is neglected and Eq. 2.27 turns into the Stokes equation.

2.1.2.3 The Oseen tensor

An external force acting on a single point $\mathbf{r}'$ of the fluid is mathematically described by a delta distribution,

$$\mathbf{f}^{ext}(\mathbf{r}) = \mathbf{f}_0 \delta(\mathbf{r} - \mathbf{r}') \tag{2.35}$$

The prefactor $\mathbf{f}_0$ is total force $\int \mathrm{d}\mathbf{r}' \mathbf{f}^{ext}(\mathbf{r}')$ acting on the fluid. Since the creeping flow equations are linear, the fluid velocity at some point $\mathbf{r}$ in the fluid, due to the point force in $\mathbf{r}'$, is directly proportional to that point force. Hence,

$$\mathbf{u}(\mathbf{r}) = \mathbf{T}_o(\mathbf{r} - \mathbf{r}') \cdot \mathbf{f}_0 \tag{2.36}$$

The tensor $\mathbf{T}_o$ is commonly referred to as the Oseen tensor,. The Oseen tensor connects the point force at a point $\mathbf{r}'$ to the resulting fluid flow velocity at a point $\mathbf{r}$. Similarly, the pressure at a point $\mathbf{r}$ is linearly related to the point forces,

$$p(\mathbf{r}) = \mathbf{g}(\mathbf{r} - \mathbf{r}') \cdot \mathbf{f}_0 \tag{2.37}$$

The vector $\mathbf{g}$ is referred to here as the pressure vector.

Consider an external force which is continuously distributed over the entire fluid. Due to the linearity of the creeping flow equations, the fluid flow velocity at some point $\mathbf{r}$ is simply the superposition of the fluid flow velocities resulting from the forces acting in each point on the fluid. Hence,

$$\mathbf{u}(\mathbf{r}) = \int \mathrm{d}(\mathbf{r}'\mathbf{T}(\mathbf{r}-\mathbf{r}') \cdot \mathbf{f}^{ext}(\mathbf{r}') \tag{2.38}$$

The same holds for the pressure,

$$p(\mathbf{r}) = \int \mathrm{d}(\mathbf{r}'\mathbf{g}(\mathbf{r}-\mathbf{r}') \cdot \mathbf{f}^{ext}(\mathbf{r}') \tag{2.39}$$

substitute Eqs. 2.38 and 2.39 into the creeping flow equations (2.34, 2.33), leads to,

$$\nabla \cdot \mathbf{T}(\mathbf{r}) = \mathbf{0} \tag{2.40}$$

$$\nabla^2 \mathbf{g}(\mathbf{r}) - \eta_0 \nabla^2 \mathbf{T}(\mathbf{r}) = \mathbf{I}\delta(\mathbf{r}) \tag{2.41}$$

2.1.3 Models for filamentous swimmer

Exact analytic results for the drag coefficients of certain high-symmetry shapes such as spheres and ellipsoids can be obtained in the Stokes limit. For more complex shapes such as chiral particles, the boundary integral formulation of the Stokes equation can be used [94–96], which reduces the full three-dimensional problem of solving for the fluid flow to the two-dimensional problem of determining source distributions on the bounding surfaces. The typical Reynolds number in experiments of driven magnetic helices at the micron scale and at the nanoscale are about 10^{-8} and 10^{-9} [97]. Hence zero Reynolds number approximation is justified. The resistive force theory (RFT) and the slender body theory (SBT) are the usual approaches used to study the propulsive motion of rigid helices and flagellar propulsion.

2.1.3.1 Resistive force theories

In the 1950s, Gary and Hancock [98] developed resistive force theory to provide a description of HI applied to flexible filaments. It represented a breakthrough in the theory of Stokes flows, which is still widely used [99–101].

In formulating resistive force theory, the filament is assumed to be thin, with a circular cross section. In this way, one can first consider an average force per unit length acting on the filament centerlines, rather than a force per unit area acting over the surface. In addition, the cross-sectional symmetry allows us to consider just two independent,

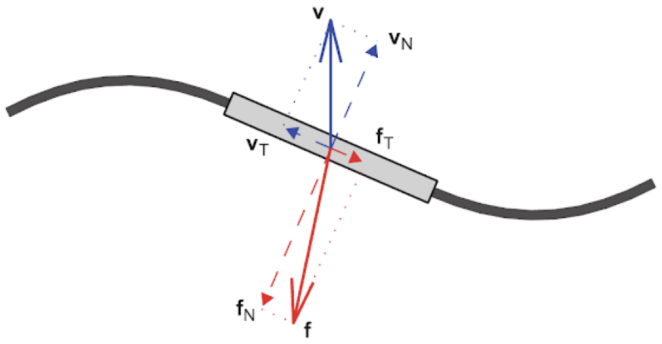

FIGURE 2.3: A two-dimensional representation of the resistive force theory approximation. The local velocity of a slender filament of circular cross section can be separated into components tangential and perpendicular to the filament. Figure cited from [102]

non-trivial coefficients C_{N} and C_{T} relating forces to velocities for the filament in the normal and tangential directions, since the binormal and normal are interchangeable. Decomposing the local filament velocity into its normal, tangential, and binormal directions, i.e., $\mathbf{v} = \mathbf{v}_{\mathrm{N}} + \mathbf{v}_{\mathrm{T}} + \mathbf{v}_{\mathrm{B}}$, with an analogous expression for the local viscous force per unit length acting on the filament, $\mathbf{f} = \mathbf{f}_{\mathrm{N}} + \mathbf{f}_{\mathrm{T}} + \mathbf{f}_{\mathrm{B}}$, then resistive force theory formally states that the local viscous drag forces and filament velocities are related by

$$\mathbf{f}_{\mathrm{T}} = -C_{\mathrm{T}}\mathbf{v}_{\mathrm{T}}, \quad \mathbf{f}_{\mathrm{N}} = -C_{\mathrm{N}}\mathbf{v}_{\mathrm{N}}, \quad \mathbf{f}_{\mathrm{B}} = -C_{\mathrm{N}}\mathbf{v}_{\mathrm{B}}, \tag{2.42}$$

Simple kinematical and symmetry arguments based on linearity are sufficient to demonstrate that a linear, symmetric tensor relates viscous drag to velocity for a sufficient long, straight cylinder, and thus, via a suitable choice of axes, such that the above equation emerges. However, the power of resistive force theory is the demonstration that these relationships hold locally for any slender body with circular cross section, at least to logarithmic accuracy in the body aspect ratio, given appropriate estimates for C_{N} and C_{T}.

For a filament of length L, the net viscous force and net torque are given by

$$\mathbf{F}(t) = \int_0^L \mathbf{f}(s)\mathrm{d}s = -C_{\mathrm{N}}\int_0^L \mathbf{v}_{\mathrm{N}}(s)\mathrm{d}s - C_{\mathrm{N}}\int_0^L \mathbf{v}_{\mathrm{B}}(s)\mathrm{d}s - C_{\mathrm{T}}\int_0^L \mathbf{v}_{\mathrm{T}}(s)\mathrm{d}s \tag{2.43}$$

and

$$\begin{aligned}\mathbf{M}(t) = \int_0^L \mathbf{X}(s)\times\mathbf{f}(s)\mathrm{d}s = &- C_{\mathrm{N}}\int_0^L \mathbf{x}(s)\times\mathbf{v}_{\mathrm{N}}(s) - C_{\mathrm{N}}\int_0^L \mathbf{X}(s)\times\mathbf{v}_{\mathrm{B}}(s)\mathrm{d}s \\ &- C_{\mathrm{T}}\int_0^L \mathbf{X}(s)\times\mathbf{v}_{\mathrm{T}}(s)\mathrm{d}s\end{aligned} \tag{2.44}$$

$\mathbf{X}(s)$ is the centerline of helix. For the propulsion of helical flagellum Hancock [98] explored the resistive coefficients by using singular solutions to Stokes equation, and obtained

$$C_{\mathrm{T}} = \frac{2\pi}{\ln \frac{2\lambda}{b} - \frac{1}{2}}, \quad \gamma = \frac{C_{\mathrm{N}}}{C_{\mathrm{T}}} = 2. \tag{2.45}$$

where b is the cross-sectional radius of the flagellum and λ the wavelength of flagellum. The ratio, $\gamma = 2$, given by Gray and Hancock [98] is only correct for the limiting case of a vanishingly thin helix.

The calculations for the propulsive velocity of rigid helix are carried out by summing the drag and thrust contributions of the rotating helical particles [99, 100]. Also the method is widely used in propulsion of micro-robots such as bacteria or sperm [101, 103].

2.1.3.2 Slender body theories

The need for a more general and accurate modeling framework for the motion of slender filaments in viscous fluids motivated the development of slender body theory. This theory emerged from the studies of Cox [104] and also Batchelor [105] who used a systematic matched asymptotic expansion in the logarithm of the filament aspect ratio. However, these expansions are complex and cumbersome and, due to a logarithmic dependence on the aspect ratio, require large numbers of terms for accuracy. Lighthill [106] greatly simplified the mathematics underlying filament dynamics by constructing solutions from potential diploes as well as Stokeslets on the centerline of a cylindrical filament. This reduced the three-dimensional flow problem to an integral equation for Stokeslets and potential dipoles along the filament centerline and was applied initially for refining resistive force theory as discussed above.

Slender-body theory allows us to derive an approximate relationship between the velocity of the body at each point along its length and the force per unit length experienced by the body at that point.

Consider slender body of length L and typical diameter $2a$ with $L \gg 2a$ surrounded by a fluid of viscosity μ, whose motion is governed by the Stokes equations, see Fig 2.4. Let the axis of the body be described by $\mathbf{X}(s)$, where s is an arc-length coordinate. By virtue of the slenderness of the body, the force exerted on the fluid at the surface of the body may be approximated by a distribution of Stokeslets along the axis with force density $\mathbf{f}(s)$ per unit length. $\mathbf{f}(s)$ is assumed to vary only over lengths much greater than a, see Fig 2.4.

The fluid velocity $\mathbf{u}(\mathbf{x})$ at a general point $\mathbf{x}$ due to such a distribution can be written in terms of an integral of the Oseen tensor (see 2.2.3), which acts as a Green's function for a single Stokeslet,

$$\mathbf{u}(\mathbf{x}) = \int_0^L \frac{\mathbf{f}(s)}{8\pi\mu} \cdot \left(\frac{\mathbf{I}}{|\mathbf{x} - \mathbf{X}|} + \frac{(\mathbf{x} - \mathbf{X})(\mathbf{x} - \mathbf{X})}{|\mathbf{x} - \mathbf{X}|^3} \right) \mathrm{d}s \tag{2.46}$$

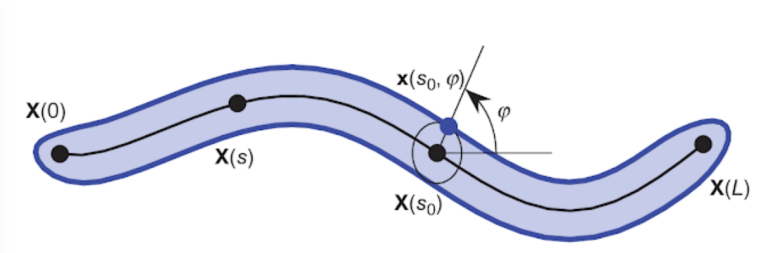

FIGURE 2.4: In slender body theory, Stokeslets and higher order singularities are distributed along the centerline $\mathbf{X}(s)$ with the aim of matching the velocities at surface points $\mathbf{x}(s_0, \varphi)$ to the required local velocity at $\mathbf{X}(s_0)$ for each $s_0 \in [0, L]$ and $\varphi \in [0, 2\pi]$. Figure taken from [102]

Asymptotic analysis can then be used to show that the leading-order contribution to the integral for a point $\mathbf{x}$ on the surface of the body adjacent to position s_0 comes from the force distribution at $|s - s_0| = O(a)$. Since $a \ll L$, we approximate $\mathbf{f}(s) \approx \mathbf{f}(s_0)$, and then obtain

$$\frac{\partial \mathbf{X}}{\partial t} \sim \frac{\ln(L/a)}{4\pi\mu}\mathbf{f}(s) \cdot \mathbf{I} + \left(\frac{\partial \mathbf{X}}{\partial s}\frac{\partial \mathbf{X}}{\partial s}\right) \tag{2.47}$$

The expression can be inverted to give the force density in terms of the motion of the body:

$$\mathbf{f}(s) \simeq \frac{4\pi\mu}{\ln(L/a)}\frac{\partial \mathbf{X}}{\partial t} \cdot \left(\mathbf{I} - \frac{1}{2}\frac{\partial \mathbf{X}}{\partial s}\frac{\partial \mathbf{X}}{\partial s}\right) \tag{2.48}$$

The drag force F on a rigid cylinder (length L , radius a) moving at a velocity u,

$$F = \int_L \mathbf{f}(s)\mathrm{d}s \tag{2.49}$$

either parallel to its axis $F_{\|}$ or perpendicular to it $F_{\perp}$ can be obtained. The parallel force reads,

$$F_{\|} \sim \frac{2\pi\mu L u}{\ln(L/a)} \tag{2.50}$$

while the perpendicular case gives

$$F_{\perp} \sim \frac{4\pi\mu L u}{\ln(L/a)} \tag{2.51}$$

Note that the dominant length scale in the above expressions is the longer length L; the shorter length a has only a weak effect through the logarithm of the aspect ratio. In slender-body theory results, there are $O(1)$ corrections to the logarithm, so even for relatively large values of L/a the error terms will not be that small. Note that the

Stokes' paradox which states that the limit of infinite aspect ratio $L/a \to \infty$ is singular, as no Stokes flow can exist around an infinite cylinder.

2.2 Simulation Methods

Powerful and efficient computational approaches play a fundamental role in applied science and engineering, enabling systematic studies of abroad range of soft matter systems. Numerical simulations allows us to cover a broad range of length scales and complexity and probe physical behavior of a system under a set of varying parameter conditions. Numerical techniques make it feasible to measure the system properties locally within molecular scales (meso-, nano- and even sub-nano scales), where experimental approaches are frequently limited. Here we describe a hybrid simulation method, multiparticle collision dynamics (MPC), in combination with molecular dynamics simulations (MD), which will be used in some parts of our work.

2.2.1 Molecular dynamics simulation

In classical mechanics the dynamics of point particles is governed by *Newtons equations of motion*. The equations of motion for a system consisting of N particles of masses m_i and the positions $\mathbf{r}_i$ $(i = 1, 2, ..., N)$ are

$$m_i \frac{\mathrm{d}^2}{\mathrm{d}t^2}\mathbf{r}_i = \mathbf{F}_i \tag{2.52}$$

where $\mathbf{F}_i$ is the net force acting on the i-th particle and is obtained from the potential energy U via $\mathbf{F}_i = -\nabla \mathrm{U}(\mathbf{r}_i)$. Molecular dynamics simulations provide a numerical solution of Newtons equations of motion for the particles in the system and thereby supplies the time evolution or dynamics of the system. An efficient and standard technique to integrate the equations of motion is the velocity Verlet algorithm that updates the positions and velocities of the particles at the time $t + \Delta t_{MD}$ according to [107]

$$\mathbf{r}_i(t + \Delta t_{MD}) = \mathbf{r}_i(t) + \mathbf{v}_i(t)\Delta t_{MD} + \frac{\mathbf{F}_i(t)}{2m_i}\Delta^2_{MD} \tag{2.53}$$

$$\mathbf{v}_i(t + \Delta t_{MD}) = \mathbf{v}_i(t) + \frac{\mathbf{F}_i(t + \Delta t_{MD}) + \mathbf{F}_i(t)}{2m_i}\Delta t^2_{MD} \tag{2.54}$$

This algorithm is time reversible and it has shown to provide a very reasonable energy conserving for conservative forces.

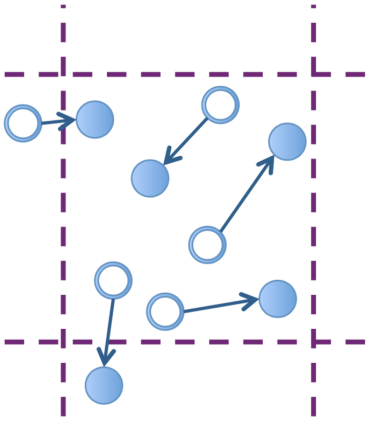

FIGURE 2.5: Streaming step of the multiparticle collision dynamics method (MPC) in two dimensions. The particles move ballistically.

2.2.2 Multiparticle collision dynamics

Multiparticle collision dynamics, MPC, is a mesoscale simulation method for fluids introduced by Malevanets and Kapral in 1999 [87, 88, 108]. In this technique, instead of calculating pair interactions between individual fluid particles, simultaneous multiparticle collisions are considered in collision cells. In MPC, mass, energy, and momentum are conserved on the collision cell level. Therefore, this simulation method captures both hydrodynamics, heat transfer and thermal fluctuations [88]. This means for example that the MPC fluid fulfills the compressible Navier-Stokes equations for a Newtonian fluid on not too small length scales [108, 109]. MPC consists of two steps: streaming and collision step.

Streaming step The fluid is composed of N point particles of equal mass m, with the positions $\mathbf{r}_i$ and the velocities $\mathbf{v}_i (i = 1, ..., N_s)$. In the streaming step, the particles move ballistically during a time increment h, which is called the collision time (Fig. 2.5). The new positions of the particles after streaming are

$$\mathbf{r}(t + h) = \mathbf{r}(t) + h\mathbf{v}(t) \tag{2.55}$$

If an external flow field is applied, an extra term has to be added.

Collision step In the MPC collision step, the particles interact among each other by a stochastic process. As we mentioned before, momentum has to be conserved locally for ensuring hydrodynamics, thus the collisions have to fulfill this condition. Therefore, we divide the simulation box into smaller cubic cells of size a, which are called collision cells, and sort all particles into these cells.

Imagine a box with a number of balls inside they may be billiard balls which collide elastically. If we shoot the balls towards each other to collide and compare their properties at times t_1, just before collision, and t_2, right after collision, we find that the total momentum and energy are conserved, and the center of mass velocity remains constant. Therefore, if we go to the center-of-mass reference frame and look at the collisions again,

the particles velocity vectors are rotated after collision. This is what is implemented in the MPC collision step. In the MPC collision step, the elastic collision of the particles is generalized and coarse-grained. Instead of considering only pair collisions, in the Stochastic Rotation Dynamics (SRD) version of MPC, the velocities of the particles in a collision cell are updated by rotating them around an arbitrary vector in the center-of-mass frame. Thereby, we first calculate the center-of- mass velocity for each cell:

$$\mathbf{v}_{cm,i}(t) = \frac{\sum_j^{(i)} m_j \mathbf{v}_j(t)}{\sum_j m_j}, \tag{2.56}$$

where $\mathbf{v}_j(t)$ is the velocity of particle j located in the cell i at time t. Then, we rotate the velocity of the j-th particle in the center-of-mass reference frame by an angle α (See Fig. 2.6 a).

$$\mathbf{v}_j(t+h) = \mathbf{v}_{cm,i}(t) + \Re(\alpha)[\mathbf{v}_j(t) - \mathbf{v}_{cm,i}(t)] \tag{2.57}$$

$\Re(\alpha)$ is the stochastic rotation matrix and can be defined by the Euler rotation matrix around the arbitrary unit vector $\mathbf{u} = (u_x, u_y, u_z)$.

$$\Re(\alpha) = \begin{vmatrix} c + u_x^2(1-c) & u_x u_y(1-c) - u_z s & u_x u_z(1-c) + u_y s \\ u_y u_x(1-c) + u_z s & c + u_y^2(1-c) & u_y u_z(1-c) - u_x s \\ u_z u_x(1-c) - u_y s & u_z u_y(1-c) + u_x s & c + u_z^2(1-c) \end{vmatrix} \tag{2.58}$$

where $c = \cos\alpha$ and $s = \sin\alpha$. For each cell and each MPC simulation step, we define a random rotation vector $\mathbf{u}$. By updating the velocities through this procedure, energy and momentum remain conserved at each cell before and after collision. Angular momentum is only conserved on average at larger scales, but not at the cell level. Andersen thermostat version of MPC does however conserve both linear and angular momentum at the cell level, but not kinetic energy [110].

2.2.2.1 Random shift

As previously mentioned, in the MPC collision step, the particles are sorted in collision cells and solely interact with the particles located in their cell. When the mean free path of the particles $\hat{\lambda} = h$ is smaller than the cell size a, the particles move slowly and have little chance to leave the cell. Moreover, if we change our reference frame and for example consider a frame moving with a constant velocity then the particles will see and interact with some diferent particles, which affects the results. Thereby, the Galilean invariance is destroyed. To overcome this problem, a random shift is applied to the collision grid before execution of the collision step [109, 111]. This can be implemented by shifting all particles along a random vector; its components are random numbers chosen from a uniform distribution in the interval $[a/2, +a/2]$. After the collision, the particles are shifted back to their original positions (Fig. 2.6 b).

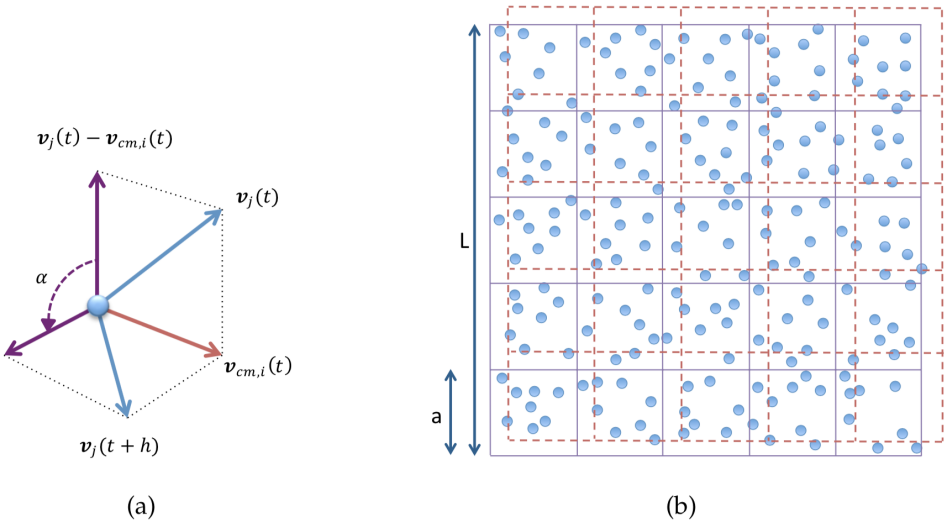

FIGURE 2.6: MPC collision step: (a) rotating the velocity of particle j in the i-th cell (vj(t) vcm,i(t)) in a reference frame co-moving with the center-of-mass by the angle α. (b) Random shift of the collision-cell grid. L is the simulation box size and a is the collision cell size

2.2.2.2 Hybrid algorithm

In the previous sections, two simulation algorithms were introduced: the MD and MPC methods. These two schemes can be combined to simulate complex fluids. Thereby, we simulate the fluid particles by MPC and the objects dissolved in the fluid by means of MD and also MPC. The interaction between solvent and solute particles has been modeled in two ways depending on the nature of problem. In phoresis for example, where the details of the surface interactions are important [112], MD interactions are considered. This is not the case in most polymer solutions where MPC interactions have shown to be very efficient in including HI interactions [113]. In this case, the velocities of the solute particles are updated in both, MD and MPC steps the positions in the MD streaming step and velocities in MPC collision step.

In case that a monomer size (segment size) as large as the collision cell size, i.e., $\eta = a$ is considered. Consequently in a collision cell, we typically do not have more than one monomer. Here we use the MPC coupling between the solvent and the solute such that the solvent particles can penetrate the monomer, which is placed in their collision cell. MPC treats the monomers in the same way as the fluid particles [111]. The center-of-mass velocity of a cell, with one monomer inside is

$$\mathbf{v}_{cm,i}(t) = \frac{M_k \mathbf{v}_k^m(t) + \sum_j^{(i)} m_j \mathbf{v}_j(t)}{M_K + \sum_j m_j}, \tag{2.59}$$

where M_k and $\mathbf{v}_k^m(t)$ are mass (which is larger than a fluid particle mass) and velocity of the k-th monomer, which is inside the i-th cell, respectively. Alternatively Kapral. [87, 111] introduced an interaction force between solvent and solute particles in the

collision step. In order to treat this force appropriately, we need to execute several MD integrations during one MPC step h [114].

As mentioned before, MD is indeed integration of the equations of motion, therefore, the shorter the MD time step, the more accurate the integration. On the other hand, choosing shorter time steps is less efficient. In our simulations, we consider $N = h/\Delta t$ MD time steps between two MPC collisions, with typically $N = 50$, which has shown to be good for the employed potentials.

2.2.2.3 Thermostat

Since the MPC algorithm conserves kinetic energy and momentum for the closed systems, we can calculate a uniform temperature via the equipartition theorem. We can set the energy to a desired value at the beginning of the simulation. Monitoring the energy (temperature) during the simulation is a way to check the validity of the MPC algorithm.

The application of an external field or specific boundary conditions might imply an input or output of momentum and energy which suppose a breakdown of the momentum and energy conservation in the system and consequently may change the temperature. Therefore, in order to fix the temperature, we have to thermalize the system [115]. The applied thermostat should conserve the momentum locally. Hence, we will use a cell-level thermostat to fix the temperature in each collision cell. At equilibrium, the velocity distribution function of the particles is a Maxwell - Boltzmann distribution.

2.2.2.4 Viscosity and dimensionless numbers

Transport properties in general, and viscosity in particular have been calculated by means of kinetic theory [109, 116] and simulations. The total viscosity η_s of a MPC fluid consists of two terms, the kinetic η_{kin} and collisional η_{coll} viscosity, i.e.,

$$\eta_s = \eta_{kin} + \eta_{coll} \tag{2.60}$$

In three dimensions [116, 117], these two terms can be calculated and are given by

$$\eta_{coll} = \frac{\sqrt{k_B T a^2/m}}{\hat{\lambda}} \frac{1-\cos\alpha}{18} \left(1 - \frac{1}{\rho}\right) \tag{2.61}$$

$$\eta_{kin} = \hat{\lambda}\sqrt{k_B T a^2/m} \left[\frac{1}{4 - 2\cos\alpha - 2\cos 2\alpha} \frac{5\rho}{\rho - 1} - \frac{1}{2}\right] \tag{2.62}$$

where ρ is the average number of fluid particles in a collision cell. For systems of small ρ, density fluctuations have pronounced affects and should be considered in the viscosity calculations. For the system of $\rho = 10$ these effects are negligible [116, 117].

Table 2.1: Parameters in simulation

Symbols	Description	Value in simulation units
L	simulation box size	$50a - 80a$
α	rotation angle	$130°$
h	MPC time step	$0.1\sqrt{ma^2/k_BT}$
Δt_{MD}	MD time step	$0.0001\sqrt{ma^2/k_BT}$
M	Monomer mass	$10m$
ρ	fluid particle density in cells	$10a^{-3}$
ϵ	Lennard-Jones potential depth	$1k_BT$
η_s	fluid viscosity	$8.7\sqrt{mk_BT}/a^2$
Re	Reynold number	uL/ν
Sc	Schmidt number	ν/D
Pr	Prandtl number	ν/ζ

In the coarse-grained modeling, here consider of all the particles in the system (solvent and solute particles) have been described as point particles. The nature of the approach does not permit a straightforward relation with physical units, such that comparisions are typically made of dimensionless relevant numbers. Thus we define the relevant length, mass, and energy, and then the rest of the system quantitiies can be referred to the ones,and time scales associated to the system:

· Length: a; MPC collision cell size
· Mass: m; mass of a fluid particle
· Energy: k_BT
· Time: ma^2/k_BT
· u: the velocity of the fluid with respect to the object (m/s)
· L: a characteristic linear dimension (m)
· D: the mass diffusivity (m^2/s)
· ν: the kinematic viscosity in units of (m^2/s)
· ζ: thermal diffusivity (m^2/s).

The parameters of our simulations in these units are listed in Tab. 2.1.

2.2.2.5 Boundary conditions

In simulating a physical system, we are limited by the number of particles to be considered, since two important factors prevent us to deal with massive systems: computer power and simulation time. For instance, it is impossible to simulate a bulk fluid system, or even a system with one Mol ($O(10^{23})$) of particles. By considering a small part of a bulk system, finite size effects may lead to deviation of the simulation results from the measured quantities. On the other hand, for systems in confinement, the particles close to the borders have a smaller number of neighbors than particles that are located in the middle of the box, therefore, they experience different forces. We circumvent surface effects by using *periodic boundary conditions*.

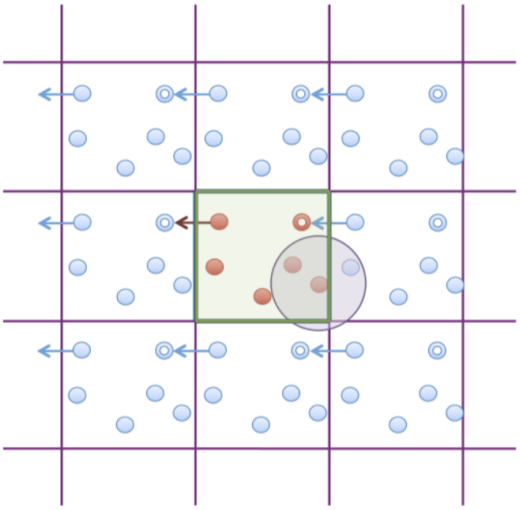

FIGURE 2.7: Illustration of periodic boundary conditions in two dimensions.

Using periodic boundary conditions, we replicate our simulation box in all directions and create a virtual infinite lattice of our system. When one particle moves in the simulation box, all images of that particle in other virtual boxes move in the same direction. If one particle leaves the simulation box, its image will enter the box through the opposite side, hence the number of particles remains constant during the simulation [107].

To reduce the numerical efforts, an interaction range for the particles is defined. Each particle can interact with all particles that are within its interaction range. The interaction range depends on the type of the interactions between the particles. Particles can also interact with the images, which are inside their interaction ranges, thus, surface effects will be eliminated. This is called minimum image convention (see Fig. 2.7). The interaction range should be less than $L/2$ to prohibit particles to interact with their own images.

Periodic boundary conditions in non-equilibrium situations

One of the main objectives in the work is to study of the system behavior response to shear flow. Shear flow can be imposed in the system in two ways. In the first one, the simulation box is placed between two confining walls, and the walls move in opposite directions with a constant relative velocity. The second approach is a modification of the periodic boundary conditions, by moving the upper and lower replicated simulation boxes in opposite directions (Fig. 2.8); this is called Lees-Edwards periodic boundary conditions [107]. In this situation, we create a velocity gradient in the simulation box perpendicular to the shear direction.

When a particle crosses one boundary, it comes back through the opposite boundary, but because of the movement of the boxes, the displacement of the particle and its image along the shear direction is $\delta x = u_x h$, where $u_x = \dot{\gamma} L$ is the shear velocity. The shear velocity is added to the velocity of the particle entering the original box. The average velocities of the particles in the shear direction is then a linear function of their positions in the shear gradient direction,

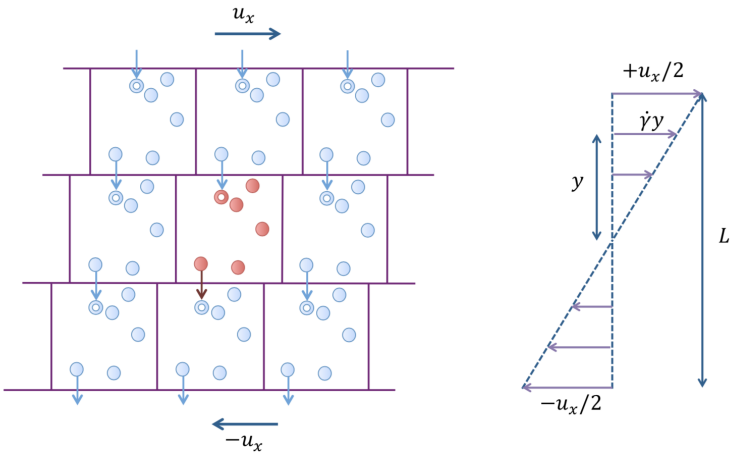

htb!

FIGURE 2.8: (a) Illustration of Lees-Edwards boundary conditions for a simulation box under shear flow. The upper and lower virtual boxes move in opposite directions with shear velocity u_x. If a particle enters the upper or lower boxes, the box velocity will be added to its velocity. (b) Velocity gradient; the flow velocity is a linear function of the position in y direction. $\dot{\gamma}$ is the shear rate.

$$\langle v_x \rangle = \dot{\gamma} y \tag{2.63}$$

where $\dot{\gamma}$ is the shear rate.

Note that although both periodic boundary conditions and Lee-Edwards boundary conditions were designed for MD, they have shown to be perfectly applicable in MPC.

2.2.3 Random MPC

To assess the effect of hydrodynamic interactions, the simulation can be carried out without HI, using as the method known as random MPC simulation of helix. In random MPC [118], each monomer is coupled not with an explicit solvent, but with an effective solvent momentum $\mathbf{P}$ which is directly chosen from Maxwell-Boltzmann distribution of variance $m\rho k_B T$ and a mean given by the average momentum of the fluid field - which is zero at rest, or $(m\rho\dot{\gamma}r_y^i, 0, 0)$ in the case of an imposed shear flow. The total center-of-mass velocity is then given by

$$\mathbf{v}_{cm,i} = \frac{M\mathbf{v}_i + \mathbf{P}}{m\rho + M} \tag{2.64}$$

with which the collision step in equation 2.56 is performed. Note that similarly to the MPC solvent, the polymer trajectory is sampled by MD and the interaction with the solvents is performed every collision time h. The random MPC solvent has therefore similar properties as the MPC solvent, except those associated with HI. The relevant parameters in both methods are the density ρ, the rotation angle α, and the collision time h which can be chosen be the same.

Chapter 3

Tumbling of quantum dots

.

3.1 Introduction

Colloidal quantum dots (QD) are semiconductor nanocrystallites with sizes typically ranging between 2 and 20 nm [119]. Although such nanocrystals already have the crystal structure of their bulk counterparts, their opto-electronic properties are strongly size-dependent. Due to quantum confinement, the QD band gap increases with decreasing QD size, which results in a broadband absorption spectrum with a size-tunable absorption onset and a narrow photoluminescence spectrum with a central wavelength that concomitantly shifts to shorter wavelengths [120]. A further tuning of the opto-electronic properties is possible by exploiting shape anisotropy [121, 122]. Rod-like nanocrystals, for example, preferentially absorb and emit light linearly polarized along their long axis [123, 124].

QD have gained attention as an optical material in lighting and display application [125, 126], solar energy conversion [127], photodetection [128, 129] and lasing [130, 131]. In addition, they have raised extensive interest as a luminescent probe in biomedical applications, such as biolabeling and immunoassays [132–136]. In almost all of these applications, QD are first dispersed in suitable liquid medium to form colloidal suspensions, and these QD dispersions are then processed to obtain a desired QD-coating or QD-composite. For example, QD dispersed in a polymer solution can be spun into aligned nanowires to produce waveguides with high polarization ratio [137]. Similarly, QD suspensions are used in other techniques such as electrohydrodynamic Jet Printing [138], screen-printing [139], or roll-to-roll printing [140] to control the deposition, distribution, and alignment. In all the above techniques, the rheological properties of the suspension play a crucial role not only to optimize processing conditions, but also to control the final alignment and ordering of nanoparticles [141, 142].

The rheological properties of a particular colloidal suspension depend on a number of factors such as colloid concentration, shape of the colloids, and colloid-colloid interactions.

While for very dilute solutions the colloid size has in principle no effect on the viscosity, for higher concentrated systems the effect of Brownian motion and its competition with the applied deformation rate strongly affects the flow properties and requires thus a detailed characterization of the colloid dimensions. Moreover, for nanocolloids the required stabilization in the form of colloid charge and an associated Debye length, or steric stabilization via grafted polymers or surfactants, will lead to an additional alteration of their effective hydrodynamic dimension [90, 143–147]. Two geometric parameters that are particularly effective in influencing the rheological properties of a suspension during deposition are the shape anisotropy of the colloid, specifically the hydrodynamic aspect ratio, and the polydispersity thereof, which also plays a crucial role in formation of the more complex structures during post processing [141, 142, 148–150].

A problem that arises when characterizing these parameters is that although many techniques are available to obtain information on colloid dimensions and polydispersity, such as electron microscopy or UV-Vis spectrometry for gold and silver nanocolloids[151–153], they only provide absolute physical dimensions of the colloids and not rheologically relevant hydrodynamic dimensions. For anisotropic colloids, this effect is amplified when their size decreases to the nanometer regime, since the ratio of the thickness of the stabilizing layer and the dimension of the colloidal particles diverges when approaching the dimensions of QD. In addition, these techniques provide statistically poor data due to the small sampling size. Other techniques, such as dynamic and depolarized dynamic light scattering that do provide statistically relevant hydrodynamic dimensions, are only suitable if the colloids are larger than the dimensions of the probe light [154, 155]. Furthermore, obtaining polydispersity using light scattering can be ambiguous due to the arising complex scattering patterns [91]. Given the typical sizes of QD (2-20 nm), investigations with scattering techniques therefore are usually not possible since each colloid acts as a Rayleigh point scatterer and hence does not provide any information about the colloidal shape.

One possibility to optically access the dimensions of QD is with linear flow dichroism (LFD). Dichroism measurements probe the polarization dependence of the turbidity that arises from scattering. The transmitted intensity is reduced due to scattering, while the scattered intensity depends on the polarization direction of the incident light for those cases where there is a preferred direction of orientation of shape-anisotropic colloids. Such a preferred direction of orientation can be induced when a colloidal suspension is subjected to a controlled flow field using a rheometer. Linear dichroism is then simultaneously probed using modulated polarized light [57, 156]. Colloids with an anisotropic shape tumble in such a flow field due to the differences in torque at either end of the colloid. For this, the hydrodynamic forces must be sufficiently large to overcome Brownian motion, and thus align the colloids on average towards the flow direction and rotate (tumble) them in the flow gradient plane. A sufficiently large Peclet number, $Pe = \dot{\gamma}/D_r$, to meet this requirement (where $\dot{\gamma}$ is the applied shear rate and D_r is the rotational diffusion coefficient of the colloid) can be achieved for nanocolloids by suspending the colloids in a high viscous, Newtonian matrix fluid. For the dimensions and rotational diffusivities of QD, viscosities on the order of 1-10 Pa·s are sufficient to

reduce Brownian rotational diffusion allowing to reach high Pe within an experimentally accessible shear rate-range of 1-10 s^{-1}.

Pioneering works from Fuller and co-workers [54–57, 156] on colloids of micron and sub-micrometer dimensions have shown that, using transient flow dichroism data, both the hydrodynamic aspect ratio as well as polydispersity can be obtained simultaneously. Recently, LFD has been used by Vermant and coworkers to push the colloid diameter measurement limit down to 50 nm, using shape anisotropic gold nanocolloids. Although their minimum length scale was close to the Rayleigh scattering regime, they could still rely on the localized surface plasmon resonance of gold nanocolloids to resolve scattering along and across the length of nanocolloid to obtain dichroism and orientation angle [58]. Information about hydrodynamic aspect ratio and polydispersity for all the above cases was obtained by fitting the experimental LFD data to a simplified Smoluchowski equation with the assumptions of a very high Pe regime and near spherical colloids.

In this chapter, we push the detection limit of LFD further down to particle dimensions of 10 nm to resolve the tumbling motion of QD, and extend the theoretical analysis to arbitrary values for Pe and arbitrary aspect ratios. We exploit the fact that QD retain their crystalline lattice structure even on their small dimensional scale. Measurements of the strong internal anisotropy of the lattice can be used as a 'pointer' for the colloid orientation, even for QD with a small shape anisotropy.

As dichroism is a measure of the change in the imaginary part of the refractive index, the oriented crystalline lattice of QD during tumbling leads to a significant change in dichroism even for the small dimensions of QD. Typically, dichroism values of around 1e-6 to 1e-5 represents a good signal-to-noise ratio [57, 156]. Recently, tumbling was captured with dichroism values reaching 1e-7 for plasmonic gold rods and disks [58]. In this article we will show that with a low signal-to-noise ratio QD tumbling can be detected even at dichroism values of 1e-8. Here, we show that linear flow dichroism can be used to determine the orientation and thus rotary motion of QD, from which both their hydrodynamic aspect ratio and polydispersity are obtained, quantities that have not yet been determined for QD by any other technique. As the QD are very small, reaching the very large Pe regime is experimentally not feasible. This implies that the existing approximations of tumbling theories valid in the high Pe regime [58] are not applicable. Therefore, we here present the use of the full Smoluchowski equation, which is numerically solved to fit transient LFD data to obtain both hydrodynamic aspect ratio and polydispersity of QD at intermediate Peclet numbers where Brownian motion cannot be ignored.

3.2 Experimental Section

Synthesis of QD

$CuInS_2$ quantum dots (CIS QD) were synthesized through a method described before by Dierick et al [157]. To obtain the relatively large, tile-shaped CIS nanocrystallites used

Sample	description	a/b	$\bar{p}_{\mathrm{TEM}}$
A	CdSe/CdS nanorod	17.3/4.6	3.76
B	CdSe/CdS nanorod	11.8/5.6	2.10
C	CdSe/CdS nanorod	12.1/3.8	3.18
D	$CuInS_2$ tile	10.0/19.19	0.52
E	$CuInS_2$ tile	7.77/15.38	0.50

TABLE 3.1: Physical dimensions of the five analyzed samples of quantum dots obtained from TEM images. Here a refers to the radial length, b to the axial length, and $\bar{p}_{\mathrm{TEM}}$ to the averaged aspect ratio. The lengths are given in nm.

here, 1 mmol of $Cu(acac)_2$ (0.262 g) 1 mmol of $In(acac)_3$(0.412 g) and 2.1 mmol (0.067 g) elemental S were added to 30 mL of 1-octadecene in a three-neck flask. This flask was then attached to a Schlenk line, after which the heterogeneous mixture was flushed with nitrogen for 1 h. Next, 2 mL of oleylamine was injected, followed by increasing the temperature to 240 ^{o}C. An infrared heating lamp was used to fix the heating rate at 80 ^{o}C/min. Upon reaching 240 ^{o}C, the reaction was allowed to continue for 1 h. After this period, the flask was cooled down using a water bath, and the CIS QD were washed using toluene and ethanol. The nanocrystallites were then collected by centrifugation and the brown-red supernatant was discarded. The nanocrystallites pellet was redissolved in toluene and the resulting clear black solution was stored in the fridge. Under these synthesis conditions, we obtained tile shaped CIS QD (samples D and E in table 3.1).

CdSe/CdS nanorods (samples A, B and C in table 3.1) were synthesized according to an established procedure [158]. First, CdSe cores (seeds) were synthesized in trioctylphosphinoxide (TOPO), using a mixture of cadmium oxide (CdO), octadecylphosphonic acid, and trioctylphosphineselenide (TOPS) as precursors. To synthesize the CdSe/CdS nanorods, the CdSe seeds were co-injected with a TOPS precursor into a hot reaction mixture containing octadecyl- and hexylphosphonic acid, TOPO and CdO.

3.2.1 Linear flow dichroism measurements

Linear flow dichroism was measured using a home-built optical train combined with a Couette flow geometry in a stress controlled rheometer, MCR300 (Paar Physica, Austria) [58, 159]. The optical train used to measure dichroism was designed following the rules laid out in Ref. [156] and is composed of a He-Ne laser (λ= 632.8 nm, 10 mW), a Glen-Thompson polarizer at 0° (Newport, USA), a photoelastic modulator at 45° (PEM, Beaglehole Instruments, New Zealand), a quarter-wave plate at 0° (Newport, USA), and a double prism to bend the horizontal light in the vertical direction such that it passes through the Couette cell along the shear-gradient plane, probing the tumbling of colloids. The scattered light emerging from the Couette cell after passing through the sheared sample is collected using a photodiode. The Couette cell was custom built with quartz disks at the top and bottom of the cell to provide optical access and to eliminate scattering from the air-liquid interface. The Couette cell has an inner radius of 16.95 mm, an outer radius of 17.95 mm, and a height of 21 mm. The photodiode

provides two outputs, a direct current (DC), which provides the intensity of the scattered light, and the alternating current (AC), which contains the intensity fluctuations due to the colloids tumbling. The AC signal is passed through a low-pass filter and sent to two lock-in-amplifiers (Stanford Research Systems Model 830) together with the signal from the PEM. The first (R_1) and the second (R_2) harmonic outputs from the lock-in-amplifiers, along with the DC signal, are used to obtained both the magnitude of dichroism and the orientation angle. The dichroism is given by [156]

$$\Delta n'' = -sgn(R_2)\tanh^{-1}\left\{\frac{1}{2}\sqrt{\frac{R_1}{-J_1(A)}+\frac{R_2}{-J_2(A)}}\right\}\times\frac{\lambda}{2\pi l} \quad , \tag{3.1}$$

where λ is the wavelength of light (632.8 nm), l is the optical path length (21 mm), J_1 and J_2 are Bessel functions of the zeroth order, and A is a constant that depends on the photoelastic-modulator, such that $J_0(A) = 0$. Similarly, the orientation angle, that is, the average angle of alignment of the colloids relative to the flow direction, is given by

$$\chi = \frac{1}{2}\tan^{-1}\left\{\frac{R_1/\mathrm{J}_1(A)}{R_2/\mathrm{J}_2(A)}\right\}. \tag{3.2}$$

To reduce Brownian motion and to increase Pe within the experimentally accessible shear rates (0.1-10 s^{-1}), the QD were dispersed in mineral oil with a viscosity of 4.9 Pa·s. The setup was calibrated using the same mineral oil without QD. All experiments were conducted at 22 ^{o}C.

Linear flow dichroism experiments were conducted on rod-like and disk-like quantum dots as those shown in fig 3.1, and whose physical dimensions, determined using TEM, are given in table 3.1. Note that these physical dimensions only represent core particle dimensions without taking into account other additional characteristics such as polymer coatings, or asymmetric charge distributions when dispersed in a liquid, or bullet shape for prolate QD and flat disk shape for oblate QD. These additional factors will be reflected in the hydrodynamic particle dimensions, which are crucial for determining the rheological properties of QD suspensions.

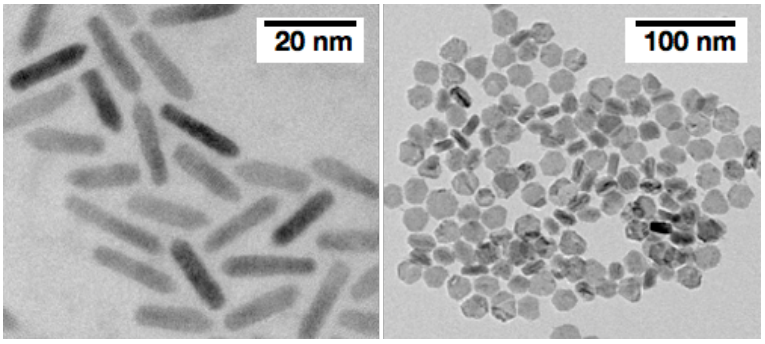

FIGURE 3.1: Example of transmission electron images of rod-like (sample A) and disk-like (sample D) quantum dots.

3.3 Results and discussion

3.3.1 Linear flow dichroism (LFD)

LFD is one of the most effective techniques to determine the hydrodynamic aspect ratio and polydispersity of shape anisotropic colloids. Typically, a non-spherical colloidal particle in a shear flow performs tumbling or kayaking motions (Jeffrey orbits) if hydrodynamic forces are sufficiently large to overcome Brownian motion. The hydrodynamic forces result in a torque on the colloid that causes it to periodically tumble in the flow gradient plane. Such periodic orientational motions are referred to as Jeffery orbits [160]. For negligible Brownian motion, the time period T for a tumbling event is given by,

$$T = \frac{2\pi}{\dot{\gamma}} \left\{ p + \frac{1}{p} \right\} \tag{3.3}$$

where p is the colloids hydrodynamic aspect ratio [160]: $p > 1$ for rod-like colloids, $p = 1$ for a sphere, and $p < 1$ for disk-like colloids. For an anisotropic colloid, the rotational velocity during a tumbling cycle is not constant since the colloid resides longer at orientations corresponding to lower hydrodynamic torques, which occurs when the long axis is parallel to the shearing direction. However, since the torque on any finite size colloid will not vanish completely, the colloid will eventually rotate out of this preferential position to quickly flip and approach this position again.

For long times and/or multiple colloids, an average tumbling period is determined from the overall orientational distribution function (ODF), which quantifies the probability for a colloid to attain a certain orientation at a certain time. At rest, Brownian force causes the colloid orientation to be uniformly distributed, so that each orientation is equally likely to occur. However, at the start-up of shear the colloid rotates quickly into the preferential flow aligned orientation and then performs its tumbling rotation. For samples with monodisperse colloids, and in the limit where Brownian motion can be neglected (limit of $Pe \to \infty$), this synchronised tumbling motion will maintain its correlation indefinitely under an applied shear force. However, when Brownian motion is significant, and for samples with colloids that are polydisperse with respect to their aspect ratio, the tumbling motion, is averaged over all colloids being present in the sample, loses its correlation in time, leading to phase mixing. At a fixed Pe, colloids with smaller hydrodynamic aspect ratios tumble faster than their larger counter parts, since the tumbling period is directly proportional to the hydrodynamic aspect ratio. As time progresses, the phase mixing dampens the optical response of the ODF (while maintaining the average tumbling period T) and eventually approaches an apparent steady state, corresponding to an average orientation angle of the colloid's long axis and the flow direction between 45° (isotropic) and 0° (perfect alignment along the flow direction) depending on Pe. Perfect alignment is only achieved when increasing the shear rate to infinitely large values, where Brownian motion can be neglected. It should be noted that, in the hydrodynamically dilute regime, the magnitude of the dichroism is a linear function of the concentration, whereas the orientation angle is independent of

concentration. Because of this, the averaged orientation angle is the preferred quantity to analyse and to obtain the hydrodynamic aspect ratio and polydispersity.

3.3.2 Smoluchowski equation for tumbling of colloids

The Smoluchowski equation describes the time evolution of the probability distribution function $P(\hat{\mathbf{u}}, t)$ of the unit vector $\hat{\mathbf{u}}$ that characterizes the orientation of a colloid: $\hat{\mathbf{u}}$ is pointing along the long axis of the rod, or pointing along the normal to the face of a disk. For very dilute dispersions, where interactions between the colloids can be neglected, the Smoluchowski equation reads

$$\frac{\partial}{\partial t} P(\hat{\mathbf{u}}, t) \;=\; D_r \, \mathcal{R}^2 \, P(\hat{\mathbf{u}}, t) - \mathcal{R} \cdot \{ \, \omega \, P(\hat{\mathbf{u}}, t) \, \} \;, \tag{3.4}$$

where $\mathcal{R}(\cdots) = \hat{\mathbf{u}} \times \nabla_{\hat{\mathbf{u}}}(\cdots)$ is the rotation operator (with $\nabla_{\hat{\mathbf{u}}}$ the gradient operator with respect to the Cartesian coordinates of $\hat{\mathbf{u}}$). The above Smoluchowski equation (eq 3.4) does not include interactions between the colloidal particles, and therefore applies only to very dilute suspensions.The first term on the right hand-side accounts for orientational Brownian motion, and the second term describes the effect of shear flow, where ω is the resulting colloid angular velocity. This angular velocity corresponds to Jeffery orbits [160], and can be written in vector form as

$$\omega \;= \dot{\gamma} \, \frac{p^2 - 1}{p^2 + 1} \, \hat{\mathbf{u}} \times (\mathbf{\Gamma} \cdot \hat{\mathbf{u}}) + \; \dot{\gamma} \, \frac{2}{p^2 + 1} \, \hat{\mathbf{u}} \times (\mathbf{\Omega} \cdot \hat{\mathbf{u}}) \, . \tag{3.5}$$

For simple shear, with flow in the x-direction and the velocity gradient in the y-direction, the velocity gradient tensor $\mathbf{\Gamma}$ has been shown in Eq. 2.1, the rotational part of the velocity-gradient tensor in Eq. 2.3 in Sect. 1.2.1.1.

In the following, we explore the effect of aspect ratio, Peclet number, and polydispersity on the colloid orientation in a flow field using the full numerical solution of the Smoluchowski equation (eq 3.4). This will later allow us to fit actual experimental data to the corresponding numerical solution. Earlier related comparisons were performed by Mason *et al.* [161], who performed experiments with millimeter sized rod-like colloids and obtained an almost exact fit to experimental data using a reduced Smoluchowski equation where Brownian motion was neglected. For colloids with dimensions in the millimeter to micrometer range, large Pe can be achieved with relative ease using standard rheometers with flow rates and matrix viscosities within the experimentally accessible range [54–57]. The Mason approximation is valid in the infinite Peclet number limit, but for intermediate Pe, typical for smaller colloids, the probability distribution function for the rod orientation can only be obtained by numerically solving the full Smoluchowski equation.

3.3.3 Dependence of the orientation angle on the strength of the applied flow

The tumbling of the orientation angle of a monodisperse sample of rods with small and a larger aspect ratio is displayed in fig 3.2 as a function of the strain. The Mason approximation (see supporting information for the detailed implementation) is plotted together with the numerical solution of the Smoluchowski equation (eq 3.4), for values of Pe ranging from $10^2 - 10^{10}$. Mason's approximation shows a perfect periodic tumbling motion where the orientation angle oscillates between $\pm\pi/4$ degrees with a period that is a function of the aspect ratio as given by the Jeffery expression in eq 3.3. The solutions of the Smoluchowski equation shown here correspond to finite values of Pe and thus show phase mixing, where the amplitude of the oscillating orientation angle χ decreases with increasing strain. This damping becomes stronger both with Pe and aspect ratio. The values of the Peclet number at which Mason's approximation (eq 3.4 without the first term) can be considered valid are surprisingly large, and these values increase with the aspect ratio. For rods with small aspect ratio (close to spheres) the tumbling in fig 3.2a shows reasonable agreement with Mason's approximation at $Pe = 10^4$, while for $p = 4$ in fig 3.2b agreement occurs only at $Pe = 10^{10}$, and for $p = 7$ in fig 3.2c Mason's approximation does not come close to the real values, even at enormously high shear rates.

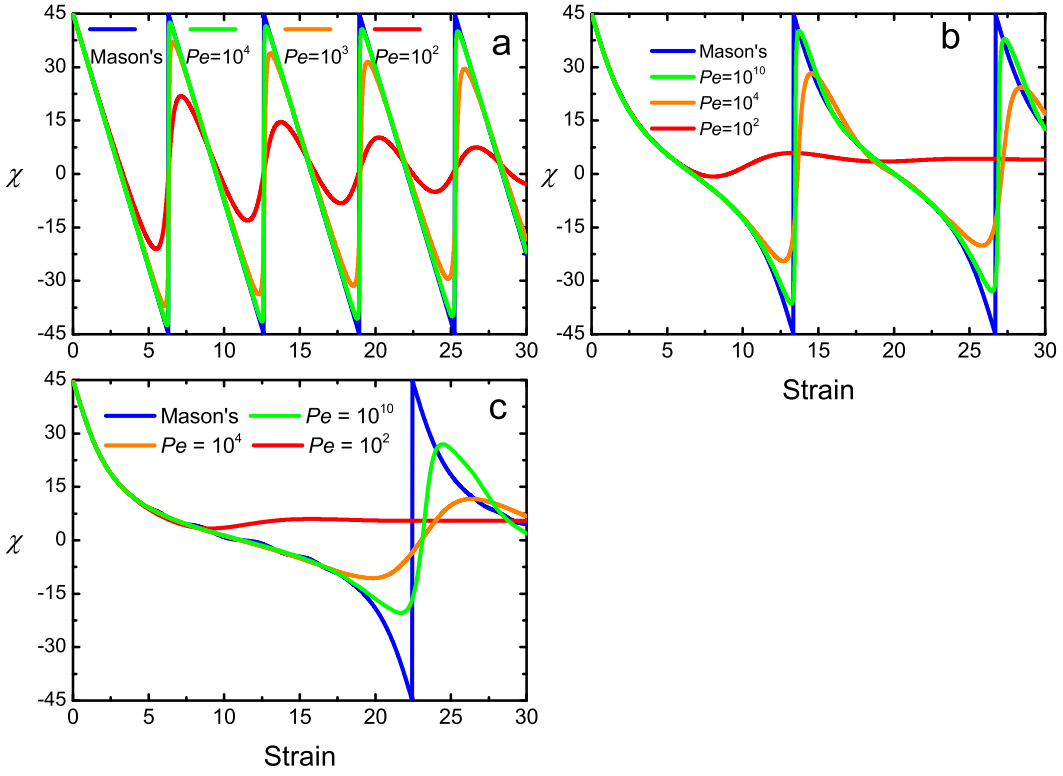

FIGURE 3.2: The orientation angle as a function of strain calculated from the Smoluchowski equation in eq 3.4 at large values of Pe and compared to Mason's approximation, for aspect ratios a) $p = 1.1$, b) $p = 4.0$, and c) $p = 7.0$.

The damped evolution of the orientation angle obtained from the numerical solution of the Smoluchowski equation at smaller values of the applied shear rate are shown for $p = 2$ in fig 3.3. For large enough values of Pe, the oscillations of the orientation angle eventually vanish at large strain values reaching a steady orientation angle of $\pi/4 > \chi_s > 0$. The amplitude and the number of oscillations before reaching the steady state also decrease with decreasing Pe, eventually disappearing. The strain at which the steady behaviour is reached also decreases with Pe, as well as the steady orientation values. In the case shown in fig 3.3, it can be seen that for $Pe = 50$ there is on average still one single oscillation observered, while lowing the flow rate to $Pe = 10$ the rotational diffusion dominates the flow and the rods reach the steady orientation angle even before the first tumbling event is completed.

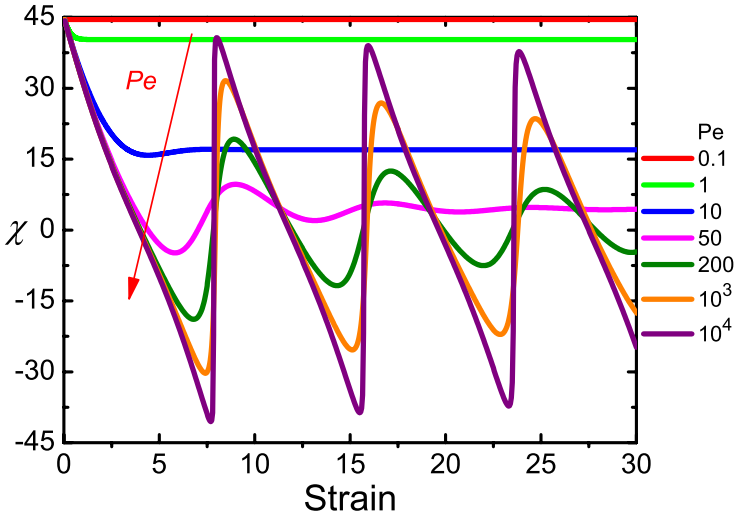

FIGURE 3.3: Orientation angle as a function of strain for $p = 2$ showing damped oscillations in a large rage of Pe values.

Figure 3.4 shows measurements of how the asymptotic orientation angle χ_s for very large strains, in the stationary state, varies as a function of Pe. Very small values of Pe (typically $Pe \lesssim 1$) show very small orientation approaching $\chi_s = \pi/4$, which corresponds to the isotropic state. At larger values of Pe, χ_s shows a clear power law decay with Pe. Solutions of the Smoluchowski equation are compared in fig 3.4 with hydrodynamic simulation results by *et. al.* [7] who used multiparticle collision dynamics coupled to molecular dynamics to determine the averaged asymptotic angles χ_s as a function of Pe for a bead model of rod like colloids with $p = 10$. The simulations showed an approximate power law behaviour $\chi_s \propto Pe^{-0.46}$ for $Pe > 5$, behaviour also observed previously for flexible polymers in shear flow [162]. Our numerical results in fig. 3.4 are in good agreement showing the similar power law, for aspect ratios $p = 10$ and $p = 20$. Important to note is that the agreement of our results with power law scaling does not require any additional fitting parameter. Numerical results for a smaller aspect ratio of $p = 2$ in fig 3.4 show however a faster decrease of χ_s. This steeper slope reflects the fact that a rod of small aspect ratio is easier to orient towards the flow axis than large ones at the same Pe. Interestingly, from fig 3.4 it can be seen that for large enough aspect ratios, the asymptotic orientation angles do not depend on the colloid aspect ratio. We note

that our theoretical prediction obtained numerically from the Smoluchowski equation (in eq 3.4) requires orders of magnitude less computing time than the simulation results.

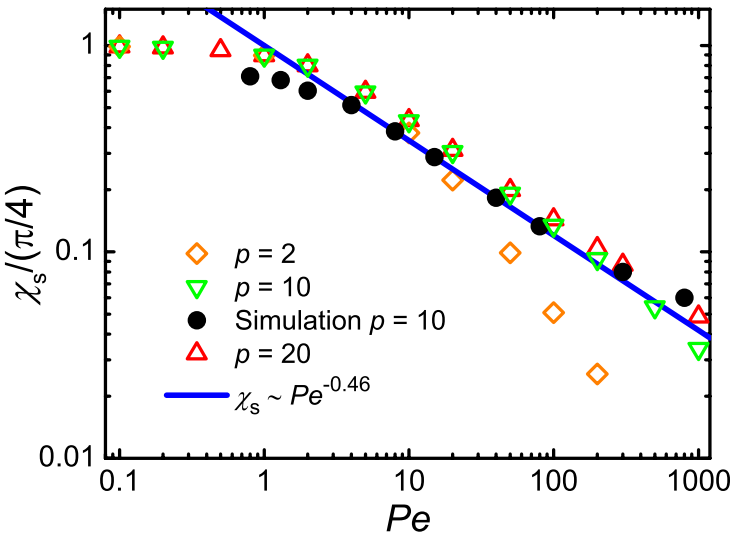

FIGURE 3.4: Normalized asymptotic orientation angle (χ_s) as a function of Pe for $p = 2, 10$ and 20, compared with the hydrodynamic simulation results for $p = 10$ from Ref. [7].

3.3.4 Dependence of the orientation angle on the colloid aspect ratio

The aspect ratio of the rods has strong and non-trivial effects on the angular velocity and the time dependent orientation angle in shear flow. As can be seen in fig 3.5, the intrinsic shape of the curve changes when the aspect ratio is increased, given a constant value of Pe. On average, the colloids spend more time oriented in the flow direction when the aspect ratio is larger. At the same time, the oscillations show larger damping for larger aspect ratios. Comparing fig 3.5a and fig 3.5b, the amplitude and number of the oscillations at the same aspect ratio is reduced as the Peclet number is decreased. Figure 4b clearly indicates that the aspect ratio (for $p > 3$) has only a small influence on the asymptotic angles χ_s for large Pe. This agrees with the conclusions previously derived from fig 3.4.

The period of the tumbling rotations can be characterized via the first half period $\tilde{T}_{12}$, which can be obtained from the strain at which the first minimum of the averaged orientation angle is found, as seen for example in fig. 3.5. The strains at these first half-periods are displayed in fig 3.6 as a function of the aspect ratio and the Peclet number, and are compared with the prediction provided by Jeffery's theory in eq 3.3 [160]. Figure 3.6a shows how the full Jeffery approximation gradually deviates from the solution of the full Smoluchowski equation with increasing aspect ratio and decreasing Pe. Furthermore, Fig.3.6a shows that the rotation period at large applied shears grows approximately with $(p + 1/p)$ as predicted by Jeffery, while it is becames almost independent of the aspect ratio for the smallest applied shears. In order to analyze the dependence of the

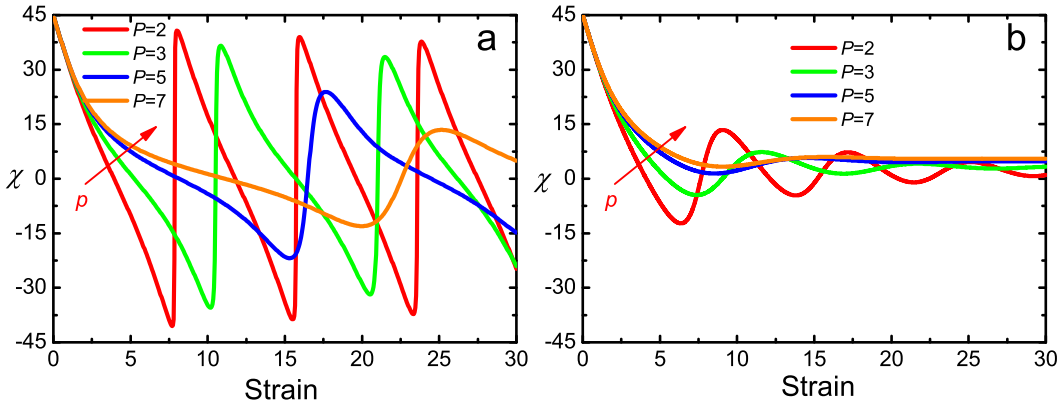

FIGURE 3.5: Orientation angle as a function of strain at various aspect ratios for a) $Pe = 10^4$ and b) $Pe = 10^2$.

actual rotation period with the Peclet number, it is illustrative to display the half-period strains normalized by the corresponding Peclet number, this is also the period, times the rotational diffusion factor, which is constant for each value of the aspect ratio, as shown in Fig. 3.6b. The Jeffery approach considers no thermal motion at all, such that rotational diffusion can be consider to be vanishing. This means that direct comparison is not really possible, although the dependence with the applied shear and aspect ratio can still be contrasted. The decay with the Peclet number rotation period shows to be a power law in Fig. 3.6b, but with an exponet smaller than one in the presence of thermal noise, a decay which shows to be slower the larger the aspect ratio.

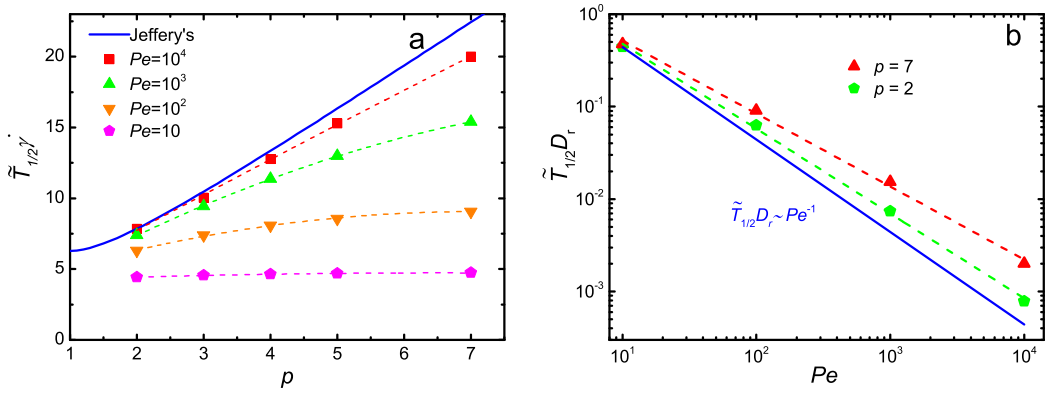

FIGURE 3.6: a) Strain at the first half-period as a function of the aspect ratio p for several values of Pe. Solid line correspond to the prediction by the Jeffery orbits in eq 3.3, and the dashed lines are guides to the eye. b) Rotation half period adimensionalized with the rotational diffusion as a function of the Peclet number for two values of the aspect ratio. Solid line indicates the inverse linear dependence predicted by Jeffery, and dashed lines indicate power law decays with exponents smaller than one.

3.3.5 Dependence of the orientation angle on sample polydispersity

In addition to the effects of shear rate and aspect ratio on the temporal behaviour of the orientation angle, also the sample polydispersity can have a large influence. Although

we consider the effect on dilute samples, where no interactions are taken into account, measurements are performed which probe an average over a large number of colloids. Realistic dispersions are sometimes quite polydisperse, containing a wide variety of, for example, rods with different lengths. To analyze the effect of polydispersity, the Smoluchowski equation 3.4 is solved for a number of different aspect ratios, and the resulting orientation angles are then averaged according to a log-normal distribution of the aspect ratio. The parameter σ that quantifies the degree of polydispersity is the width of the log-normal distribution (see the supplementary information for more details). The effect of polydispersity is shown in fig 3.7 as a function of strain for a fixed $p = 2$ and for two Peclet numbers $Pe = 10^4$ and 10^2. Increasing polydispersity σ lead to the expected increased damping of the oscillations, and the effect is stronger for larger Pe, as can be seen by comparing fig 3.7a and fig 3.7b. Since the period of revolution of a colloid depends on its aspect ratio, each colloid length will tumble with a different frequency which clearly results in phase mixing.

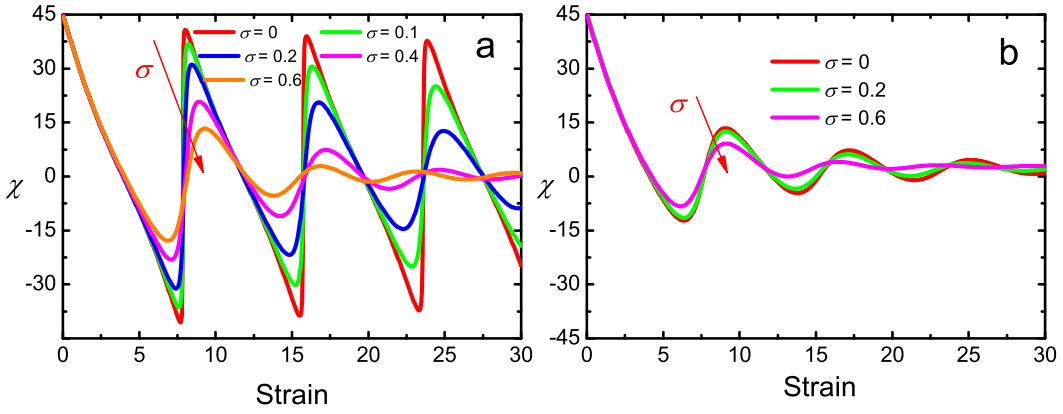

FIGURE 3.7: Orientation angle as a function of strain for varying polydispersity and $p = 2$ at a) $Pe = 10^4$ and b) $Pe = 10^2$.

3.3.6 Numerical fit to experimental dichroism data

The previously discussed features of the temporal evolution of the orientation angle (effect of shear rate, aspect ratio, and polydispersity) allow us to fit our numerical results to experimental data. The three related parameters Peclet number (Pe), polydispersity (σ), and aspect ratio (p), which are in principle unknown for the our QD suspensions, can therefore be determined. For the expected aspect ratio range of the QD measured in this study, and the experimentally accessible Pe, the tumbling period T will exhibit only a weak dependence on the Peclet number as can be concluded from our numerical results shown in fig 3.2, fig 3.3, and fig 3.6, as well as on the polydispersity σ as shown in fig 3.7. We therefore initially fit the four measured shear rate data to the same tumbling period T to obtain a unique estimated Pe and p (see fig 3.8) for the sample A. Subsequently, the following fitting procedure is used to obtain the hydrodynamic aspect ratio and polydispersity:

1. Experimental determination (for example via microscopy) whether the colloids are prolate (rod-like with $p > 1$), or oblate (disk-like with $p < 1$).

2. First estimation of the colloid aspect ratio (p) from the first half-period ($\tilde{T}_{12}$) of the time dependent average orientation angle.

3. Estimation of the value of Pe from the asymptotic orientation angle χ_s.

4. Solution of Smoluchowski equation using the previously obtained p and Pe and assuming $\sigma = 0$, and subsequent optimiztion of the agreement of $\tilde{T}_{12}$ and χ_s by iteratively modifying the values of Pe and p.

5. Improving the matching of the oscillation amplitudes by solving the Smoluchowski equation with higher values of the polydispersity σ.

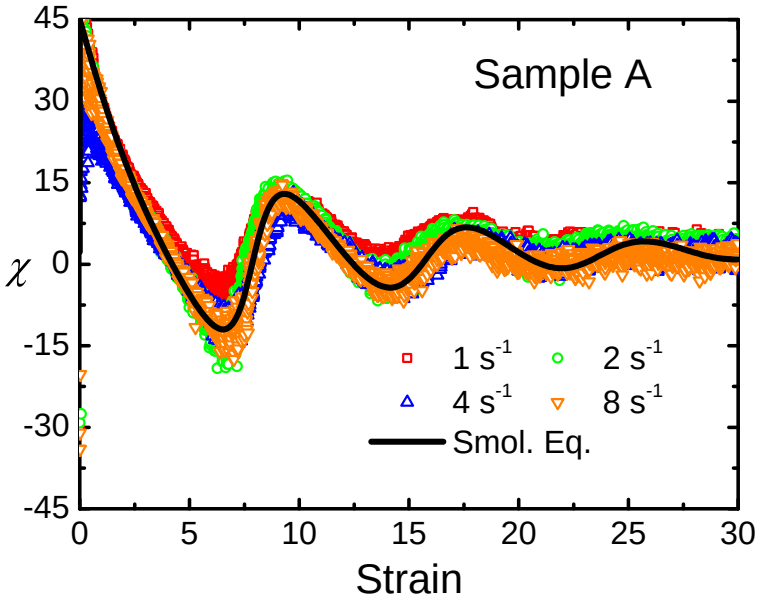

FIGURE 3.8: Comparison of experimental orientation angle as a function of strain for sample A to the prediction given by Smoluchowski equation (eq 3.4) with $p = 2.1$, $\sigma = 0.08$ and $Pe = 100$.

A comparison of fitting result to experimental data for sample A is shown in fig 3.8, where a good agreement of the tumbling period, the asymptotic behaviour at larger strains, and the decay in oscillation amplitude can be observed. Fitting curves obtained using the same method for other samples are shown in fig 3.9 where the method is applied for both, rod-like QD (samples B, C) and disk-like QD (samples D, E). The fitted values of p, σ, and Pe for both rod and disk shape quantum dots are are listed in table 3.2.

The hydrodynamic aspect ratio obtained from LFD is consistently smaller than the aspect ratio obtained from TEM, as shown in table 3.2. This is expected as our QD colloids are coated with a stabilizing polymer layer that decreases the effective $\bar{p}$, and which is detected by LFD but not with TEM and explains the difference between the $\bar{p}$ from LFD and $\bar{p}_{\mathrm{TEM}}$ data for the prolate particles in table 3.2. For the oblate QD a uniform polymer layer alone can not explain the difference between the LFD and TEM results. A similar finding for oblate particles has been reported before [58]. A plausible explanation for the discrepancy in case of the oblate QD is that the stabilization polymer layer is not homogeneously distributed over their surface. It seems that the polymer

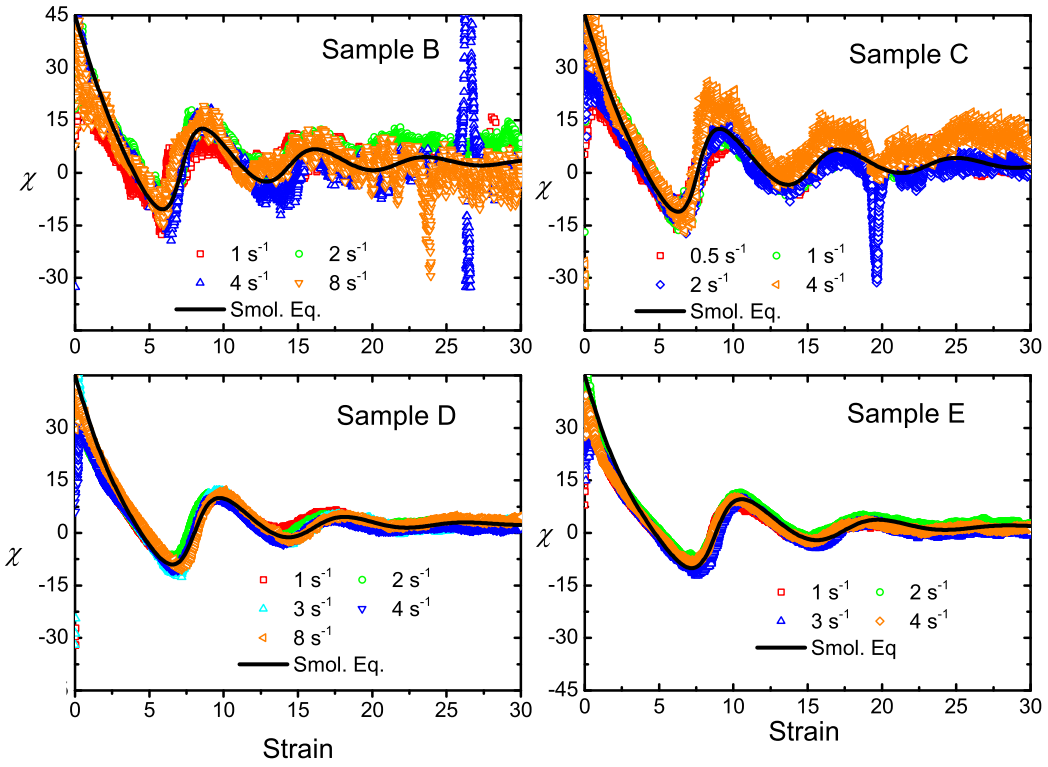

FIGURE 3.9: Orientation angle as a function of strain comparing experiments and Smoluchowski equation for samples B-E.

Sample	$\bar{p}$	σ	Pe	$\bar{p}_{\mathrm{TEM}}$
A	2.10±0.10	0.08±0.05	100	3.76
B	1.80±0.10	0.07±0.04	70	2.10
C	2.00±0.14	0.07±0.05	90	3.18
D	0.45±0.02	0.07±0.02	100	0.52
E	0.40±0.03	0.06±0.02	160	0.50

TABLE 3.2: Estimated average hydrodynamic aspect ratio, polydispersity, and Peclet number. The last column shows the physical aspect ratio from TEM for comparison.

coating at the edges of the oblate QD is slightly denser as compared to the flat face, although there is no independent proof that sustains this observation. However, this supports the necessity of independent direct measurements of the hydrodynamic aspect ratio as with the LFD presented here, as not even the knowledge of the protective layer allows to fully theoretically predict the effective $\bar{p}$. But it should also be noted that the experimental LFD data have a rather large scatter, which is connected to the extremely small size of the QDs, leading to a small signal to noise ratio. This large scatter in the experimental data does not permit to make independent fits for each applied shear rate separately, but only to provide an average fit which corresponds to an averaged shear rate. In spite of this, a combination of experimental LFD and the fitting procedure using the Smoluchowski equation at intermediate Pe gives a robust estimate of the hydrodynamic aspect ratio and polydispersity for shape anisotropic QDs.

3.4 Summary

Combining experimental rheo-optics and the numerical solution of the Smoluchowski equation is a powerful approach to characterize the effective aspect ratio of anisotropic colloidal systems for which other techniques fail, as is the case with quantum dots (QD) dispersed in a liquid. For this the time evolution of the orientation angle of dilute suspensions of non-spherical colloids upon inception of shear flow is monitored by means of a polarisation modulation method that probes linear flow dichroism (LFD). The time evolution of the orientation angle depends on three parameters: the Peclet number Pe, the hydrodynamic aspect ratio p, and the particle polydispersity σ. Numerical solutions of the rotational Smoluchowski equation for prolate and oblate colloids, including both Brownian motion and shear flow, reveal the importance of these parameters on the temporal evolution of the degree of alignment as quantified by the orientation angle. Based on this an analysis procedure for experimental LFD data is proposed for arbitrary values of Pe, p, and σ. Interestingly, although the LFD signal to noise ratio is low due to the small size of the QD, the hydrodynamic aspect ratio and polydispersity of QD can still be obtained reliably, which has been shown here for both prolate and oblate QD. We expect that this optical technique probing dichroism, and the data analysis based on numerical solutions of the orientational Smoluchowski equation, will be widely used for the characterization of the hydrodynamic properties of single particles ranging in sizes down to those of QD. We also anticipate that by matching the refractive index of the suspending medium to that of the particles, the method will soon be extended to the characterization of dense systems, where particle-particle interactions becomes important.

Chapter 4

Helix in shear flow

4.1 Motivation

Objects whose mirror image can't be superimposed with the original one by rotation are called chiral. Most biological organisms and molecules are totally or partially chiral which significantly influence their chemical and physical behaviors. Motion and kinetics of chiral objects are largely determined by their spatial anisotropy since chirality leads to a coupling between the translational and rotational degrees of freedom. Objects with different handedness symmetry might rotate, drift, or form structures along opposite directions under non-equilibruim conditions.

Recently, a lateral drift of screw-like objects in shear flows was experimentally demonstrated for bodies with a linear extension of the order of centimeters [163], millimeters [11], and micrometers [10]. Clemens *et al* [164] have experimentally demonstrated separation of racemic mixtures by exposing left and right-handed chiral molecules to a rotating electric field. The control of actively moving nano-structured propellers was studied by Ghosh and Fisher [95]. D'Urso *etal* [165] described the formation of chiral assembles made of achiral components in a vortex flow and showed that stirring shifted the equilibrium of a racemic mixture towards the side chosen by the vortex chirality.

On the theoretical side, Brenner [166] formulated the Stokes resistance of an arbitrary particle shape and discussed the possibility of migration of helicoidal particles in shear flow. Kim *et al* [167] studied the motion of helical particles and suggested the possibility of separating helical particles since right- and left- handed particles have opposite drift direction. Exact analytic results for the drag coefficient of certain high-symmetry shapes such as spheres and ellipsoids can be obtained in the Stokes limit. The influence of the chirality of a macroscopic object on its transport properties were conducted for sedimentation [71] and for shear flows [45]. The latter described the vorticity drift of twisted ribbons in shear flow with direction determined by the particle chirality.

Chiral enantiomers were studied for separation in clover leaf flows [12] and in flows in channels of various geometries [168–170]. Alcanzare *et al* [171] optimized the helical shape of particles at nanoscale in terms of maximising the vorticity displacement velocity.

In these studies, fluctuating forces were taken into account in order to include the effect of thermal fluctuations on the molecules by the surrounding fluid.

For flexible particles, Watari and Larson [172] considered achiral objects with respect to their geometry in equilibrium, but with differently deformable bonds between four atoms which can be separated in shear flow. The objects consisting of four mutually interacting spheres with different equilibrium bond lengths and identical bond strengths, were demonstrated to experience a lateral drift in uniform shear flow [173]. For biological system, resistive force theory (RFT) and slender body theory (SBT) are the usual approaches used to study the propulsive motion of flagellar propulsion [99, 174–176]. These two methods can also be used to analyze flexible helix. Macros *et al* [177] recognized bacterial rheotaxis, a purely physical phenomenon, coming from the subtle interplay between velocity gradients and the helical shape of flagella.

All previous studies of chiral objects under shear, however, are restricted to rigid helixes [12, 45, 71, 166–171] and flexible tetrahedron. Most of helical polymers in reality are not perfectly rigid, particularly in biological systems. It's still unclear how the flexibility affects the deformation and dynamics of helix in shear flow. Here, we address theses issues by employing a hybrid approach in which the polymer conformations are sampled by standard molecular dynamics simulations (MD), whereas the solvent is described by multi-particle collision dynamics (MPC) [108].

4.2 Method and model

4.2.1 Method

The simulation method used here has been introduced in Sect 2.4. The solvent is described by Multi-particle Collision (MPC) simulation while the solute (helix) by Molecular Dynamics (MD). The coupling between solvent and solute is by inclusion of the monomers in the MPC collision step.

4.2.2 Model of helix

We investigate polymers with helical structure using a generic coarse-grained bead homopolymer model [173]. The equilibrium configuration of a free object, i.e. a stable configuration with bonding forces between the spheres, is assumed to be of helical form. This form is constructed by positioning the centers of the beads on a cylinder surface of radius R. Given the location of the first sphere $\boldsymbol{X}_1$, the next one, $\boldsymbol{X}_2$, is found upon rotation by an angle β around the cylinder axis combined with a translation by h_p parallel to the cylinder axis, and similarly with the third and fourth spheres yielding the respective positions $\boldsymbol{X}_3$ and $\boldsymbol{X}_4$, as illustrated by Fig 4.1. Here, the helix is set up as a left-handed helix. The positions of beads take then the form

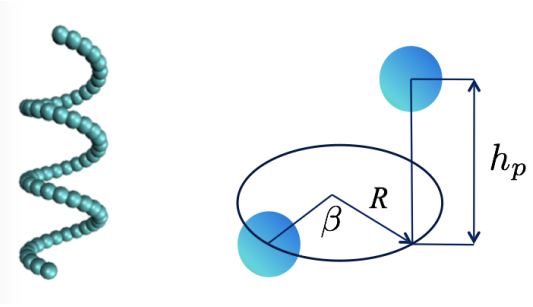

FIGURE 4.1: The configuration of a spiral object

$$\begin{aligned} x &= R\cos[(n-1)\beta)] \\ y &= h_p(n-1) \qquad\qquad n = 1, 2, \cdots N. \\ z &= R\sin[(n-1)\beta)] \end{aligned} \tag{4.1}$$

The geometry of helix can be changed by adjusting parameters h_p, β, R in Eq. (4.1) and the total number of bead conforming the helix. These parameters will determine helix input dimensions, namely the end-to-end length $2L_h$, the helix wavenumber N_p of complete helix turns, and then the derived the aspect ratio $p = 2L_h/2R$, pitch $c = 2L_h/N_p$.

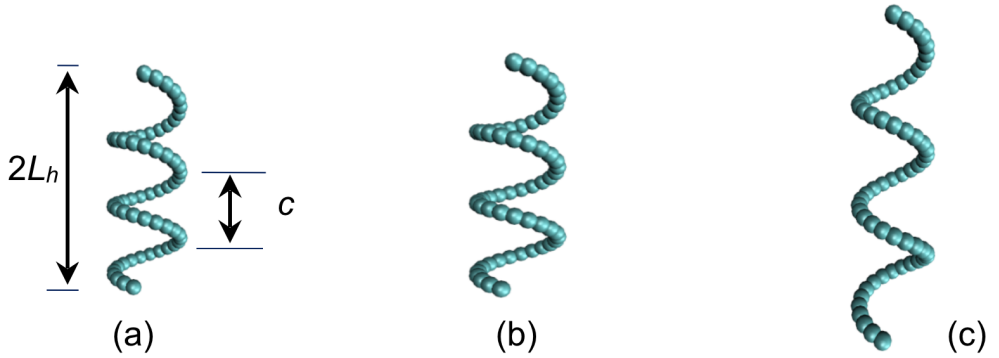

FIGURE 4.2: The geometry of helix with parameters (a) $R = 2$, $h_p = 0.25$, p_0 =1.5, c = 3. (b) $R = 3$, $h_p = 0.15$, p_0 =1.5, $c = 2$. (c) $R = 2$, $h_p = 0.3$, p_0 =4.5, $c = 5$

Once the initial location of the beads is given, molecular dynamics considers the bead connected to each other by harmonic bonds, bond bending, and torsional potentials.

The energy associated with the harmonic bonds which fix together consecutive monomers is calculated using the spring potential:

$$U_{\text{bond}} = \frac{\kappa_{\text{bond}}}{2} \sum_{i=2}^{N_m} (|\boldsymbol{X}_i - \boldsymbol{X}_{i-1}| - l_0)^2 \tag{4.2}$$

where κ_{bond} is the harmonic constant and l_0 is the equilibrium bond length. $\mathbf{X}_i$ is the position vector of bead i.

$$U_{\text{bend}} = \frac{\kappa_{\text{bend}}}{2} \sum_{i=3}^{N_m} (\cos\theta_i - \cos\theta_0)^2 \tag{4.3}$$

A bending potential is introduced to control the flexibility of the chain, where κ_{bend} is the bending force constant and θ_i is the bending angle formed by bead i, $i+1$ and $i+2$. θ_0 is the equilibrium bending angle. The bending angle follows from the relation $\cos\theta_i = \Delta\boldsymbol{X}_i \cdot \Delta\boldsymbol{X}_{i-1}/(|\Delta\boldsymbol{X}_i||\Delta\boldsymbol{X}_{i-1}|)$,

An additional potential associated with the dihedral angles to maintain the initial helical order by exerting a torsional effect on polymer bonds:

$$U_{\text{tors}} = \frac{\kappa_{\text{tors}}}{2} \sum_{i=4}^{N_m} (\cos\tau_i - \cos\tau_0)^2 \tag{4.4}$$

where κ_{tors} is the torsional force constant and τ_i is the torsional angle formed by bead i, $i+1$, $i+2$ and $i+3$. τ_0 is the equilibrium torsional angle. The torsional angle from $\cos\tau_i = (\Delta\boldsymbol{X}_i \times \Delta\boldsymbol{X}_{i-1})(\Delta\boldsymbol{X}_{i-1} \times \Delta\boldsymbol{X}_{i-2})/(|\Delta\boldsymbol{X}_i \times \Delta\boldsymbol{X}_{i-1})||\Delta\boldsymbol{X}_{i-1} \times \Delta\boldsymbol{X}_{i-2}|)$, where $\Delta\boldsymbol{X}_i = \boldsymbol{X}_i - \boldsymbol{X}_{i-1}$. Each potential can be toned independently by changing κ_{bond}, κ_{bond} or κ_{tors}.

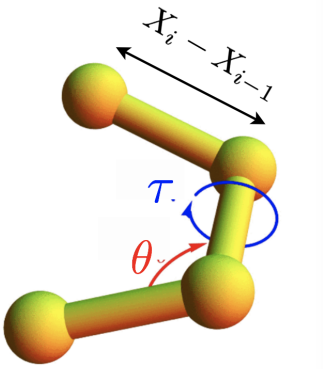

FIGURE 4.3: Sketch of a chain segment containing four monomers. The bond length is represented by $\boldsymbol{X}_i - \boldsymbol{X}_{i-1}$ and the torsion angle is by τ (blue) and the bending angle by θ (red)

Furthermore, a repulsive and truncated Lennard-Jones potential

$$U_{\mathbf{LJ}} = \begin{cases} 4\varepsilon \left[\left(\frac{\sigma}{r}\right)^{12} - \left(\frac{\sigma}{r}\right)^{6} \right] + \epsilon, & r < 2^{1/6}\sigma, \\ 0, & \text{otherwise}, \end{cases} \tag{4.5}$$

is used to account for excluded-volume interactions between non-consecutive beads that happen to be in a certain distance range. This interaction prevents, for example, flexible helix from crossing itself.

The dynamics of the beads is then described by the Newton equations of motion, which are integrated by the velocity-Verlet algorithm with time step $\Delta t_{MD} = 10^{-6}$ for the largest value of κ.

The bead particles are coupled to the fluid in the collision step with so-called MPC coupling algorithm described in sec. 2.4.2.2. Finally, Lees-Edwards boundary conditions are employed in order to impose a linear velocity profile $v_y = v_z = 0, \quad v_x = \dot{\gamma} y$ in the fluid in the absence of a polymer, with a tunable shear rate $\dot{\gamma}$. The method has been presented in sec. 2.4.2.5

4.2.3 Parameters

The size of the simulation box is taken to be $L_x = L_y = L_z$, with L_x varied from $30a^3$ to $80a^3$ to test the convergence for the simulations, a being the side length of the collision cell. The mass of a helix bead is set to $M_h = 10m$ in order to enhance the hydrodynamics coupling [117]. In this work, the default configuration which will be used unless otherwise specified is, number of beads for one-turn helix is $N_m = 20$, $h_p = 0.3$, $R = 2$, $\beta = 2\pi/N_m$, which yield the equilibrium bond length l_0 =0.694, the equilibrium bending angle $\phi_0 = 16.2°$, and the equilibrium torsional angle $\tau_0 = 172°$. Here, the helix is inextensible. So the bond force constants is fixed to rigid condition $k_{bond}/\sqrt{k_B T} = 10^7$ such that polymer contour length doesn't change with fluctuations, nor with any strength of the applied field, such that $L_h = (N_m - 1)l_0$Bending and torsional force constants are varied from 10^7 to 10^4, what covers the range of very stiff to very flexible helices.

4.3 Results and discussions

4.3.1 Rotational diffusion of helix

When the helix is of micro-scale size, thermal fluctuations are considerable and they are naturally taken into account in our simulation. In order to characterize the rotational diffusion coefficient of the helix, the mean-squared angular displacement $W(t)$ is calculated in simulation by Eq. (2.15). The results of $W(t)$ is shown in Fig. 4.4, from which we can obtain rotational diffusion coefficients of helix at different aspect ratios. The value of D_r is much smaller than theoretical one of rod-like rigid cylinder with same aspect ratio [178]. It is because compared to rod with same aspect ratio, the helix corresponds to hollow structure and has much longer contour length, which leads to smaller rotational diffusion coefficient.

4.3.2 Tumbling and Breathing of flexible helix

Many soft matter systems, ranging from rod-like colloids to linear or star polymers, droplets, and vesicles, have been studied under shear flow conditions, since this is typical case where the dynamical behavior can be investigated in a stationary nonequilibrium

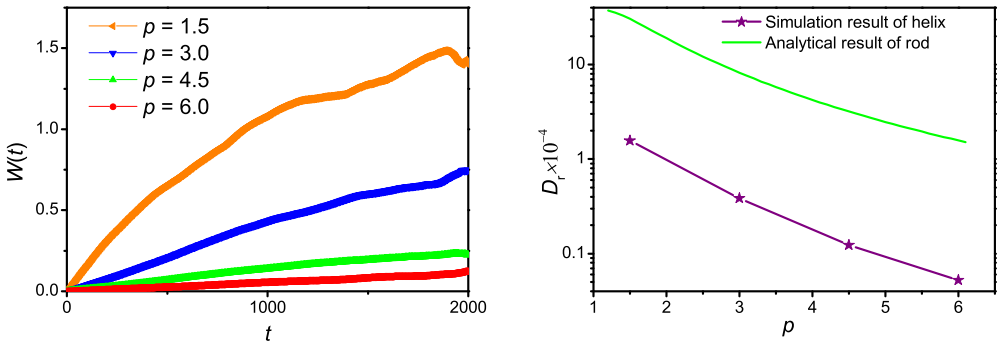

FIGURE 4.4: (a) Mean-squared angular displacement vs. time for a the helix with $R = 2a, L = 18a, N_p = 3$. (b) Rotational rotation coefficient of helix vs. Aspect ratio. Helix radius $R = 2a$, pitch $c = 6a$ and pitch numbers N_w varies from 1 to 4.

state [3, 179]. A rich dynamical behavior has been found for deformable soft objects under shear flow, such as tumbling, kayaking, tank-treading, stretching, and collapsing [180–182]. Helical polymers present a special structure, in which the torsional potentials lead to its chirality.

In order to investigate the effect of the flexibility we modify both the bending and the torsional potential strength by fixing both constants the same value. $\kappa = \kappa_{\text{bend}} = \kappa_{\text{tors}}$. In this way, the limit of vanishing κ corresponds to a flexible polymer with no helicoidal character, and the limit of $\kappa \to \infty$ corresponds to a fixed helix. Intermediate values of κ corresponds to flexible helixes, in which the end-to-end distance is not fixed , the central cylinder is not completely straight, and in which the distance between consecutive helix turns is not constant.

When the shear rate is big enough or helix is flexible enough, the helix will be subjected to larger shear stress when the main axis of helix is perpendicular to the flow direction. Then the helix will be largely stretched. The shear stress is reduced when the main axis of helix is aligned to flow direction. Figure 4.5 indicates the helix tumbles in flow due to its interaction with the applied flow field. Here, y/y_0 relates to the time dependent position in gradient direction of one of the beads at the extreme of the helix while $L/2L_h$ refers to the normalized end-to-end length. The particle is subject to strongest shear stress and stretched, such that end-to-end length of helix reaches a peak value when its main axis is perpendicular to flow direction. Then the end-to-end length of helix decreases till the main axis of helix is aligned to flow direction and increases again when the angle between the main axis of helix and flow direction becomes bigger. We refer as breathing to the stretching and collapsing of the total helix length, and as tumbling to the periodic orientation rotation of the complete helix. So in one tumbling period there are two breathing ones. During the process, the dynamics of helix shows the perfect coupling of tumbling and breathing.

4.3.2.1 Stability phase diagram

In shear flow the helix shrinks and partially folds quickly in case where the shear stresses are larger that these applied by the bending and torsional potentials, such that the helical

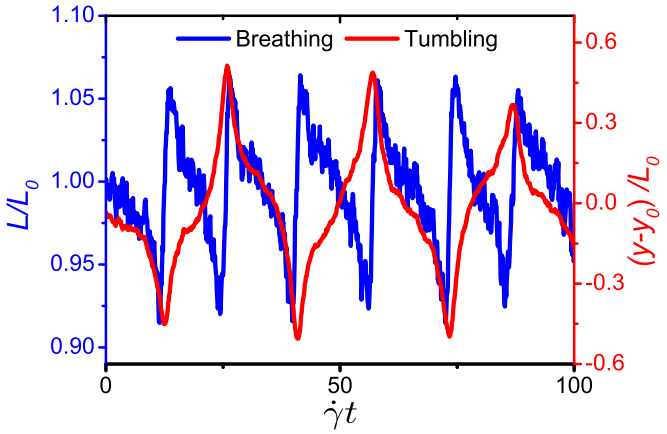

FIGURE 4.5: Temporal evolution of the normalized end-to-end length of helix L/L_0 (blue line) and the normalized y label of first bead (red line). At $t = 0$, the main axis of helix is parallel to the flow direction. The rigidity of helix $\kappa = 10^7$. The shear rate $\dot{\gamma} = 0.1$.

structure is broken. In our simulations we obtain the stability diagram gathering at the prevalence of the helical structure for one single case of the initial helix geometry as shown in Fig. 4.6. If the helix has much bigger aspect ratio and under larger shear rate, the rigid helix would be bended besides stretched and collapsed.

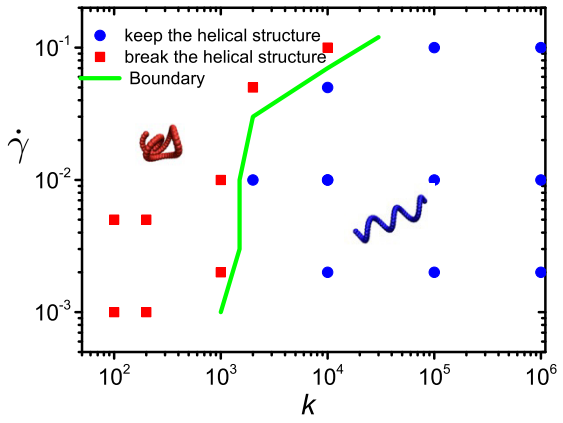

FIGURE 4.6: Diagram of helix state. $R = 2$, $N_p = 3$, $L = 18$. The red points represent the helix is in folding and chaotic due to shear stress. The blue points means the helix still can keep helical structure, and tumbling and breathing even subjects to shear flow. Green line is boundary between two states.

4.3.2.2 Breathing and tumbling

Firstly, in Fig. 4.7, the average length of helix increases with rigidity. It's interesting to note that the length of more flexible helix is still smaller than at equilibrium for all investigated cases, even though the helix is stretched during some time. This indicates that the semi-flexible helix is always compressed if the pitch is not so small to prevent the compression .

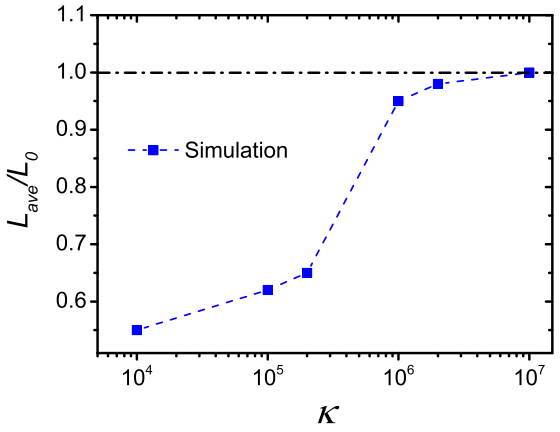

FIGURE 4.7: Average end-to-end length of helix varies with the rigidity of helix from 10^4 to 10^7. The shear rate $\dot{\gamma} = 0.1$.

In Fig 4.8, the difference between average and maximum length shows to decrease with rigidity. This is because the flexible helix can be stretched easily under same shear rate.

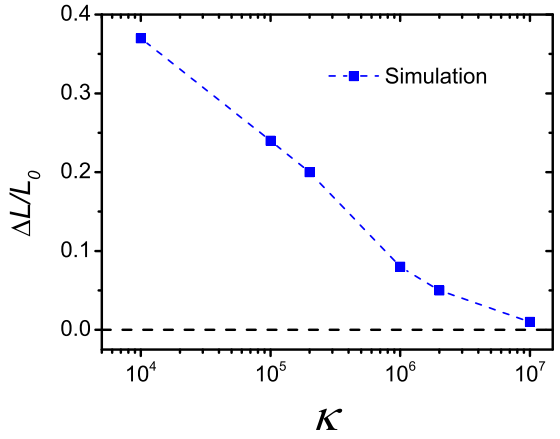

FIGURE 4.8: Changed amplitude of helix length varies with the rigidity of helix from 10^4 to 10^7. The shear rate $\dot{\gamma} = 0.1$.

In Fig. 4.9 the position (y) of the helix end along the shear-gradient axis characterizes the tumbling process since where the tumbling takes place is the flow-gradient plane. Besides the effect of thermal fluctuations, Fig 4.9 shows that the helix tumbling motion is similar to that a rod-like colloid. From Fig 4.9, the rigid helix tumbles periodically same as rigid rod. When the rigidity of helix decreases to 10^5, the periodicity of the tumbling looses some coherence but it is still clear but does not anymore occur when the rigidity is equal to 10^4. For this flexibility and this shear strength the structure of the helix is not really preserved. In this case, the helix keeps tumbling but starts to tangle and fold itself, becomes eventually chaotic.

According to Jeffery's theory in Eq. (3.3), the tumbling period of a rigid rod increases with aspect ratio of the rod. We perform two sets of simulations, one with fixed h_p (length) and changed R, and vice versa that are shown in the table 4.1 and Fig. 4.10. The green line is Jeffery's theory by Eq. 3.3 at $\dot{\gamma} = 0.1$ varying with aspect ratio of rods ($p_0 = L/2R$). The simulation results show that the two ways of changing geometries

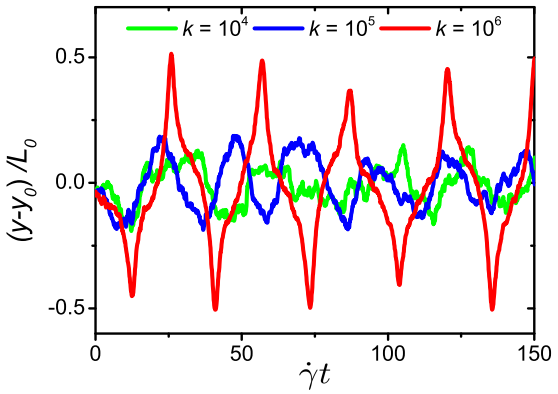

FIGURE 4.9: Temporal evolution of the normalized y label of first bead for helixes of various flexibilities (red line for $\kappa = 10^6$, blue for $\kappa = 10^5$, green for $\kappa = 10^4$). At $t = 0$, the main axis of helix is parallel to the flow direction.

overlap, which means that we don't need to know either length or radius of helix but the aspect ratio of helix for the tumbling periods.

TABLE 4.1: Different geometries of helix

h_p=0.15			
R	L_{e0}	p_0	c
2	9	2.25	3
2.5	9	1.8	3
3	9	1.5	3
4	9	1.15	3

R=2			
h_p	L_{e0}	p_0	c
0.1	6	1.5	2
0.15	9	2.25	3
0.2	12	3	4
0.3	18	4.5	6

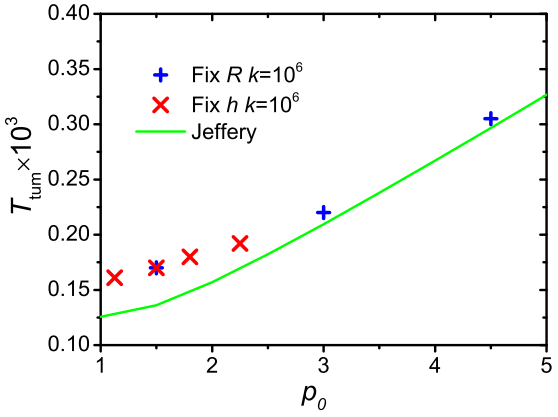

FIGURE 4.10: Tumbling period of helix as function of aspect ratio for simulations with $\dot{\gamma} = 0.1$ and $\kappa = 10^6$. Red points is from fixed length of helix, blue from fixed diameter of helix. Green line is from Eq.3.3 at $\dot{\gamma} = 0.1$. The inset is the fitting from Eq. 3.3 in terms of tumbling period.

In Fig 4.10, the green line is still Jeffery's theory with $p = p_0$. When the helix is rigid with bigger aspect ratios , the simulation results can be nicely fitted by Jeffery's theory. It's understandable since the same aspect ratios for rods and helices lead to same torque that rises same rotational speed. However, there is some displacement away from Jeffery's theory when the helix has smaller aspect ratio. This is due to that helix with smaller aspect ratio becomes more compressible under same shear, compared to the helix

with same bending and torsional potentials. Therefore, in Fig 4.10, the helices have the aspect ratios less than 1 when p_0 is close to 1. Then the helices becomes more disk-like and have bigger tumbling periods that rise the displacement from theory.

However, in Fig. 4.11, it is very interesting that the results of helix at intermidiate flexibility ($\kappa = 10^5$) can be still fitted with Jeffery's theory at an another effective hydrodynamic aspect ratio $p = 2.79$, which is clearly smaller than the initial one. But when the rigidity of helix is decreased to values smaller than $\kappa = 10^4$, then the fitting to Jeffery's theory becomes quite unclear, which indicates that the tumbling doesn't follow Jeffery's theory anymore since the helix became too flexible and chaotic. This shows that Jeffery's theory can applied in the behaviour of helix if the helix can just keep tumbling and breathing.

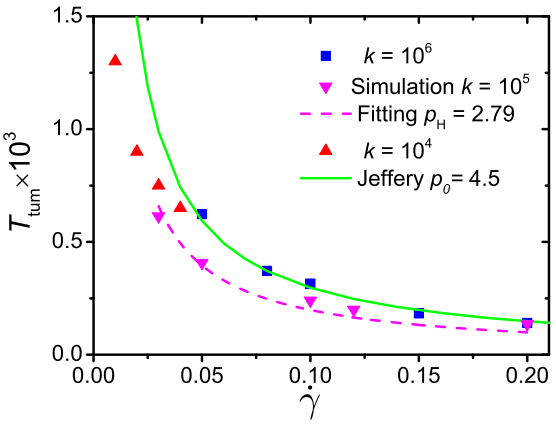

FIGURE 4.11: Tumbling period of helix varies with shear rate. Red, purple, and blue points are for rigidity $\kappa = 10^4$, 10^5, 10^6, respectively, dashed lines are fitting from Eq.3.3, Green line is from Eq..3.3 at $p_0 = 4.5$.

Figure 4.12 indicates how the effective aspect ratios are related to flexibility. For the helix with $p_0 = 4.5$, the effective p_0 increases to 4.5 with rigidity. This can be understood from Fig. 4.7, where the average length of helix increases with rigidity. This happens to another helix with $p = 7.5$ as well.

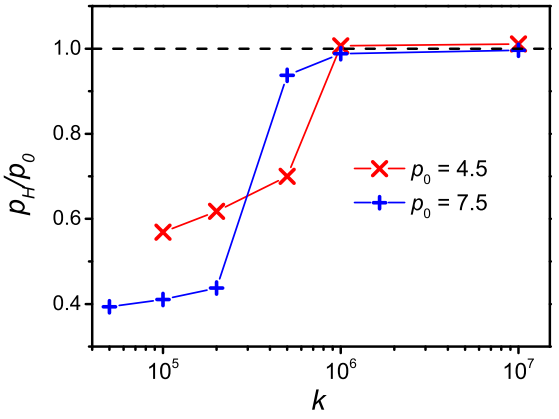

FIGURE 4.12: Effective aspect ratio as function of κ. The shear rate $\dot{\gamma} = 0.1$,

4.3.3 Vorticity displacement

4.3.3.1 The effect of HI

Besides the tumbling and breathing of helix under uniform shear, the helix drifts along the vorticity direction of flow. As explained in Ref. [45, 171, 173], the main mechanisms leading to a lateral drift of the helices, i.e. to a motion perpendicular to the flow direction and to the direction in which the flow speed changes, can be summarized as follows. The shear field of the flow leads to a rotation of the helix, which then, like a small propeller, moves in, or opposite to, the direction of the vorticity of the flow. The particles with different handedness drift in opposite directions. In order to assess the reason of lateral drift, we perform random MPC simulations, which eliminate hydrodynamic interactions.

The results are shown in Fig. 4.13. Δz, is the average displacement along the vorticity on 16 individual samples. In contrast to the result from the MPC simulation with full HI, the displacement in random MPC simulation shows to be very clear vanishing at same shear rate. This allows us to conclude that the lateral displacement is driven by hydrodynamics.

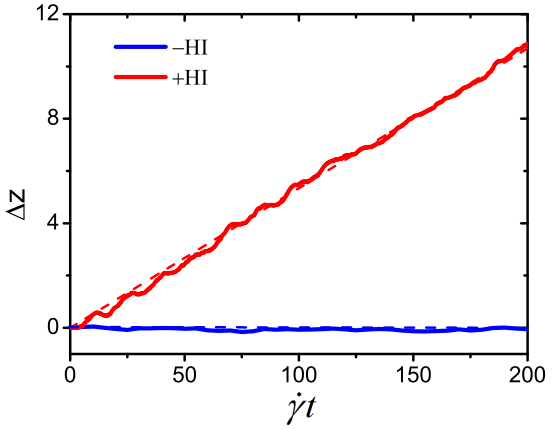

FIGURE 4.13: Temporal evolution of the displacement of helix along vorticity direction with and without HI, at $\dot{\gamma} = 0.1$ and R=2.

4.3.3.2 Dependence of shear rate

The shear flow must first orient the particles before it can induce any drift. One would expect higher shear rate leads to bigger angular velocity of helix which would is related to its drift velocity. To study this dependence on shear rate, we have varied the shear rate in terms of the dimensionless quantity called the rotational Peclet number $Pe_r = \dot{\gamma}/D_r$.

Figure 4.14 shows the mean displacement of the particles in the vorticity direction plotted against the shear strain $\dot{\gamma}t$ for various shear rates $\dot{\gamma}$. For large Pe_r, Fig. 4.14 shows that the displacement linearly increases with time. It indicates that the particles move with constant average migration velocity. For smaller Pe, Δz shows considerable fluctuation, which is a result of dominant Brownian motion along the z axis.

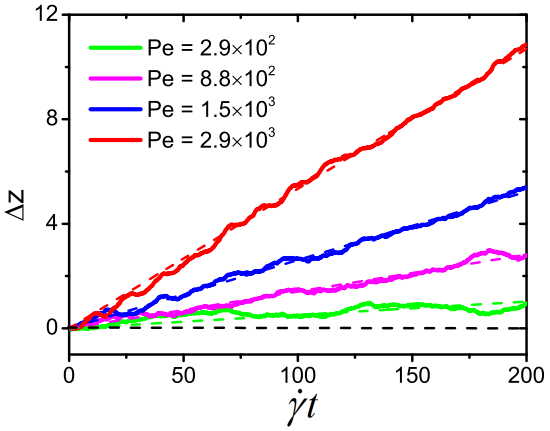

FIGURE 4.14: Temporal evolution of the displacement of helix along vorticity direction at different Pelect number from at $R = 2$

An analytical expression for the migration velocity as function of Peclet number has been obtained by Doi and Makino [11, 45] in the context of twisted ribbons:

$$v_D = \begin{cases} F R_{rb} \dot{\gamma} Pe^2 & Pe \ll 1 \\ G R_{rb} \dot{\gamma} & Pe \gg 1 \end{cases} \tag{4.6}$$

where $2R_{rb}$ is ribbon's width. F and G are constants dependent on the shape of the particle, which are identically zero for non-chiral particles, and non-zero for chiral particles. The underlying mechanism, the shear-induced drift of chiral particles in the vorticity direction, is a nonlinear effect in bulk solution, since the helix orientation is isotropic and v_D is proportional to $\dot{\gamma}^3$ at $Pe_r \ll 1$. The migration velocity is proportional to the shear rate at high Peclet number. This is a general result of the Stokesian dynamics where the effect of Brownian motion is negligible.

Our simulation results of helix in Fig 4.15 also show the migration velocity v_D depends on shear rate linearly when $Pe > 300$. The linearly fit with Eq. (4.6), the parameter C is equal to 0.278 for the parameters here employed, although in the following we see that this number depends on the helix geometry and flexibility. Due to strong thermal fluctuation, it will take timely prohibitedly to check if our results are consistent with the theory in the regime of small Pe_r, this would be at $Pe_r \ll 1$ in Eq. (4.6).

4.3.3.3 Effect of geometry

The drift velocity is not only determined by shear rate but also by the parameters characterizing the helix. In previous discussion, we already described how the tumbling period is affected by its aspect ratio in Jeffery's theory [160]. Figure 4.16.a shows that the migration velocity increases monotonically with number of pitches, and that it saturates to a constant value with for a large value of the number of pitches. The asymptotic value is a function of pitch over radius c/R only.

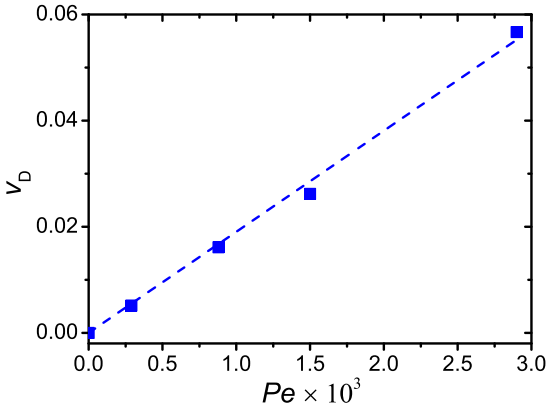

FIGURE 4.15: Drift velocity v_D as function of Peclet number from 0 to $3{\times}10^3$. Rotational diffusion coefficient of the helix $D_r = 3.3 \times 10^{-5}$.

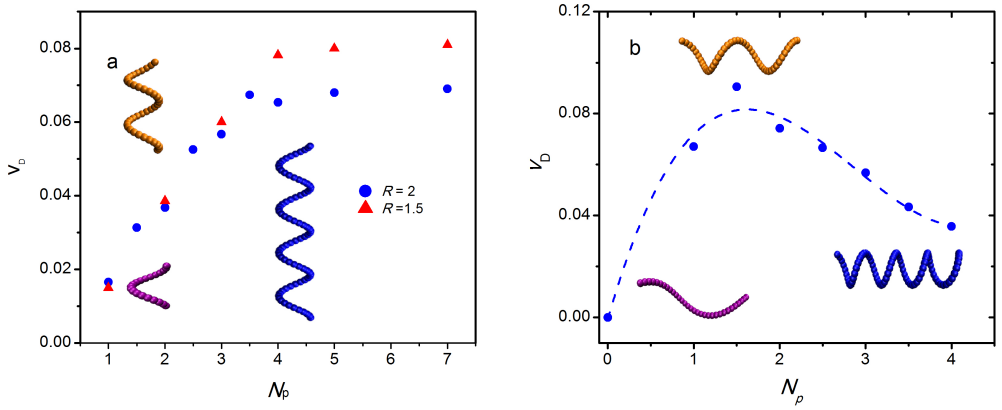

FIGURE 4.16: Drift velocity as a function of the number of helix pitches for (a) fixed radius R and pitch c. The red and blue points are for radius $R = 1.5$ and 2, respectively and pitch of helix $c = 6a$. (b) fixed end-to-end length and radius, varied pitch c.

It is also interesting to fix the aspect ratio by fixing the diameter and end-to-end length of helix but change the number of pitches. Figure 4.16.b shows that the migration velocity varies for the particle of fixed end-to-end length $2L_h = 18a$. It is seen that the migration velocity has a peak, where the pitch number $N_p = 1.5$, and the pitch length $c = 2L_h/N_p = 12a$ is approximately equal to $2\pi R$, here $R = 2a$. This result is consistent with Doi's work [45], which studied twisted ribbon in shear flow by simulation and theory. One can understand the behavior qualitatively as the crossover between two well-defined limits. There are the limit of pitch $c \to \infty$ (corresponds to rod limit) and the limit of $c = 0$ (corresponds to tube limit). In both limits, the particle loses chirality, and the migration velocity should vanish, such that a maxima can be expected in between.

The same phenomenon can be observed when the number of pitches and end-to-end length of helix are fixed but the radius is changed. There is also a maximum in Fig. 4.17, where, however, the pitch length $c = 6a$ is approximately equal to πR . And the two limits are: the radius of helix $R = 0$ (the rod limit) and the radius $R \to \infty$ (the ring limit).

Then the contour length and number of pitches are fixed but the diameter is changed.

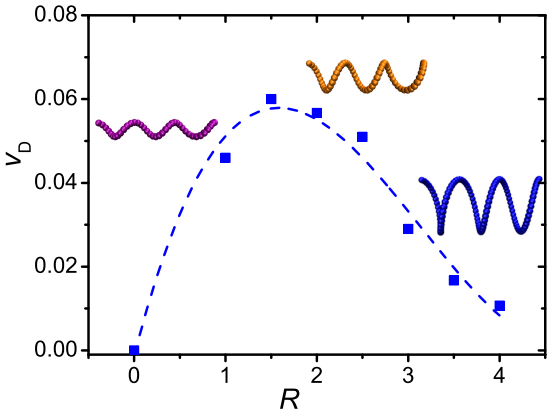

FIGURE 4.17: Drift velocity varies with radius of helix. The end-to-end length and the number of pitches are fixed

Fig. 4.18 shows that there are still peaks, where the pitch length $c = 10a$ is approximately equal to $2\pi R$ ($R = 1.5a$). There are two limits, one of which is the radius R vanishes (the rod limit), and another is that the gap between consecutive pitches vanishes. The peaks appear at $c = 2\pi R$ regardless of shear rate and number of pitches in Fig. 4.18. This would help us understand how to optimize the helix geometry in terms of drift velocity.

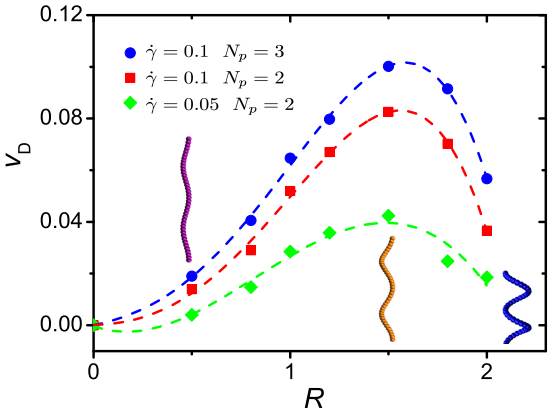

FIGURE 4.18: Drift velocity as function of the radius of helix . The contour length and the number of pitches are fixed. The blue points: the number of pitches $N_p = 3$, shear rate $\dot{\gamma} = 0.1$. The red points: $N_p = 2$, $\dot{\gamma} = 0.1$. The green points: $N_p = 2$, $\dot{\gamma} = 0.05$. At the peaks: the pitch $c = 10a$ and the radius $R = 1.5a$.

4.3.3.4 Effect of flexibility

For flexible helixes, pitches keep being changed when the helix is in shear flow, see Fig. 4.7. The average pitch length of flexible helix is always smaller than the one of more rigid helixes. Meanwhile, the average diameter of flexible helices is bigger than the one of more rigid ones.

Therefore, the migration velocity would decrease with flexibility if the equilibrium pitch of helix $c \leq 2\pi R$ (located in the right of peaks in Fig. 4.19). In Fig. 4.19, the equilibrium

pitch of helix $c = 6a$, definitely smaller than $2\pi R$. The migration velocity is increased with rigidity, then reaches an asymptotic value due to rigid condition since the end-to-end length keeps asymptotic.

From a different perspective, it can be understood that the drift velocity is a property of the intrinsic chirality of the helix, which is dependent on helix geometry when the helix is rigid. Furthermore, the chirality is relevant to the helix rigidity as well. It is clear that the behaviour of a flexible helix should be close to the one of flexible rod. This is why in Fig. 4.19 the drift velocity increases with rigidity. The helix still have lateral drifts when the helix is very flexible at $\kappa = 10^3$ to 10^4 and becomes chaotic under shear rate $\dot{\gamma} = 0.1$.

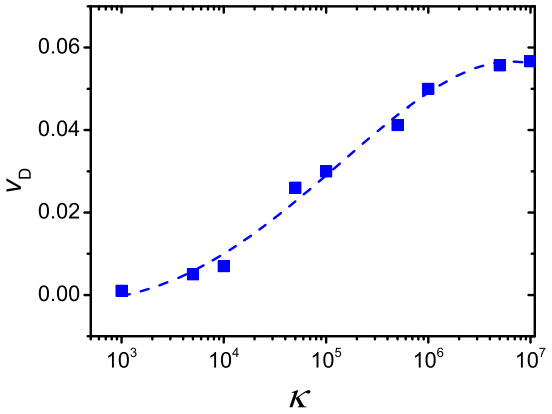

FIGURE 4.19: Drift velocity varies with the flexibility of helix from $\kappa = 10^3$ to 10^7 under shear rate $\dot{\gamma} = 0.1$. Parameters of helix: $R = 2a$, $c = 6a$.

4.4 Summary

We have studied the behavior of a helix-like colloid in shear flow. For a helix with a strong rigidity the shape is well preserved in the flow and the motion can be well understood with the Jeffery theory [160] for rod-like colloids. The rigid helix keeps tumbling or kayaking subject to shear stress. If the helix is not completely rigid, it tumbles and breaths in shear flow until a critical shear rate is reached. This means that eventual small deformations do not really affect the overall motion. The flexible helix transits to chaotic motion once the rigidity of helix can't support it's helical structure and behaves just as a flexible polymer .

We demonstrated that the lateral drift of chiral particles in uniform shear flow is driven by hydrodynamics. The drift velocity increases linearly with shear rate because of the Stokesian dynamics. Not only the strength of the applied shear determines the value of the vorticity velocity, but also the helix geometry. For rigid helix, the drift velocity shows a maxima between rod and tube limits when its radius or end-to-end length is changed and other parameters of helix geometry are fixed. When we fix the contour length of the helix and change the pitch, there is still a maximum value of drift velocity.

The above results also help us understand how the migration velocity is influenced by the helix rigidity. The end-to-end length of flexible helix is shorter but the radius is larger compared to more rigid ones in shear flow. This smaller effective aspect ratio implies that more flexible helix has smaller tumbling frequency and also smaller migration velocity in same shear flow.

Vorticity displacement of the helix in the presence of shear flow is an interesting characteristic both in fundamental research or industry applications. These results can be helpful to design and to optimize artificial helix or flagella in terms of lateral drift velocity, which can be used in medicine delivery or transport in biological systems.

This work doesn't investigate chaotic state of helix in shear flow in detail, which can indicate the dynamics and elastic properties of helix under critical shear stress. Thie work also can be extended to the helix with higher aspect ratios which can be bended by shear stress.

h

Chapter 5

Swimming of a deformable helix

5.1 Motivation

Cell motility is a major achievement of biological evolution and is essential for a wide spectrum of cellular activities. The net movement of micro-swimmers critically depends on the anisotropy of the viscous drag within the fluid [13], and requires a non-reciprocal swimming stroke to break the time-reversal symmetry of the underlying equations of motion as theoretically proven by Purcell and the so called scallop theorem [14]. The motion of model cellular swimmers, such as spermatozoa, bacteria, and algae, has been studied characterizing how they swim in bulk fluids [15, 16], in search for food sources [17], and moving near boundaries [183, 184]. The motion of some of these micro-swimmers is produced classically by the rotation of rigid helical structure although the deformation of a helix has also shown to produce motion [185, 186]. The helical flagellar filaments of *Escherichia coli* (*E.coli*), for example, can switch form producing them a rotation and propulsion in a different direction [187], leading to random reorientations of the bacteria as a whole what characterized the so-called run-and-tumble motion. For the bacterium *Rhodobacter sphaeroides*, these reorientation events were previously thought to be governed by Brownian rotation, but recent results suggest that the polymorphic change itself actively rotates the swimmer [188]. A different phylum of bacteria, the *Spirochaetes*, can also use the deformation of helical shape to generate propulsion. These bacteria encase their flagellar filaments within a thin sheath around their bodies [189]. When the helical filaments are rotated, their motion deforms the cell body through a set of waves and helical shapes, which in turn creates motion [190]. Similarly *Spiroplasma*, a group of small helical unflagellated bacteria, are able to generate thrust by propagating a switch in helix handedness along its body length [191].

These systems have also inspired the creation of artificial microswimmers with helical tail. One example is a flexible flagellum-like tail of magnetic particles bridged by DNA molecules and end-linked to a red blood cell as a head. The structure could be actuated and directed by an oscillating external magnetic field [84]. The second example is a biohybrid swimmer that consists of a polydimethylsiloxane filament on which cardiomyocytes have been adhered. The cardiomyocytes contract periodically and deform the

filament to propel the swimmer [192]. Recently Mourran *et al.* developed a deforming helical microswimmer made by a temperature sensitive gel [86, 193]. When periodically heated and cooled with a laser, these gels expand and contract such that they retain their helical shape while changing their helix radius and axial length in a controlled manner. When the deformations are non-reciprocal, they have shown to lead to a net rotation parallel and perpendicular to the helix axes (as illustrated in Fig. 5.1). Later, Koens *et al* [89]., explored the net translation and rotation of general unbounded perfect deforming helices by resistive force theories, which reveal that the rotational displacements are optimised at small axial lengths while translational displacements are optimised at large axial lengths.

Motivated by these recent experimental and theoretical results and by the importance of deforming helices in biological systems, this chapter explores how a deforming helix can generate motion by a hybrid simulation method. The theoretical results [89] neglected the effect of thermal fluctuations, which is not very accurate considering that the experimental helixes are on the order of 10 μm where the stochastic interactions with the solvent are still relevant. First we consider the motion generated by a perfect, inextensible deforming helix in an unbounded fluid. We demonstrate that this simple shape can rotate by generating a non-reciprocal swimming stroke in bulk conditions. Then the effect of confining walls is taken account, and we can characterize how the rotation speed and helix position are affected with respect to walls.

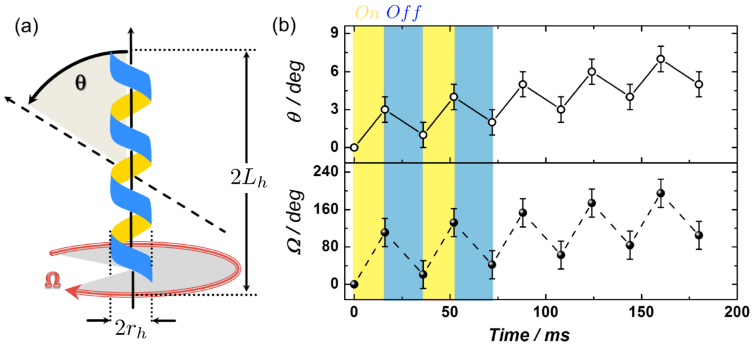

FIGURE 5.1: Net rotating motion of a deforming gel helix [86]; (a) Schematic diagram of the helix of length $2L_h$ (measured along the helix axis) and diameter $2r_h$, with a definition of the two angles (θ, Ω) by which it may rotate; (b) Angular displacements of the helix as it periodically deforms in a non-reciprocal manner. Light yellow regions indicate when the light is on, while dark blue regions reflect when the light is off. Figure adapted from Ref. [86]

5.2 Method and model

We employ a hybrid simulation method similar to that in Chapter. 4. The helix is simulated by molecular simulation as described in Sect. 4.2.3, while solvent is dealt by MPC described in Sect. 2.4.2. The coupling between helix and solvent is done with MPC as explained in Sect. 2.4.2.2.

In order to include the actuated deformable character of the helix we employ a generic coarse-grained bead-spring model for elastic, self-interacting gels with torsional interaction. The gel is represented by a linear chain of N monomers. A perfectly deforming helix is expected to maintain a helical shape throughout its entire motion. Hence its centreline or the positions of beads, $\mathbf{X}(s,t)$, can always be written as

$$\mathbf{X}(s,t) = \{\alpha_h(t)s, R(t)\cos[(k(t)s], R(t)\sin[(k(t)s]\} \tag{5.1}$$

where t is time, $\alpha_h(t)$ is the cosine of the helix angle, $R(t)$ is the helix radius, $k(t)$ is the wavenumber, $s \in [-l, l]$ is the arc length and $2l$ is the contour length of the helix along its centreline in Fig 5.2. In this configuration, the length along the helix axis is given by $2L_h(t) = 2\alpha(t)_h l$. Provided that this helix is inextensible, the configuration follows the additional mathematical constraint

$$\alpha_h(t)^2 + R(t)^2 k(t)^2 = 1 \tag{5.2}$$

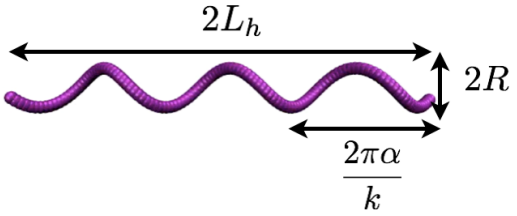

FIGURE 5.2: Sketch of helix configuration. $\alpha_h = L_h/l$. The contour length of the helix centreline is $2l$. The helix becomes a tube for $\alpha_h = 0$, and a rod at $\alpha_h = 1$.

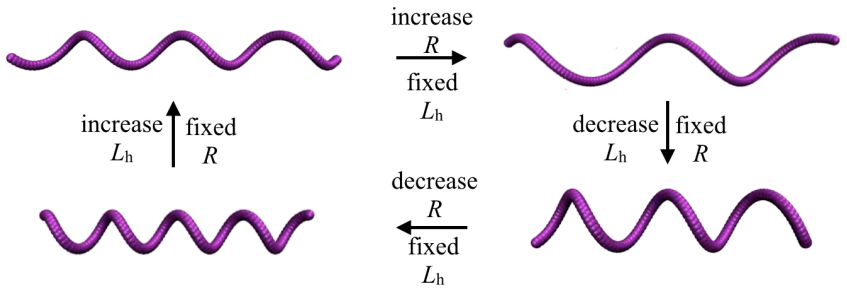

FIGURE 5.3: Illustration of a perfect helix undergoing non-reciprocal deformation with centreline described by Eq. 5.1 and a circular cross-section.

at all times. In what follows, we scale all lengths in the problem by half the contour length l. The centreline condition Eq. 5.1, and inextensibility constraint, Eq. 5.2, show that a helix is uniquely defined by two of the three conformation parameters: α_h, R, and k. A deforming helix therefore has two independent degrees of freedom which can be varied sequentially or simultaneously. As discussed by Purcell in his seminal article on locomotion at low Reynolds numbers [14], two independent degrees of freedom are sufficient to create a non-reciprocal stroke (by a non-identical deformation under a time-reversal symmetry) and thus are the minimal requirement needed to induce net motion. An example of a non-reciprocal stroke, generated by a deforming helix, is shown in Fig.

5.3. This stroke was obtained by alternatively varying the axial length, $L_h = \alpha_h(t)l$, and helix radius, R, while keeping the other parameters fixed.

To stabilize the helix in the simulation, the interaction among the monomers are bond, bending and torsional potentials, similar to those in chapter. 4. In order to calculate these potentials and forces, the distance of two monomers $(X_i - X_{i-1})$, bending angle θ, and torsional angle τ can be obtained when the configuration of helix is determined as.

$$\begin{pmatrix} \alpha_h(t) \\ R(t) \\ k(t) \end{pmatrix} \Rightarrow \begin{pmatrix} (X_i - X_{i-1})(t) \\ \theta(t) \\ \tau(t) \end{pmatrix} \tag{5.3}$$

Here, the configuration of the helix is changed periodically. However the change of distance between monomers $((X_i - X_{i-1})(t))$ is restricted within 0.5% by setting high harmonic potential ($\kappa_{bond} = 10^7$) since the helix is assumed to be inextensibe.

Since the helix deforms periodically, an approximate deformation loop of the gel helix can be parametrised as

$$\begin{aligned} \alpha_h(t)) &= \bar{\alpha}_h + \Delta\alpha_h \sin(2\pi f t) \\ R(t) &= \bar{R} + \Delta R \cos(2\pi f t + \phi) \end{aligned} \tag{5.4}$$

where ϕ is the phase between the two oscillations and k is given by Eq. 5.2. The frequency of deformation is $2\pi f$, and $T_h = 1/f$ is the period of deformation. Note that for $\phi = (\pi/2,\, 3\pi/2)$. Eq. (5.4) describes reciprocal deformations while for $\phi = (0,\, \pi)$ the deformations will be non-reciprocal, which will determine the existence, and direction of an eventual net rotation.

5.3 Results and discussions

5.3.1 Rotation in bulk

The net rotation of the actuated helical swimmer is governed by its interaction with the surrounding viscous fluid as determined by the hydrodynamic interaction. The details of these hydrodynamic interactions dictate how the forces and torques on the body relate to its velocity and shape. The transient angles of helix in space can be characterized by (θ, φ) of main axis of helix in the coordinate system of Fig. 5.4. They can be calculated from the eigenvalues (x, y, z) of the gyration tensor of helices as

$$\begin{aligned} \theta &= \arccos \frac{z}{\sqrt{x^2 + y^2 + z^2}} \\ \varphi &= \arctan \frac{y}{x} \end{aligned} \tag{5.5}$$

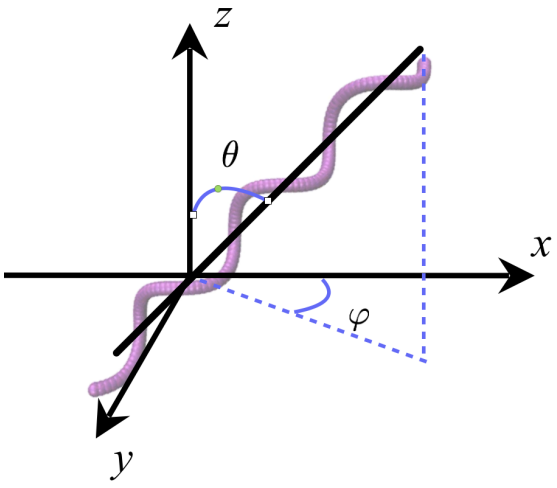

FIGURE 5.4: Schematic of rotational angles (polar θ, azimuth φ) that can be obtained from its cartesian coordinates (x, y, z). The initial postion of helix: the main axis of helix is parallel to $x - y$ plane.

From Fig.5.5, we can observe the angular displacement increases with the number of actuated period in θ direction, but the displacement is miuch less clear in φ due to insufficient statistics. To clarify this, average over multiple realizations could be necessary.

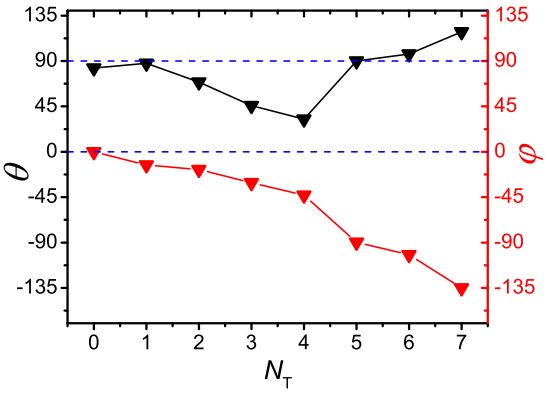

FIGURE 5.5: Angular displacement vary with periods. The parameters of deformation loop in Eq. 5.4 are: $\bar{R} = 0.06$, $\Delta R = 0.4$ and $\bar{\alpha}_h = 0.6$, $\Delta\alpha_h = 0.15$. Deformation period $T_p/T_H = 4$. Phase $\phi = 0$.

The direction of the rotation is determined by the system parameters, and it can be changed by the value of the phase between the two oscillations, as analyzed by Koens *et al* [89]. in Fig. 5.6. For the loops considered, each displacement shows a different non-sinusoidal dependence on the phase lag, φ.

In Fig. 5.6, the direction of rotation predicted at $\phi = 0$ is opposite to that at $\phi = \pi$. Our simulation results in Fig. 5.7 showed a qualitatively agreement with the theoretical one in Fig. 5.6. The helices in simulation have opposite rotation direction in Fig 5.5 and Fig 5.7. However, the amplitude of net displacement are similar at $\phi = 0$ and $\phi = \pi$.

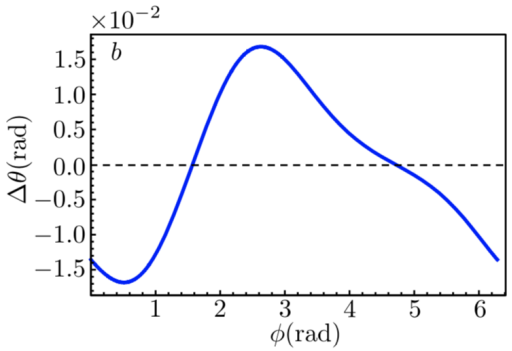

FIGURE 5.6: Net rotational displacement generated from a small-radius helix deforming according to Eq. 5.4, as a function of the phase, ϕ. For this deformation loop, the parameter values are $\bar{R} \approx 0.077$, $\Delta R = 0.026$, $\bar{\alpha}_h \approx 0.903$, and $\Delta\alpha_h = 0.047$ to reflect the typical dimensions of the experimental gel swimmer in Ref. [86]. Figure adapted from [89]

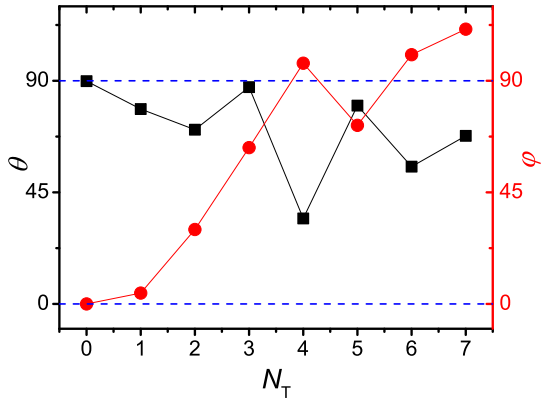

FIGURE 5.7: Angular displacement varies with periods. The parameters of deformation loop in Eq. 5.4 are: $\bar{R} = 0.06$, $\Delta R = 0.4$ and $\bar{\alpha}_h = 0.6$, $\Delta\alpha_h = 0.15$. Deformation period $T_p/T_H = 4$. Phase $\phi = \pi$.

5.3.1.1 Effect of deformation velocity

In order to ensure the presence of hydrodynamic interactions in the system it is important to consider the time T_H which we define as the time that a hydrodynamic perturbation takes to propagate a distance equal to the polymer end-to-end distance. This time is related to the solvent viscosity μ by

$$T_H = (2L_h)^2/\mu \tag{5.6}$$

In this way when considering times much smaller than T_H, the effect of HI is not guaranteed to be fully developed. In experiments, this time scale is typically orders of magnitude smaller than the relevant motion (10 ms), while in simulations this separation is not so clear becoming then an important control parameter, to verify the applicability of the method.

Therefore, in order to capture the hydrodynamics interaction in our simulation, we estimate long enough deformation period, which means at least comparable with T_H. Here, the end-to-end length of helix is approximately equal to 35, and the minimal hydrodynamics time T_H in Eq. (5.6) is 2000 for the employed MPC parameters. Different periods are tested to probe the period effect on the net rotation. From Fig. 5.8, the rotation mostly disappears when the period of deformation is half, or identical to T_H. The angular displacements become more obvious from the period equal to $T_p/T_H = 2$. And the rotational angle is bigger at $T_p/T_H = 4$ than $T_p/T_H = 2$. Therefore, the longer deformation period leads to a larger net angular displacement. Thus, in this system, bigger periods should be chosen in order to guarantee the enough hydrodynamics interaction. In the flowing, $T_p/T_H = 4$ is used. Although it has to be considered that imply also long simulation times making the results are computationally costy.

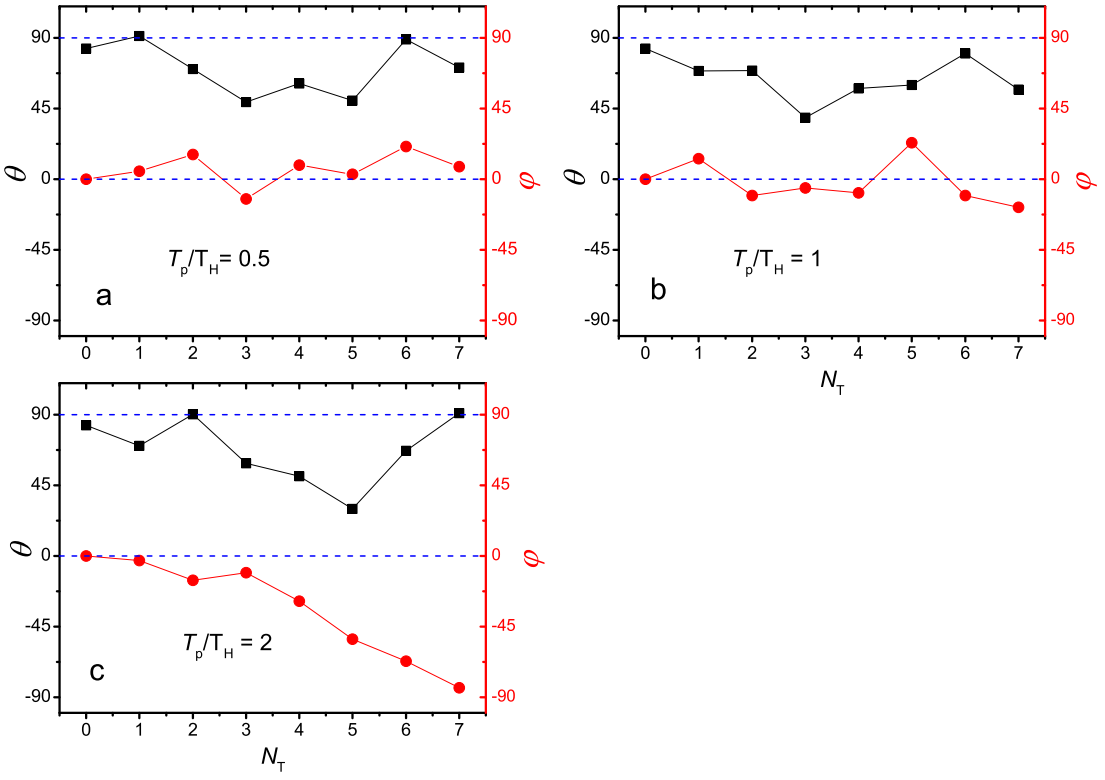

FIGURE 5.8: The time dependence of angular displacement (θ, φ) with N_T the number of completed periods for different values of the period time T_p as compared with T_H: Employed parameters in Eq: 5.4 are $\bar{R} = 0.06$, $\Delta R = 0.4$ and $\bar{\alpha}_h = 0.6$, $\Delta\alpha_h = 0.15$.

The net rotational displacements in both of θ and φ direction are averaged over 7 deformation periods and displayed in Fig. 5.9. The deformation periods exhibit less impact on $\Delta\theta$, while the net angular displacement $\Delta\varphi$ increases with increasing periods time. Here, it should be noted that the net displacement will not be increased once the deformation period covers the full of hydrodynamic interaction, where a constant value is expected to be independent of T_p.

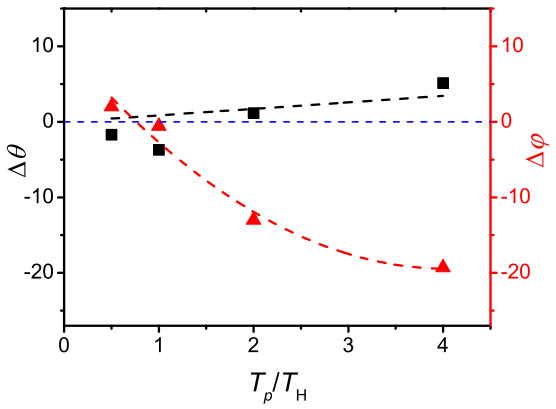

FIGURE 5.9: Average net angular displacement vs. deformation period. The net angular displacements are averaged over seven periods in Fig. 5.8 and Fig. 5.5

5.3.1.2 Effect of fluid viscosity

It was discovered a few decades ago that many micro-organisms swim faster in more viscous fluids than in less viscous ones. Shoesmith [194], reported already in 1960 the increased motility of *Pseudomonas viscosa*, *Bacillus brevis* and *Escherichia coli* for a small increase in the viscosity of the solution; larger increases led to a motility decrease. Similarly, Schneider and Doetsch [195] reported that many flagellated bacteria showed an increase in the velocity when the solution viscosity rose to a characteristic value, and a decrease thereafter. Many other studies [196–198] have corroborated this phenomenon of the swimming being enhanced with an increase in the fluid viscosity. Pande *et al.* [199] calculated analytically the velocity of a bead-spring microswimmer driven by sinusoidal forces. They have shown that the swimmer exhibits both the conventional and the aberrant kinds of behavior (defined as a decrease and an increase, respectively, of the swimming velocity with the fluid viscosity) for expected ranges of the time scale ratio.

In order to understand this effect we perform simulations with different solvent viscosities, which are obtained by varying the MPC parameters h, α and ρ. Here, we employ four values of fluid kinetic viscosity μ ranging from 0.62 to 1.67 as shown in Table 5.1. The result at $\mu = 0.87$ has shown in 5.9.d and others in Fig 5.10. The deforming helix rotates in the solvents with all investigated viscosities in θ direction as indicated in Fig. 5.10. The net angular displacements of single period are averaged them over seven deformation periods and show to vary with viscosity. In Fig. 5.11, the net angular displacements in θ direction shows to be small and with a non-monotonous dependence with μ, which is most probably due to the lack of statistical precision. The dependency of $\Delta\theta$ on fluid viscosity is not so clear, but seems keep oscillating around 0. Nevertheless, the net rotational displacements in φ direction tend to increase with fluid viscosity. Especially, the increase of $\Delta\varphi$ with viscosity is much sharper from $\mu = 0.62$ to 0.87 compared to $\mu = 0.87$ to $\mu = 1.67$, where the increase seems to reach an asymptotic value or transition to decrease if the fluid viscosity keeps growing. These results are partially consistent with ones in [199], which found that the velocity of swimmer exhibits decrease with fluid vicosity until a critical value then incrcrease with fluid viscosity.

TABLE 5.1: Solvent kinetic viscosity μ varied by MPC parameters collision time step h and stochastic rotation angle α.

h	α	μ	$\Delta\theta$	$\Delta\varphi$
0.1	100	0.62	-6.6	-4.4
0.1	130	0.87	-19	1.4
0.08	150	1.22	-22	-12.6
0.05	130	1.67	-28	-8.6

In order to understand this effect we have to consider that the typical hydrodynamic time T_H in Eq.(5.6) varies with viscosity. This is the time that a hydrodynamic perturbation needs to connect the two ends of the helix is shorter the larger the viscosity, and it seems that this times is setting the rotation frequency. Then the helix can have larger net rotational displacement when it swims in more viscous fluid during same period. Extension of this work to investigate more viscous conditions will show the rotation velocity of helix would eventually decreases with fluid viscosity.

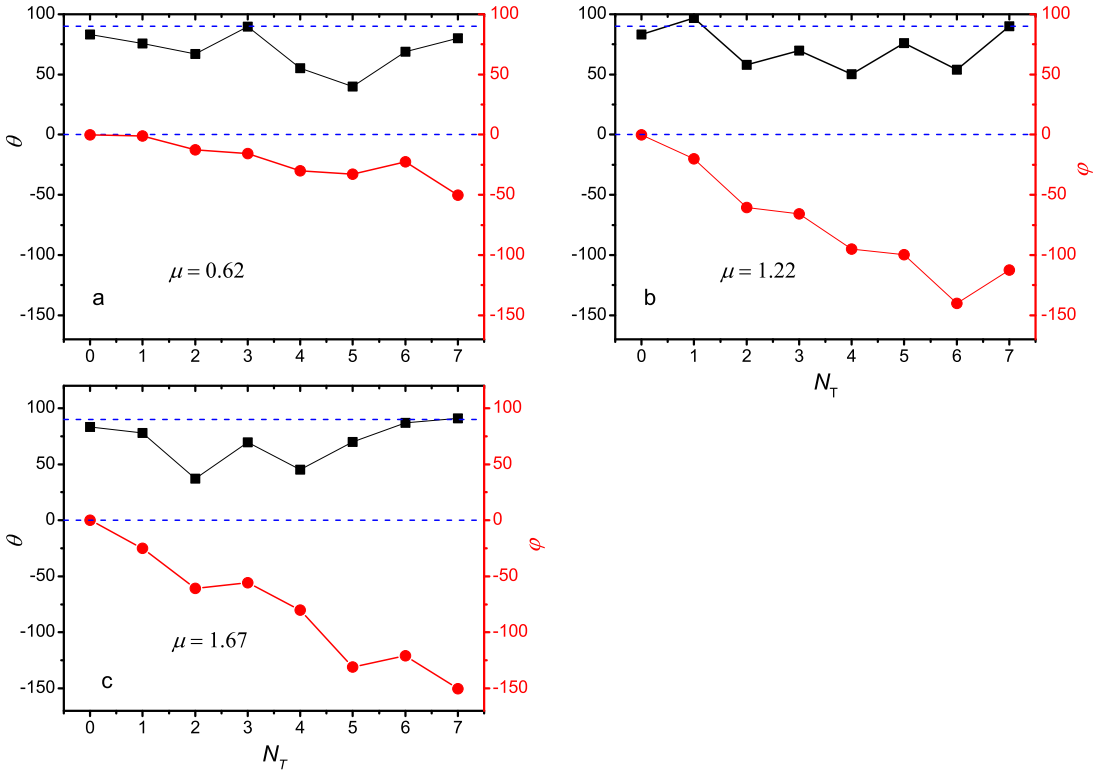

FIGURE 5.10: Time dependence of the angular displacement with N_T the number of completed periods. Employed parameters in Eq: 5.4 are $\bar{R} = 0.06$, $\Delta R = 0.4$ and $\bar{\alpha}_h = 0.6$, $\Delta\alpha_h = 0.15$.

5.3.1.3 Effect of helix configuration

It is now important to investigate the relation between parameters of the imposed deformation and the net resulting rotation. Koens *et al.* [89] investigate this system and define a vector field by balancing the torques of the helix, which are only related to the

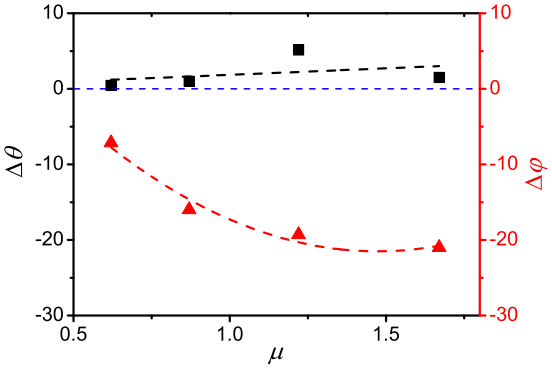

FIGURE 5.11: Average net angular displacement $(\Delta\theta, \Delta\varphi)$ varied with fluid vicosity μ. The net angular displacements are averaged over seven periods in Fig. 5.10 and Fig. 5.5

helix deformation parameters α, R, k. The strength of this field $\mathbf{M}^{\theta} = (M^{\theta,r}_{r,\alpha_h}, M^{\theta,\alpha_h}_{r,\alpha_h}, 0)$ is shown as a function of two deformation parameters as a colormap in Fig. 5.12. Any closed loop in this vector field would correspond to a possible deformation cycle, and the integral of $\mathbf{M}^{\theta}$ over the area V in the closed loop in Fig. 5.12 determines the value of the net rotation as

$$\Delta\theta = \int\int_{V} (\nabla \times \mathbf{M}^{\theta}) \cdot \hat{\mathbf{x}} dR d\alpha_h \tag{5.7}$$

where V is the area within the loop in configuration space and $\hat{\mathbf{x}}$ is the unit vector perpendicular to the configuration space. Inspection of the map in Fig. 5.12 revealed the general trends of the swimmer, and clearly showed the large density of iso-contour lines in Fig. 5.12 at small helix radius. The argument indicates $(\nabla \times \mathbf{M}^{\theta}) \cdot \hat{\mathbf{x}}$ strongly oscillates between positive and negative values of almost equal magnitude but increasing frequency when changing the radius,. This increasing rate of oscillation suggests that it is better for the swimmer to have a larger helix radius than larger loops which do not cross a zero contour are possible, thereby reducing the sensitivity of the results to small changes while maximising the area within the loop.

In Ref. [86], the mean (scaled) helix radius of the reported gel swimmers deformation is $\bar{R} \approx 0.077$ and it varies by $\Delta R = 0.026$ throughout one cycle. Similarly the mean scaled axial length is $\bar{\alpha}_h \approx 0.903$, and it variea by $\Delta\alpha_h = 0.047$. This loop is shown in Fig. 5.12 as a solid red circle. At these parameters, the experimental [86] and theoretical [89] results show that a net rotation displacement exists even though it is quite small (around 1 degree per period). However, our simulation results for these parameters shown in Fig. 5.13 are not able to capture this and it seems that the variations in the orientation do not constitute any net rotation, but only a statistical variation around a constant value. This occurs because of the employed parameters, where thermal fluctuation is more significant than hydrodynamics interactions, which in principle could be obtained by averaging overvarious realizations.

In order to find parameters in which the net rotation is enhanced, and to understand the effect of shape on rotation, we chose another deformation loop in Fig. 5.12 (shown

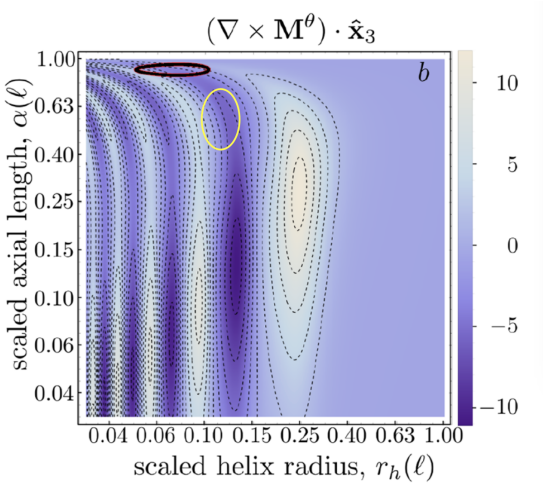

FIGURE 5.12: Motility map: Density plots of the rotation functional $(\nabla \times \mathbf{M}^{\theta}) \cdot \hat{\mathbf{x}}$ as a function of the scaled helix radius, r_h, and scaled axial length, α_h. The dashed lines represent iso-contours of the functional. The solid red loop represents an approximate path in configuration space taken by the deforming gel swimmer from Ref. [86] (Eq. 5.4 when $\varphi = 0$). The yellow loop is employed in this work. The functions have been scaled such that the total displacement over a loop is the integral of the function within the loop. Lengths scaled with respect to l. Figure adapted from Ref. [89]

with yellow circle), where $\bar{R} = 0.06$, $\Delta R = 0.4$ and $\bar{\alpha}_h = 0.6$, $\Delta\alpha_h = 0.15$. This loop has much larger area and within negative value, such that a large net displacement is expected from Eq. (5.7). The simulation results have been shown in Fig. 5.8.d, where the helix has shown angular displacements up to 20 degrees per periods ,which is very large also in comparison with experimental parameters [86].

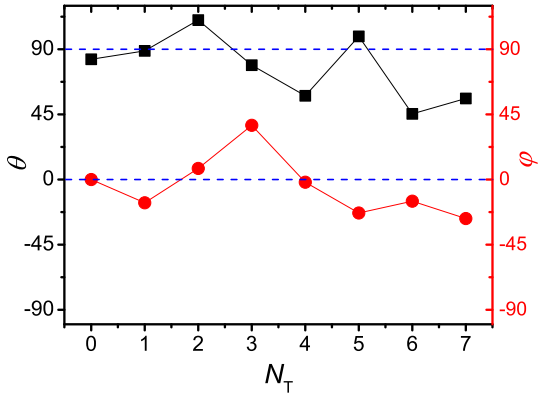

FIGURE 5.13: Time dependence of the angular displacement with N_T the number of completed periods. Parameters here same as experiments in Ref. [86]: $\Delta R = 0.026$ $\bar{\alpha}_h \approx 0.903$, and $\Delta\alpha_h = 0.047$. The deformation period $T_p/T_H = 4$

5.3.2 Motion under confinement

Many biological microswimmers regularly encounter surfaces and confinement, from sperm cells in the reproductive tract to microorganisms in the soil [200]. Moreover, microorganisms often rely on the presence of surfaces for their function and survival; for

example, bacteria form biofilms on surfaces for spreading, to enhance cell-cell exchange and nutrient uptake. And regarding synthetic microswimmers, equally important is that modern microfluidic devices can be used to investigate, control, and manipulate microswimmers in many diverse manners[201]. Therefore, in order to make predictions, and to interpret, and to understand experimental results, it is thus important to account for the effect of confinement.

5.3.2.1 Helix rotation

Using a boundary element method, Zhu *et al.* [202] already showed that spherical squirmers with tangential deformations decrease their swimming velocity with increasing confinement, while swimmers with normal deformations swim faster in confinement. Ledesma *et al.* [203] found that reduced model swimmers always move towards the center of rigid tube and show to move faster in parallel confinement. While most other swimmers show naturally accumulate at the walls.

We perform simulations in which the helix is confined between two parallel walls separated by a distance L_w in Fig. 5.14, and with periodic boundary conditions in other two directions. In Fig. 5.15, the rotational displacements in (θ, φ) are shown for two of the confinement values ($L_w/2L_h = 2$ and $L_w/2L_h = 1$). It seems that the walls enhance the rotation of the helix, this is narrower slit leads to a faster rotation. In order to quantify this effect, we define the net rotational displacement velocity in φ direction in bulk is ω_b, and ω_c for the confinement. Employing the similar idea in Ref. [203], where the enhanced effect of tube confinement on translation was studied, they have a linear relation:

$$\omega_c = g\omega_b \tag{5.8}$$

where g is a factor controlled by the proximity to the wall, here, which is the width of slit $L_w/2L_h$.

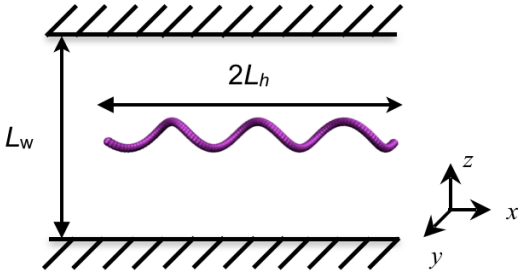

FIGURE 5.14: Schematic of helix confined by a slit with width $L_w/2L_h$

The average net angular displacements in φ direction are $-26°$ and $-29°$,are respectively for $L_w/2L_h = 2$ and $L_w/2L_h = 1$. Therefore, the enhanced factor g in Eq. 5.8 are 1.37 and 1.58.

This increase of swimming speed in the slit can be related to the problem of micro-scale locomotion in polymeric solutions. It is well known that actuated biological flagella generate drag-based thrust due to larger resistance of the normal with respect to tangential motion [204]. When swimming in polymer solutions, flagella undergoing motion normal to its shape push directly onto the neighbouring polymer network, whereas tangential motion barely perturb these micro obstacles [198]. In this case, the drag force increases more in the normal direction than in the tangential one, resulting in larger swimming speeds.

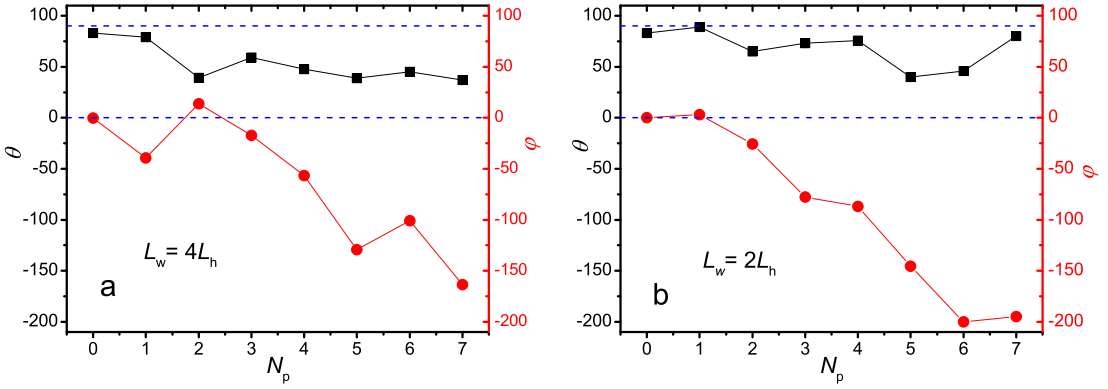

FIGURE 5.15: Time dependence of the angular displacement (θ, φ) with N_T the number of completed periods for a helix confined in a slit with $L_w = 4L_h$. The parameters of deformation loop in Eq. 5.4 are: $\bar{R} = 0.06$, $\Delta R = 0.4$ and $\bar{\alpha}_h = 0.6$, $\Delta\alpha_h = 0.15$. Deformation period $T_p/T_H = 4$.

5.3.2.2 Helix migration

Understanding the trajectories of the swimmers is important in controlled swimming applications. Lauga *et al.* [205] and Gompper *et al.* [72] report that bacteria swim in circular trajectories under force-free and torque-free swimming conditions. For artificial swimmers under confinement, two distinct trajectories stand out, one of which is a helical trajectory close to the channel boundaries when the tail is pushing the head (called pusher-mode) and a straight trajectory close to the center of the channel when the tail pulls the head (called puller-mode) [206].

Here, we tested the trajectories of the deformable helixes for the two different confinement values. The initial position of the mass center of helix is chosen to be a displaced $\pm z = 0.5L_h$ away from the slit center in z direction, with the axis of helix parallel to the channel walls. From Fig. 5.16, it can be inferred that the helix tends to drift towards the slit center in the two different investigated confinement and also for the two symmetric simulation above and below the center.

Although the fluctuating trajectories do not permit a precise quantification, the results in Fig 5.16 show that a well defined drift velocity to the channel center which very clearly increases with confinement. For more confined condition, the helix reaches the slit center at around $N_T = 2$, while the less confined helix drifts more slowly and reaches the slit center at about $N_T = 3.5$. However, the position of helix is oscillating around the slit

center. And the oscillation for $L_w/2L_h = 1$ is between (-2.5, +2.5) while the amplitude of oscillation around 5 for the wider slit ($L_w/2L_h = 2$), which is almost twice as the narrower one. These different behaviors in different slits aredue to the hydrodynamic interactions between helix and walls, which are stronger in narrower slit.

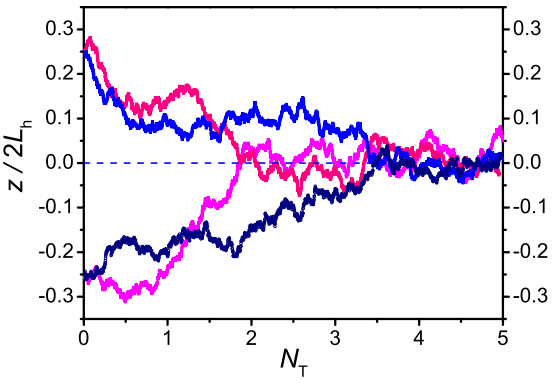

FIGURE 5.16: Time dependence of helix mass center in z direction with N_T the number of periods in a slit. Blue and navy: the width of slit $L_w/2L_h = 2$. Purple and magenta: $L_w/2L_h = 1$. the initial $z/2L_h$ is ± 0.25 for both slits. Employed parameters in Eq: 5.4 are $\bar{R} = 0.06$, $\Delta R = 0.4$ and $\bar{\alpha}_h = 0.6$, $\Delta\alpha_h = 0.15$.

In order to probe that helix migration is an effect related to the hydrodynamics interactions at the non-reciprocal deformation, we perform additional simulation for a passive helix and a helix with reciprocal deformation and quantify also the helix center of mass position. The results in Fig. 5.17 show migrations don't happen to passive helix and helix of reciprocal deformation within 5 periods. For passive helix, there is no hydrodynamic interaction. So the helix just has a Brownian motion. Interestingly, the helix of reciprocal deformation doesn't migrate to slit center, which indicates the reciprocal deformation is non-effective on the hydrodynamic interaction with walls.

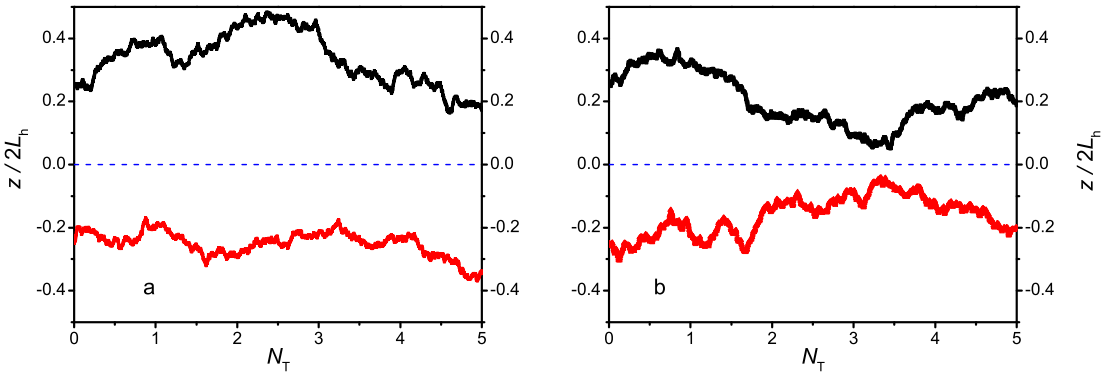

FIGURE 5.17: Time dependence of helix mass center in z direction with N_T the number of periods in a slit. $L_w/2L_h = 2$. The initial position $z/2L_h$ is ± 0.25 for both slits. a) the helix here performs a reciprocal deformation $\phi = \pi/2$. b) passive case, the rigid helix here doesn't have a any deformation. Here N_T indicates a similar time frame as a).

5.4 Summary

Helices are iconic shapes in the mechanics of small-scale locomotion, with many types of swimmers using rotating helicial flagella to generate thrust. Deforming helices are a example of synthetic swimmers which can also create a non-trivial motion. Inspired by the large range of biological systems displaying motion from the deformation of a helix, we considered how an inextensible deforming helix can propel at low Reynolds number. By imposing that the helical shape changes periodically in a non-reciprocal way in a hydrodynamic solvent, we confirm the presence of a helix rotation. This is performed both in bulk and in confinement by means of hydrodynamic simulations. When requiring the swimmer to maintain helical shape at all times, we show that deforming helices can create non-reciprocal rotation in bulk and confinement by a hybrid simulation method.

The value of the net displacements over one period of oscillation depended strongly on the deformation period due to the time scale of hydrodynamic interaction. The helix configuration loop also affects the rotation speed and direction. Furthermore, the more viscous fluid can lead to a faster propulsion until the velocity increases to a peak then decrease with fluid velocity. Our simulation results have good qualitative agreement with experimental [86] and theoretical works [89] where the thermal fluctuations were ignored.

We found that the confinement of the helix in a slit increases the net rotation displacement by directly pushing against the surrounding slit wall. Compared to passive helix or helix of reciprocal deformation, the non-reciprocally deformable helix always tend to migrate to the slit center. The slit width has significant effect on this migration velocity, which is bigger at narrow slit compared to wider silt. The position oscillation is also dependent on the slit width. The narrow slit rises the higher amplitude of oscillation around slit center.

These results in turn can potentially be used to guide the design of other artificial deforming helix systems, similar to the gel helix from Ref. [86]. These predictions could be further improved by obtaining larger statistics or by considering how gel extensibility affects the dynamics. This investigation and optimisation could also lead to the design of tunable artificial swimmers, by introducing to our model how the swimmers react to external fields. Finally, the combination of this model with specific deformation models for the body of a *Spirochaetes* or the polymorphic transitions of a bacterial flagellum, could also help to improve our understanding into how biological systems employ deforming helices to generate motion and their efficiency in doing so.

Chapter 6

Summary and Conclusions

We have investigated the hydrodynamics of rods and helices in dilute suspensions, from tumbling of rods and transport of inextensible helices under shear flow to swimming of active helices.

First, a method has been presented to determine the equivalent hydrodynamic aspect ratio and associated polydispersity for nonspherical axisymmetric nano particles dispersed in a medium. The time evolution of the average orientation angle of dilute suspensions of nonspherical particles upon inception of a shear flow is monitored by means of the polarization modulation method. The orientation angle is a geometric property, such that the time evolution of the orientation angle is essentially dependent on three parameters: hydrodynamic aspect ratio, size polydispersity, and Peclet number. Numerical results have been obtained from Smoluchowski equation under the assumption that the suspension is sufficiently dilute. The advantages of the present method are that it can be applied to arbitrary shear ratio, aspect ratio of particle, and polydispersity. The usefulness of the technique has been demonstrated by determining the aspect ratio and polydispersity in a model quantum dots sample with which other techniques have previously failed. We also anticipate that by matching the refractive index of the suspending medium to that of the particles, the method could soon be extended to the characterization of dense systems, where particle-particle interactions become important. Smoluchowski equation used herein assumes prolate- or oblate-shaped colloids. It is in principle possible to extend our method to more complex-structured colloids. First of all, the Smoluchowski equation should be extended to include bi- or even triaxiality where two or three mutually coupled orientations are involved, and second, the relation between the tumbling frequency and shape parameters must be determined from hydrodynamic numerical calculations and/or simulations. Once this is accomplished, the experimental method can be applied in the same way as for elongated colloids.

Then, we presented a simulation study of the transport of deformable helix in a uniform shear flow. The rigid helices have same tumbling periods with cylinders with same aspect ratios. Tumbling of a flexible helix is coupled with breathing. Moreover, the tumbling periods of flexible helix still follow Jeffery's theory by considering an effective aspect ratio of a cylindrical particle . This effective aspect ratio depends on the helix

flexibility and equilibrium geometry and tends to the equilibrium aspect ratio in the limit of long and rigid helices. The flexible helix would go to chaotic dynamics if the shear stress is big enough and behaves as a flexible polymer. We found hydrodynamics is required to obtain lateral drift, which has a positive linear relation with shear rate, in agreement with experimental results [71]. With respect to the lateral migration, the drift velocity increases with the number of pitches until an asymptotic value. For other geometrical parameters, such as the pitch, the drift velocity shows a maximum at intermediate values which can be understood as a transition between two limits in which the helix is more similar to a rod or to a tube or hollow cylinder. More flexible helices have slower drift velocity since the changing of helix geometry under shear is always located in smaller aspect-ratio regime, in which the drift velocity is smaller than for bigger aspect ratios. These results might be used to design micro-delivery system in medicine. For example, Ref. [66] presents artificially motorized sperm cells - a novel type of hybrid micromotor, where customized microhelices serve as motors for transporting sperm cells with motion deficiencies to help them carry out their natural function. The geometrical structure and flexibility of the microhelix can be tuned to best conditions to optimize the transport velocity of the microhelices. Since the microhelices always transport in some confinement in terms of channel or tubes, the effect of walls can't be negligible in practice. Therefore, before such practical applications can be envisaged, the hydrodynamic interactions between different helices of same and different chirality as well as between helices and walls confining the fluid should all be taken into account.

Finally, we consider "active" helices which are driven by changing cyclicly the helix shape through two degrees of freedom as total length, end-to-end length or wavenumber. We demonstrated that a non-reciprocal deformation leads to net rotation propulsion, which is qualitatively consistent with previous theoretical results [89]. This net rotational displacement can be obtained only when the hydrodynamic interaction can propagate faster or in comparable time as the deformation period. The net rotation is also enhanced by the fluid vicosity within the studied regime. Furthermore, confinement in term of a slit geometry is taken into account for more practical conditions. The slit increases the rotation speed of helix if the slit width is comparable to the end-to-end length of the helix, such that more confined helix has bigger rotational velocity. The deformable helix tends to move towards the slit center because of the wall effect. This is quite different from passive helix and helix with reciprocal deformation, which just does not display this migration behaviour. These results provides criteria for design this sort of artificial helix microfluidic. Especially, the understanding of the helix behaviours under confinement is helpful for experimentists to develop more applications. For instance, this approach may be useful for designing new microfluidic devices that can mix, sort, and circulate fluid. Due to demanding simulations, here the statistics is averaged over 7 deformation periods only which is not enough to obtain more general results. In next step, more complicated confinement, such as tube, or soft walls, should be considered since microswimmers can be expected to be applied for medical purposes, such as soft tubes in organisms.

In summary, the three aspects investigated in this thesis show that the shape-anistropy

of colloids at non-equilibrium can produce many fascinating phenomena in dilute systems. These studies can be extended to consider interaction between multiple polymers structures or dense systems, where the hydrodynamic interactions become more complex and might produce even more interesting collective phenomena.

Appendix A

Numerical solution of the Smoluchowski equation

The time-dependent orientation angle χ is determined by the time evolution of the probability distribution function $P(\hat{\mathbf{u}}, t)$ of the orientation $\hat{\mathbf{u}}$ as given in eq. 4 of the paper. For the case of Rayleigh scatterers, Frattini and Fuller [54] employed the following expression for χ in terms of spherical coordinates (θ, ϕ)

$$\tan 2\chi = \frac{\langle \sin^2\theta \sin 2\phi \rangle}{\langle \sin^2\theta \cos 2\phi \rangle}. \tag{A.1}$$

This expression provides numerical predictions in good agreement with experimental results [54, 55]. The average $\langle \mathrm{A} \rangle$ is calculated according to

$$\langle \mathrm{A} \rangle = \int_0^{\pi} \int_0^{2\pi} \mathrm{A}(\theta, \phi)\, P(\theta, \phi; t) d\theta d\phi \quad , \tag{A.2}$$

where a monodisperse suspension is considered. In order to calculate the time evolution of the orientation angle χ, the time dependence of $P(\theta, \phi; t)$ has to be accounted for. The Smoluchowski equation can be expressed in spherical coordinates as

$$\begin{aligned} \frac{\partial P}{\partial \tau} = & \quad \frac{1}{Pe}\left[\frac{1}{\sin\theta}\frac{\partial}{\partial\theta}\left(\sin\theta\frac{\partial P}{\partial\theta}\right) + \frac{1}{\sin\theta^2}\frac{\partial^2 P}{\partial\phi^2}\right] \\ & - \frac{p^2-1}{p^2+1}\left[\frac{\sin\phi\cos\phi}{\sin\theta}\frac{\partial}{\partial\theta}\left(P\sin^2\theta\cos\theta\right) - \frac{\partial}{\partial\phi}(P\sin^2\phi)\right] \\ & - \frac{1}{p^2+1}\left(\frac{1}{2}\frac{\partial P}{\partial\phi}\right), \end{aligned} \tag{A.3}$$

where $\tau = \dot{\gamma}t$ is the strain, or dimensionless time. For the boundary condition at the two poles, $\theta = 0$ and $\theta = \pi$, the probability density function is given by:

$$P|_{\theta=0} = \left[\sum_{1}^{N_\theta} \left(4P\left(1, j_\theta\right) - P(2, j_\theta)\right)/3\right] \Big/ N_\theta \tag{A.4}$$

$$P|_{\theta=\pi} = \left[\sum_{1}^{N_\theta} \left(4P\left(N_\theta - 1, j_\theta\right) - P(N_\theta - 2, j_\theta)\right)/3\right] \Big/ N_\theta \tag{A.5}$$

where $P(i_\theta, j_\phi)$ is the value of probability density function at the grid point (i_θ, j_ϕ). The probability density function is also continuous so that the periodic condition applies in the azimuthal direction ϕ.

The equation for the averages is here numerically solved for each fixed value of the aspect ratio p, and Peclet number Pe. We use a finite difference method, in which the time term is discretized by 3$^{\text{rd}}$ order TVD (total variation diminishing) Runge-Kutta, while the space terms are discretised by a central difference scheme on a grid domain with N intervals for the θ variable with $(0 \leq \theta \leq \pi)$, and $2N$ intervals for the ϕ variable with $(0 \leq \phi \leq 2\pi)$. The central difference scheme is 2nd order, which, however, gives rise large spurious numerical oscillations for high values of Pe and large time steps when it is used in the convection term. Therefore, in order to guarantee the numerical stability and accuracy of the method, we tested different grids. The grid sensitivity analysis reveals that an accurate solution is obtained by grid systems with $N = 40$ for values from $Pe = 0.1$ to 10^3; grids with $N = 60$ for $Pe = 10^3$ to 10^5; and grids with $N = 150$ for $Pe \geq 10^5$. The integration is here performed by discretizing each of the three terms in eq. A.3, since splitting the second term into smaller terms leads to undesired divergences.

In order to consider the effect of polidispersity, the orientation angle includes an additional averaging with respect to the aspect ratio

$$\langle \mathrm{A} \rangle = \int_0^\pi \int_0^{2\pi} \int_0^\infty \mathrm{A}(\theta, \phi)\, P(\theta, \phi; t) m(p) d\theta d\phi dp \quad , \tag{A.6}$$

where both A and P are implicitly p-dependent. The distribution of aspect ratios $m(p)$ can be approximated by a log-normal distribution

$$m(p) = \frac{1}{p(2\pi)^{1/2} s} \exp\left[\frac{-(\ln p - \mu)^2}{2s^2}\right], \quad p > 0. \tag{A.7}$$

where μ is the location parameter and s the scale parameter, respectively. The average aspect ratio $\bar{p}$, polydispersity σ are then given by

$$\bar{p} = \mathrm{e}^{\mu + s^2/2} \tag{A.8}$$

$$\sigma^2 = \mathrm{e}^{2\mu + s^2}(\mathrm{e}^{s^2} - 1). \tag{A.9}$$

The continuous distribution of aspect ratios is discretized into $N_\sigma = 30$ discrete values, which proves to be sufficient to obtain accurate results. The program calculates $\chi(\dot{\gamma}t)$,

for various input values, namely the physical parameters (Pe, p, σ), and the integrating parameters (N, N_σ).

Bibliography

[1] Albert Einstein. Über die von der molekularkinetischen theorie der wärme geforderte bewegung von in ruhenden flüssigkeiten suspendierten teilchen. *Annalen der physik*, 322(8):549–560, 1905.

[2] Marian Von Smoluchowski. Zur kinetischen theorie der brownschen molekularbewegung und der suspensionen. *Annalen der physik*, 326(14):756–780, 1906.

[3] M. Doi and S. F. Edwards. *The theory of polymer dynamics*, volume 73. Oxford University Press, 1988.

[4] Jean Perrin. Mouvement brownien et réalité moléculaire. In *Annales de Chimie et de Physique*, volume 18, pages 5–104, 1909.

[5] Pablo Herves, Moisés Pérez-Lorenzo, Luis M Liz-Marzán, Joachim Dzubiella, Yan Lu, and Matthias Ballauff. Catalysis by metallic nanoparticles in aqueous solution: model reactions. *Chemical Society Reviews*, 41(17):5577–5587, 2012.

[6] A. Okagawa, Cox R. G., and S. G Mason. The kinetics of flowing dispersions. vi. transient orientation and rheological phenomena of rods and discs in shear flow. *J. Colloid Interface Sci.*, 45:303, 1973.

[7] R. G. Winkler, K. Mussawisade, M. Ripoll, and G. Gompper. Rod-like colloids and polymers in shear flow: a multi-particle-collision dynamics study. *J. Phys.: Condens. Matter*, 16:3941, 2004.

[8] R. G. Winkler. Semiflexible polymers in shear flow. *Phys. Rev. lett.*, 97:128301, 2006.

[9] J. K. G. Dhont. *An Introduction to Dynamics of Colloids*. Elsevier: Amsterdam, The Netherlands, 1996.

[10] Marcos, H. C. Fu, T. R. Powers, and R. Stocker. Separation of microscale chiral objects by shear flow. *Phys. Rev. lett.*, 102:158103, Apr 2009.

[11] M. Makino, L. Arai, and M. Doi. Shear migration of chiral particle in parallel-disk. *Journal of the Physical Society of Japan*, 77(6):064404, 2008.

[12] M. Kostur, M. Schindler, P. Talkner, and P. Hänggi. Chiral separation in microflows. *Phys. Rev. lett.*, 96:014502, Jan 2006.

[13] L. E. Becker, S. A. Koehler, and H. A. Stone. On self-propulsion of micro-machines at low reynolds number: Purcell's three-link swimmer. *Journal of fluid mechanics*, 490:15–35, 2003.

[14] E. M. Purcell. Life at low reynolds number. *American Journal of Physics*, 45(1): 3–11, 1977.

[15] L. Turner, W. S. Ryu, and H. C. Berg. Real-time imaging of fluorescent flagellar filaments. *Journal of bacteriology*, 182(10):2793–2801, 2000.

[16] R. E. Goldstein. Green algae as model organisms for biological fluid dynamics. *Annual Review of Fluid Mechanics*, 47:343–375, 2015.

[17] J. T. Locsei. Persistence of direction increases the drift velocity of run and tumble chemotaxis. *Journal of Mathematical Biology*, 55(1):41–60, 2007.

[18] Cornelis G De Kruif, Thom Huppertz, Volker S Urban, and Andrei V Petukhov. Casein micelles and their internal structure. *Advances in Colloid and Interface Science*, 171:36–52, 2012.

[19] Jin-Gyu Park, Jason D Forster, and Eric R Dufresne. High-yield synthesis of monodisperse dumbbell-shaped polymer nanoparticles. *Journal of the American Chemical Society*, 132(17):5960–5961, 2010.

[20] Jung Kwon Oh, Ray Drumright, Daniel J Siegwart, and Krzysztof Matyjaszewski. The development of microgels/nanogels for drug delivery applications. *Progress in Polymer Science*, 33(4):448–477, 2008.

[21] HC Longuet-Higgins and B Widom. A rigid sphere model for the melting of argon. *Molecular Physics*, 8(6):549–556, 1964.

[22] Dieter M Herlach, Ina Klassen, Patrick Wette, and Dirk Holland-Moritz. Colloids as model systems for metals and alloys: a case study of crystallization. *Journal of physics: Condensed Matter*, 22(15):153101, 2010.

[23] Valerie J Anderson and Henk NW Lekkerkerker. Insights into phase transition kinetics from colloid science. *Nature*, 416(6883):811, 2002.

[24] Francis Perrin. Mouvement brownien d'un ellipsoide (ii). rotation libre et dépolarisation des fluorescences. translation et diffusion de molécules ellipsoidales. *Journal de Physique et le Radium*, 7(1):1–11, 1936.

[25] Lars Onsager. The effects of shape on the interaction of colloidal particles. *Annals of the New York Academy of Sciences*, 51(4):627–659, 1949.

[26] Hartmut Löwen. Brownian dynamics of hard spherocylinders. *Physical Review E*, 50(2):1232, 1994.

[27] J Schwarz-Linek, C Valeriani, A Cacciuto, ME Cates, D Marenduzzo, AN Morozov, and WCK Poon. Phase separation and rotor self-assembly in active particle suspensions. *Proceedings of the National Academy of Sciences*, 109(11):4052–4057, 2012.

[28] CC Ho, A Keller, JA Odell, and RH Ottewill. Preparation of monodisperse ellipsoidal polystyrene particles. *Colloid and Polymer Science*, 271(5):469–479, 1993.

[29] Carlos M van Kats, Patrick M Johnson, Jan EAM van den Meerakker, and Alfons van Blaaderen. Synthesis of monodisperse high-aspect-ratio colloidal silicon and silica rods. *Langmuir*, 20(25):11201–11207, 2004.

[30] Anieke M Wierenga, Tjerk AJ Lenstra, and Albert P Philipse. Aqueous dispersions of colloidal gibbsite platelets: synthesis, characterisation and intrinsic viscosity measurements. *Colloids and Surfaces A: Physicochemical and Engineering Aspects*, 134(3):359–371, 1998.

[31] Patrick M Johnson, Carlos M van Kats, and Alfons van Blaaderen. Synthesis of colloidal silica dumbbells. *Langmuir*, 21(24):11510–11517, 2005.

[32] Xiujuan Zhang, Cheng Dong, Juan Antonio Zapien, Shafiq Ismathullakhan, Zhenhui Kang, Jiansheng Jie, Xiaohong Zhang, Jack C Chang, Chun-Sing Lee, and Shuit-Tong Lee. Polyhedral organic microcrystals: from cubes to rhombic dodecahedra. *Angewandte Chemie International Edition*, 48(48):9121–9123, 2009.

[33] Miharu Eguchi, Daisuke Mitsui, Hsin-Lun Wu, Ryota Sato, and Toshiharu Teranishi. Simple reductant concentration-dependent shape control of polyhedral gold nanoparticles and their plasmonic properties. *Langmuir*, 28(24):9021–9026, 2012.

[34] Eric C Greyson, Jeremy E Barton, and Teri W Odom. Tetrahedral zinc blende tin sulfide nano-and microcrystals. *Small*, 2(3):368–371, 2006.

[35] Guangjun Zhou, Mengkai Lü, Zhiliang Xiu, Shufen Wang, Haiping Zhang, Yuanyuan Zhou, and Shumei Wang. Controlled synthesis of high-quality pbs star-shaped dendrites, multipods, truncated nanocubes, and nanocubes and their shape evolution process. *The Journal of Physical Chemistry B*, 110(13):6543–6548, 2006.

[36] D Frenkel, BM Mulder, and JP McTague. Phase diagram of a system of hard ellipsoids. *Physical Review Letters*, 52(4):287, 1984.

[37] Ronald Blaak, Daan Frenkel, and Bela M Mulder. Do cylinders exhibit a cubatic phase? *The Journal of Chemical Physics*, 110(23):11652–11659, 1999.

[38] Bing Liu, Thijs H Besseling, Michiel Hermes, Ahmet F Demirörs, Arnout Imhof, and Alfons Van Blaaderen. Switching plastic crystals of colloidal rods with electric fields. *Nature Communications*, 5:3092, 2014.

[39] Rui Zhang and Kenneth S Schweizer. Theory of coupled translational-rotational glassy dynamics in dense fluids of uniaxial particles. *Physical Review E*, 80(1): 011502, 2009.

[40] Peter J Collings. *Liquid crystals: nature's delicate phase of matter*. Princeton University Press, 2002.

[41] Alfons van Blaaderen. Colloids under external control. *Mrs Bulletin*, 29(2):85–90, 2004.

[42] Daisuke Nagao, Maki Sugimoto, Ayako Okada, Haruyuki Ishii, Mikio Konno, Arnout Imhof, and Alfons Van Blaaderen. Directed orientation of asymmetric composite dumbbells by electric field induced assembly. *Langmuir*, 28(16):6546–6550, 2012.

[43] S. Tottori, L. Zhang, F. Qiu, K. K. Krawczyk, A. Franco-Obregn, and B. J. Nelson. Magnetic helical micromachines: Fabrication, controlled swimming, and cargo transport. *Advanced Materials*, 24(6):811–816.

[44] C-C Huang, G Sutmann, G Gompper, and RG Winkler. Tumbling of polymers in semidilute solution under shear flow. *EPL (Europhysics Letters)*, 93(5):54004, 2011.

[45] M. Makino and M. Doi. Migration of twisted ribbon-like particles in simple shear flow. *Physics of Fluids*, 17(10):103605, 2005.

[46] SE Paulin and Bruce J Ackerson. Observation of a phase transition in the sedimentation velocity of hard spheres. *Physical Review Letters*, 64(22):2663, 1990.

[47] Ahmet Faik Demirors, Patrick M Johnson, Carlos M van Kats, Alfons van Blaaderen, and Arnout Imhof. Directed self-assembly of colloidal dumbbells with an electric field. *Langmuir*, 26(18):14466–14471, 2010.

[48] A Van Blaaderen, M Dijkstra, RHHG van Roij, A Imhof, M Kamp, BW Kwaadgras, T Vissers, and B Liu. Manipulating the self assembly of colloids in electric fields. *The European Physical Journal Special Topics*, 222(11):2895–2909, 2013.

[49] Matthieu Marechal and Marjolein Dijkstra. Colloidal hard dumbbells under gravity: structure and crystallization. *Soft Matter*, 7(4):1397–1408, 2011.

[50] Michael C Wendl. General solution for the couette flow profile. *Physical Review E*, 60(5):6192, 1999.

[51] N Koumakis, AB Schofield, and G Petekidis. Effects of shear induced crystallization on the rheology and ageing of hard sphere glasses. *Soft Matter*, 4(10), 2008.

[52] Alessio Zaccone, Daniele Gentili, Hua Wu, Massimo Morbidelli, and Emanuela Del Gado. Shear-driven solidification of dilute colloidal suspensions. *Physical Review Letters*, 106(13):138301, 2011.

[53] Paul H Kaye. Spatial light-scattering analysis as a means of characterizing and classifying non-spherical particles. *Measurement Science and Technology*, 9(2):141, 1998.

[54] P. L. Frattini and G. G. Fuller. The dynamics of dilute colloidal suspensions subject to time-dependent flow-fields by conservative dichroism. *J. Colloid Interface Sci.*, 2:506, 1984.

[55] P. L. Frattini and G. G. Fuller. Conservative dichroism of a sheared suspension in the rayleigh-gans light-scattering approximation. *J. Colloid Interface Sci.*, 119: 335, 1987.

[56] Johnson S. J. and Fuller G. G. The optical anisotropy of sheared hematite suspensions. *J. Colloid Interface Sci.*, 124:441, 1988.

[57] J. Vermant, H. Yang, and G. G. Fuller. Rheooptical determination of aspect ratio and polydispersity of nonspherical particles. *AIChE J.*, 47:790, 2001.

[58] N. K. Reddy, J. Perez-Juste, Isabel Pastoriza-Santos, P. R. Lang, J. K. G. Dhont, L. M. Liz-Marzan, and J. Vermant. Flow dichroism as a reliable method to measure the hydrodynamic aspect ratio of gold nanoparticles. *ACS nano*, 5(6):4935–4944, 2011.

[59] J. Nicolle. *Louis Pasteur: A master of scientific enquiry.* Scientific Book Guild, 1962.

[60] M. Daoud and C. E. Williams. *Soft matter physics.* Springer, Berlin, 1999.

[61] C. McManus. *Right hand, left hand: The origins of asymmetry in brains, bodies, atoms and cultures.* Harvard University Press, 2004.

[62] P. Ball. *Designing the molecular world: Chemistry at the frontier.* Princeton University Press, 1996.

[63] Michiya Fujiki. Optically active polysilylenes: state-of-the-art chiroptical polymers. *Macromolecular rapid communications*, 22(8):539–563, 2001.

[64] Debora Schamel, Andrew G Mark, John G Gibbs, Cornelia Miksch, Konstantin I Morozov, Alexander M Leshansky, and Peer Fischer. Nanopropellers and their actuation in complex viscoelastic media. *ACS nano*, 8(9):8794–8801, 2014.

[65] Eli D Sone, Eugene R Zubarev, and Samuel I Stupp. Semiconductor nanohelices templated by supramolecular ribbons. *Angewandte Chemie International Edition*, 41(10):1705–1709, 2002.

[66] Mariana Medina-Sánchez, Lukas Schwarz, Anne K Meyer, Franziska Hebenstreit, and Oliver G Schmidt. Cellular cargo delivery: Toward assisted fertilization by sperm-carrying micromotors. *Nano letters*, 16(1):555–561, 2015.

[67] C. Fujimoto. Enantiomer separation by capillary electrochromatography using fritless packed columns. *Analytical Sciences*, 18(1):19–25, 2002.

[68] G. Gübitz and M. G. Schmid. Recent advances in chiral separation principles in capillary electrophoresis and capillary electrochromatography. *Electrophoresis*, 25 (23-24):3981–3996, 2004.

[69] PG De Gennes. Mechanical selection of chiral crystals. *EPL (Europhysics Letters)*, 46(6):827, 1999.

[70] M. Kostur, M. Schindler, P. Talkner, and P. Hänggi. Chiral separation in microflows. *Phys. Rev. lett.*, 96(1):014502, 2006.

[71] M. Doi and M. Makino. Sedimentation of particles of general shape. *Physics of Fluids*, 17(4):043601, 2005.

[72] J. Elgeti, R. G. Winkler, and G. Gompper. Physics of microswimmerssingle particle motion and collective behavior: a review. *Reports on progress in physics*, 78 (5):056601, 2015.

[73] J. Gray and G. J. Hancock. The propulsion of sea-urchin spermatozoa. *Journal of Experimental Biology*, 32(4):802–814, 1955.

[74] S. Ramaswamy. The mechanics and statistics of active matter. *Annu. Rev. Condens. Matter Phys.*, 1(1):323–345, 2010.

[75] F. J. Ndlec, T. Surrey, A. C. Maggs, and S. Leibler. Self-organization of microtubules and motors. *Nature*, 389(6648):305, 1997.

[76] K. Kruse, J. F. Joanny, F. Juelicher, J Prost, and K. Sekimoto. Asters, vortices, and rotating spirals in active gels of polar filaments. *Phys. Rev. lett.*, 92(7):078101, 2004.

[77] Y. Harada, A. Noguchi, A. Kishino, and T. Yanagida. Sliding movement of single actin filaments on one-headed myosin filaments. *Nature*, 326(6115):805, 1987.

[78] V. Schaller, C. Weber, C. Semmrich, E. Frey, and A. R. Bausch. Polar patterns of driven filaments. *Nature*, 467(7311):73, 2010.

[79] C. Bechinger, R. Di Leonardo, H. Löwen, C. Reichhardt, G. Volpe, and G. Volpe. Active particles in complex and crowded environments. *Reviews of Modern Physics*, 88(4):045006, 2016.

[80] T. Vicsek. Collective motion. *Physics Reports*, 517:71, 2012.

[81] M. C. Marchetti, J-F. Joanny, S. Ramaswamy, T. B. Liverpool, J. Prost, M. Rao, and R. A. Simha. Hydrodynamics of soft active matter. *Reviews of Modern Physics*, 85(3):1143, 2013.

[82] E Lauga and T. R. Powers. The hydrodynamics of swimming microorganisms. *Reports on Progress in Physics*, 72(9):096601, 2009.

[83] M. C. Marchetti, Y. Fily, S. Henkes, A. Patch, and D. Yllanes. Minimal model of active colloids highlights the role of mechanical interactions in controlling the emergent behavior of active matter. *Current Opinion in Colloid & Interface Science*, 21:34–43, 2016.

[84] R. Dreyfus, J. Baudry, M. L. Roper, M. Fermigier, H. A. Stone, and J. Bibette. Microscopic artificial swimmers. *Nature*, 437(7060):862, 2005.

[85] William M Durham, John O Kessler, and Roman Stocker. Disruption of vertical motility by shear triggers formation of thin phytoplankton layers. *Science*, 323 (5917):1067–1070, 2009.

[86] A. Mourran, H. Zhang, R. Vinokur, and M. Möller. Soft microrobots employing nonequilibrium actuation via plasmonic heating. *Advanced Materials*, 29(2): 1604825, 2017.

[87] R. Kapral. *Multiparticle Collision Dynamics: Simulation of Complex Systems on Mesoscales*, pages 89–146. Wiley-Blackwell, 2008. ISBN 9780470371572.

[88] G. Gompper, T. Ihle, D. M. Kroll, and R. G. Winkler. *Multi-Particle Collision Dynamics: A Particle-Based Mesoscale Simulation Approach to the Hydrodynamics of Complex Fluids*, pages 1–87. Springer Berlin Heidelberg, Berlin, Heidelberg, 2009. ISBN 978-3-540-87706-6.

[89] L. Koens, H. Zhang, M. Moeller, A. Mourran, and E. Lauga. The swimming of a deforming helix. *The European Physical Journal E*, 41(10):119, 2018.

[90] J. K. G. Dhont and K. Kang. Electric-field-induced polarization and interactions of uncharged colloids in salt solutions. *Eur. Phys. J. E*, 33:51–68, 2010.

[91] J. K. G Dhont. *An introduction to dynamics of colloids*, volume 2. Elsevier, 1996.

[92] J. K. G Dhont and W. J. Briels. Rod-like brownian particles in shear flow. *Soft Matter: Complex Colloidal Suspensions, edited by G. Gompper, M. Schick*, 2, 2006.

[93] C-C. Huang, G. Gompper, and R. G. Winkler. Hydrodynamic correlations in multiparticle collision dynamics fluids. *Phys. Rev. E*, 86:056711, Nov 2012.

[94] E. E. Keaveny, S. W. Walker, and M. J. Shelley. Optimization of chiral structures for microscale propulsion. *Nano Letters*, 13(2):531–537, 2013. doi: 10.1021/nl3040477.

[95] A. Ghosh and P. Fischer. Controlled propulsion of artificial magnetic nanostructured propellers. *Nano Letters*, 9(6):2243–2245, 2009. PMID: 19413293.

[96] L. Zhang, J. J. Abbott, L. Dong, B. E. Kratochvil, D. Bell, and B. J. Nelson. Artificial bacterial flagella: Fabrication and magnetic control. *Applied Physics Letters*, 94(6):064107, 2009.

[97] D. Schamel, A. G. Mark, J. G. Gibbs, C. Miksch, K. I. Morozov, A. M. Leshansky, and P. Fischer. Nanopropellers and their actuation in complex viscoelastic media. *ACS Nano*, 8(9):8794–8801, 2014.

[98] J. Gray and G. J. Hancock. The propulsion of sea-urchin spermatozoa. *Journal of Experimental Biology*, 32(4):802–814, 1955. ISSN 0022-0949.

[99] B. de Lima Bernardo and F Moraes. Simplified model for the dynamics of a helical flagellum. *American Journal of Physics*, 79(7):736–740, 2011.

[100] O. Raz and J. E Avron. Swimming, pumping and gliding at low reynolds numbers. *New Journal of Physics*, 9(12):437, 2007.

[101] R. E. Johnson and C. J. Brokaw. Flagellar hydrodynamics. a comparison between resistive-force theory and slender-body theory. *Biophysical journal*, 25(1):113–127, 1979.

[102] M. Kim and A. A. Julius. *Microbiorobotics: biologically inspired microscale robotic systems*. William Andrew, 2012.

[103] H. Gadêlha, E. A. Gaffney, D. J. Smith, and J. C. Kirkman-Brown. Nonlinear instability in flagellar dynamics: a novel modulation mechanism in sperm migration. *Journal of The Royal Society Interface*, 7(53):1689–1697, 2010. ISSN 1742-5689.

[104] R. G. Cox. The motion of long slender bodies in a viscous fluid part 1. general theory. *Journal of Fluid Mechanics*, 44(4):791810, 1970.

[105] G. K. Batchelor. Slender-body theory for particles of arbitrary cross-section in stokes flow. *Journal of Fluid Mechanics*, 44(3):419–440, 1970.

[106] J. Lighthill. Flagellar hydrodynamics. *SIAM review*, 18(2):161–230, 1976.

[107] M. P. Allen and D. J. Tildesley. Computer simulation of liquids oxford university press oxford 385. 1987.

[108] A. Malevanets and R. Kapral. Mesoscopic model for solvent dynamics. *The Journal of Chemical Physics*, 110(17):8605–8613, 1999.

[109] T. Ihle and D. M. Kroll. Stochastic rotation dynamics: A galilean-invariant mesoscopic model for fluid flow. *Phys. Rev. E*, 63:020201, Jan 2001.

[110] I. O. Götze, H. Noguchi, and G. Gompper. Relevance of angular momentum conservation in mesoscale hydrodynamics simulations. *Phys. Rev. E*, 76:046705, Oct 2007.

[111] A. Malevanets and J. M. Yeomans. Dynamics of short polymer chains in solution. *EPL (Europhysics Letters)*, 52(2):231, 2000.

[112] G. Rückner and R. Kapral. Chemically powered nanodimers. *Phys. Rev. lett.*, 98: 150603, Apr 2007.

[113] K. Mussawisade, M. Ripoll, R. G. Winkler, and G. Gompper. Dynamics of polymers in a particle-based mesoscopic solvent. *The Journal of Chemical Physics*, 123 (14):144905, 2005.

[114] A. Malevanets and R. Kapral. Mesoscopic multi-particle collision model for fluid flow and molecular dynamics. In *Novel Methods in Soft Matter Simulations*, pages 116–149. Springer, 2004.

[115] M. Ripoll, R. G. Winkler, and G. Gompper. Star polymers in shear flow. *Phys. Rev. Lett.*, 96:188302, May 2006.

[116] E. Tuezel, M. Strauss, T. Ihle, and D. M. Kroll. Transport coefficients for stochastic rotation dynamics in three dimensions. *Phys. Rev. E*, 68:036701, 2003.

[117] M. Ripoll, K. Mussawisade, R. G. Winkler, and G. Gompper. Dynamic regimes of fluids simulated by multiparticle-collision dynamics. *Phys. Rev. E*, 72:016701, 2005.

[118] M. Ripoll, R. G. Winkler, and G Gompper. Hydrodynamic screening of star polymers in shear flow. *The European Physical Journal E*, 23(4):349–354, 2007.

[119] M. V. Kovalenko, L. Manna, A. Cabot, Z. Hens, D. V. Talapin, C. R. Kagan, V. I. Klimov, A. L. Rogach, P. Reiss, D. J. Milliron, P. Guyot-Sionnnest, G. Konstantatos, W. J. Parak, T. Hyeon, B. A. Korgel, C. B. Murray, and W. Heiss. Prospects of nanoscience with nanocrystals. *ACS Nano*, 9:1012–1057, 2015.

[120] A. P. Alivisatos. Semiconductor clusters, nanocrystals, and quantum dots. *Science*, 271:933–937, 1996.

[121] R. Krahne, G. Morello, A. Figuerola, C. George, S. Deka, and L. Manna. Physical properties of elongated inorganic nanoparticles. *Physics Reports*, 501:75–221, 2011.

[122] P. D. Cunningham, J. B. Souza, I. Fedin, C. X. She, B. Lee, and D. V. Talapin. Assessment of anisotropic semiconductor nanorod and nanoplatelet heterostructures with polarized emission for liquid crystal display technology. *ACS Nano*, 10: 5769–5781, 2016.

[123] A. Sitt, A. Salant, G. Menagen, and U. Banin. Highly emissive nano rod-in-rod heterostructures with strong linear polarization. *Nano Letters*, 11:2054–2060, 2011.

[124] J. S. Kamal, R. Gomes, Z. Hens, M. Karvar, K. Neyts, S. Compernolle, and F. Vanhaecke. Direct determination of absorption anisotropy in colloidal quantum rods. *Phys. Rev. B*, 85:035126, 2012.

[125] Y. Shirasaki, G. J. Supran, M. G. Bawendi, and V. Bulovic. Emergence of colloidal quantum-dot light-emitting technologies. *Nature Photonics*, 7:13–23, 2013.

[126] K. T. Shimizu, M. Böhmer, D. Estrada, S. Gangwal, S. Grabowski, H. Bechtel, E. Kang, K. J. Vampola, D. Chamberlin, O. B. Shchekin, and J. Bhardwaj. Toward commercial realization of quantum dot based white light-emitting diodes for general illumination. *Photonics Res.*, 5:A1–A6, 2017.

[127] G. H. Carey, A. L. Abdelhady, Z. J. Ning, S. M. Thon, O. M. Bakr, and E. H. Sargent. Colloidal quantum dot solar cells. *Chem. Rev.*, 115:12732–12763, 2015.

[128] T. Rauch, M. Boberl, S. F. Tedde, J. Furst, M. V. Kovalenko, G. N. Hesser, U. Lemmer, W. Heiss, and O. Hayden. Near-infrared imaging with quantum-dot-sensitized organic photodiodes. *Nature Photonics*, 3:332–336, 2009.

[129] P. E. Malinowski, E. Georgitzikis, J. Maes, I. Vamvaka, F. Frazzica, J. Van Olmen, P. De Moor, P. Heremans, Z. Hens, and D. Cheyns. Thin-film quantum dot photodiode for monolithic infrared image sensors. *Sensors*, 17:2867, 2017.

[130] F. J. Fan, O. Voznyy, R. P. Sabatini, K. T. Bicanic, M. M. Adachi, J. R. McBride, K. R. Reid, Y. S. Park, X. Y. Li, A. Jain, R. Quintero-Bermudez, M. Saravanapavanantham, M. Liu, M. Korkusinski, P. Hawrylak, V. I. Klimov, S. J. Rosenthal, S. Hoogland, and E. H. Sargent. Continuous-wave lasing in colloidal quantum dot solids enabled by facet-selective epitaxy. *Nature*, 544:75–79, 2017.

[131] W. Xie, T. Stöferle, G. Rainò, T. Aubert, S. Bisschop, Y. Zhu, R. F. Mahrt, P. Geiregat, E. Brainis, Z. Hens, and D. Van Thourhout. On-chip integrated quantum-dot silicon-nitride microdisk lasers. *Adv. Mater.*, 29:1604866, 2017.

[132] X. Michalet, F. F. Pinaud, L. A. Bentolila, J. M. Tsay, S. Doose, J. J. Li, G. Sundaresan, A. M. Wu, S. S. Gambhir, and S. Weiss. Quantum dots for live cells, in vivo imaging, and diagnostics. *Science*, 307:538–544, 2005.

[133] N. V. Beloglazova, I. Y. Goryacheva, R. Niessner, and D. A Knopp. Comparison of horseradish peroxidase, gold nanoparticles and quantum dots as labels in non-instrumental gel-based immuno- assay. *Microchim. Acta.*, 175:361–367, 2011.

[134] B.O. Dabbousi, J. Rodriguez-Viejo, F. V. Mikulec, J. R. Heine, H. Mattoussi, R. Ober, K. F. Jensen, and M. G. Bawendi. (cdse)zns core-shell quantum dots: Synthesis and characterization of a size series of highly luminescent nanocrystallites. *J. Phys. Chem. B*, 101:9463–9475, 1997.

[135] W. Liu, M. Howarth, A. B. Greytak, Y. Zheng, D. G. Nocera, A. Y. Ting, and M. G. Bawendi. Compact biocompatible quantum dots functionalized for cellular imaging. *J. Am. Chem. Soc.*, 130:1274–1284, 2008.

[136] A. C. Vinayaka, S. Basheer, and M. S. Thakur. Bioconjugation of cdte quantum dot for the detection of 2,4-dichlorophenoxyacetic acid by competitive fluoroimmunoassay based biosensor. *Biosens. Bioelectron*, 24:1615–1620, 2009.

[137] T. Aubert, L. Palangetic, M. Mohammadimasoudi, K. Neyts, J. Beeckman, C. Clasen, and Z. Hens. Large-scale and electroswitchable polarized emission from semiconductor nanorods aligned in polymeric nanofibers. *ACS Photonics*, 2: 583–588, 2015.

[138] K. Bong Hoon, O.M. Serdar, L. Jong Bin, N. Sooji, O. Nuri, K. Hojun, Y. Ki Jun, L. Jung Woo, K. Jae-Hwan, K. Seung-Kyun, C. Hwan Lee, J. Lee, J. Ho Shin, N. Heon Kim, C. Leal, M. Shim, and J.A. Rogers. High-resolution patterns of quantum dots formed by electrohydrodynamic jet printing for light-emitting diodes. *Nano letters*, 15:969–973, 2015.

[139] C. Kokkinos, M. Prodromidis, A. Economou, P. Petrou, and S. Kakabakos. Quantum dot-based electrochemical dna biosensor using a screen-printed graphite surface with embedded bismuth precursor. *Electrochem. Commun.*, 60:47–51, 2015.

[140] X. Wang. Recent progress in colloidal quantum dot photovoltaics. *Front. Optoelectron.*, 8:241–251, 2015.

[141] V. R. Dugyala, S. V. Daware, and M. G. Basavaraj. Shape anisotropic colloids: synthesis, packing behavior, evaporation driven assembly, and their application in emulsion stabilization. *Soft Matter*, 9:6711–6725, 2013.

[142] S. C. Glotzer and M. J. Solomon. Anisotropy of building blocks and their assembly into complex structures. *Nature Material*, 6:557–562, 2007.

[143] J. Mewis and Wagner N. J. *Colloidal Suspension Rheology.* Cambridge University Press, 2012.

[144] M. P. Lettinga, J. K. G. Dhont, Z. Zhang, S. Messlinger, and G. Gompper. Hydrodynamic interactions in rod suspensions with orientational ordering. *Soft Matter*, 6:4556–4562, 2010.

[145] K. Kang, A. Wilk, A. Patkowski, and J. K. G. Dhont. Diffusion of spheres in isotropic and nematic networks of rods: Electrostatic interactions and hydrodynamic screening. *J. Chem. Phys.*, 126:214501, 2006.

[146] K. Kang and J. K. G. Dhont. Double-layer polarization induced transitions in suspensions of colloidal rods. *(EPL) Europhysics Letter*, 84:14005, 2008.

[147] K. Kang and J. K. G. Dhont. Electric-field induced transitions in suspensions of charged colloidal rods. *Soft Matter*, 6:273–286, 2010.

[148] V. R. Dugyala and M. G. Basavaraj. Control over coffee-ring formation in evaporating liquid drops containing ellipsoids. *Langmuir*, 30:8680–8686, 2014.

[149] H Lama, R Mondal, M. G. Basavaraj, and D. K. Satapathy. Cracks in dried deposits of hematite ellipsoids: Interplay between magnetic and hydrodynamic torques. *J. Colloid Interface Sci.*, 510:172–180, 2018.

[150] C. Hamon, S. Novikov, L. Scarabelli, L. Basabe-Desmonts, and L. M. Liz-Marzan. Hierarchical self-assembly of gold nanoparticles into patterned plasmonic nanostructures. *ACS Nano*, 8:10694–10703, 2014.

[151] N. Winckelmans, T. Altantzis, M. Grzelczak, A. Sanchez-Iglesias, L. M. Liz-Marzan, and S. Bals. Multimode electron tomography as a tool to characterize the internal structure and morphology of gold nanoparticles. *J. Phys. Chem. C*, in press, 2018.

[152] S. Bals, B. Goris, L. M. Liz-Marzan, and Van Tendeloo G. Three-dimensional characterization of metal nanoparticles and their assemblies by electron tomography. *Angew. Chem. Int. Ed.*, 53:10600–10610, 2014.

[153] M. Grzelczak, A. Sanchez-Iglesias, and L. M. Liz-Marzan. A general approach toward polymer-coated plasmonic nanostructures. *Cryst. Eng. Comm*, 16:9425–9429, 2014.

[154] B. J. Berne and R. Pecora. *Dynamic light scattering: with applications to chemistry, biology, and physics,*. Dover Publications, 2000.

[155] H. C. van de Hulst. *Light scattering by small particles*. New York (John Wiley and Sons), 1957.

[156] G. G. Fuller. *Optical rheometry of complex fluids*. Oxford University Press: Oxford, 1995.

[157] R. Dierick, F. Van den Broeck, K. De Nolf, Q. Zhao, A. Vantomme, J. C. Martins, and Z. Hens. Surface chemistry of $cuins_2$ colloidal nanocrystals, tight binding of l-type ligands. *Chem. Mater.*, 26:5950–5957, 2014.

[158] L. Carbone, C. Nobile, M. De Giorgi, F. Della Sala, G. Morello, P. Pompa, M. Hytch, E. Snoeck, A. Fiore, I. R. Franchini, M. Nadasan, A.F. Silvestre, L. Chiodo, S. Kudera, R. Cingolani, R. Krahne, and L. Manna. ynthesis and micrometer-scale assembly of colloidal cdse/cds nanorods prepared by a seeded growth approach. *Nano Lett.*, 7:2942–2950, 2007.

[159] L. Pellens, J. Vermant, and J. Mewis. Deviations from the stress-optical relation in telechelic associative polymer solutions. *Macromolecules*, 38:1911, 2005.

[160] G. B. Jeffery. , the motion of ellipsoidal particles immersed in a viscous fluid. *Proc. Roy Soc. Ser. A*, 102:161, 1922.

[161] A. Okagawa, R. G. Cox, and S. G. Mason. The kinetics of flowing dispersions. vi transient orientation and rheological phenomena of rods and discs in shear flow. *J. Coll. Interf. Sci.*, 45:3003–329, 1973.

[162] C. Aust, M. Köger, and S. Hess. Structure and dynamics of dilute polymer solutions under shear flow via nonequilibrium molecular dynamics. 32:5660–5672, 1999.

[163] P. Chen and C.-H. Chao. Lift forces of screws in shear flows. *Physics of Fluids*, 19(1):017108, 2007.

[164] J. B. Clemens, O. Kibar, and M. Chachisvilis. A molecular propeller effect for chiral separation and analysis. *Nature Communications*, 6:7868 EP –, 07 2015.

[165] A. D'Urso, R. Randazzo, L. LoFaro, and R. Purrello. Vortexes and nanoscale chirality. *Angewandte Chemie International Edition*, 49(1):108–112, 2010.

[166] H. Brenner. The stokes resistance of an arbitrary particleiii: Shear fields. *Chemical Engineering Science*, 19(9):631 – 651, 1964. ISSN 0009-2509.

[167] Y.-J. Kim and W.J. Rae. Separation of screw-sensed particles in a homogeneous shear field. *International Journal of Multiphase Flow*, 17(6):717 – 744, 1991. ISSN 0301-9322.

[168] R. Eichhorn. Enantioseparation in microfluidic channels. *Chemical Physics*, 375 (2):568 – 577, 2010. ISSN 0301-0104. Stochastic processes in Physics and Chemistry (in honor of Peter Hnggi).

[169] R. Eichhorn. Microfluidic sorting of stereoisomers. *Phys. Rev. lett.*, 105:034502, Jul 2010.

[170] S. Meinhardt, J. Smiatek, R. Eichhorn, and F. Schmid. Separation of chiral particles in micro- or nanofluidic channels. *Phys. Rev. lett.*, 108:214504, May 2012.

[171] M. M. T. Alcanzare, V. Thakore, S. T. T. Ollila, M. Karttunen, and T. Ala-Nissila. Controlled propulsion and separation of helical particles at the nanoscale. *Soft Matter*, 13:2148–2154, 2017.

[172] N. Watari and R. G. Larson. Shear-induced chiral migration of particles with anisotropic rigidity. *Phys. Rev. lett.*, 102:246001, Jun 2009.

[173] P. Talkner, G.-L. Ingold, and P. Hnggi. Transport of flexible chiral objects in a uniform shear flow. *New Journal of Physics*, 14(7):073006, 2012.

[174] R. Johnson. Flagellar hydrodynamics. A comparison between resistive-force theory and slender-body theory. *Biophysical Journal*, 25:113–127, January 1979.

[175] J. E. Raz, O.)and Avron. Swimming, pumping and gliding at low reynolds numbers. *New Journal of Physics*, 9(12):437, 2007.

[176] B Rodenborn, C. H. Chen, H. L. Swinney, B. Liu, and H. P. Zhang. Propulsion of microorganisms by a helical flagellum. *Proceedings of the National Academy of Sciences*, 110(5):E338–E347, 2013. ISSN 0027-8424.

[177] Marcos, H. C. Fu, T. R. Powers, and R. Stocker. Bacterial rheotaxis. *Proceedings of the National Academy of Sciences*, 109(13):4780–4785, 2012. ISSN 0027-8424.

[178] R. G. Winkler, K. Mussawisade, M. Ripoll, and G. Gompper. Rod-like colloids and polymers in shear flow: amulti-particle-collision dynamics study. *Journal of Physics: Condensed Matter*, 16(38):S3941, 2004.

[179] R. G. Larson. The structure and rheology of complex fluids (topics in chemical engineering). *Oxford University Press, New York Oxford*, 86:108, 1999.

[180] H. A. Stone. Dynamics of drop deformation and breakup in viscous fluids. *Annual Review of Fluid Mechanics*, 26(1):65–102, 1994.

[181] D. E. Smith, H. P. Babcock, and S. Chu. Single-polymer dynamics in steady shear flow. *Science*, 283(5408):1724–1727, 1999. ISSN 0036-8075.

[182] S. Gerashchenko and V. Steinberg. Statistics of tumbling of a single polymer molecule in shear flow. *Phys. Rev. lett.*, 96:038304, 2006.

[183] S. E. Spagnolie and E. Lauga. Hydrodynamics of self-propulsion near a boundary: predictions and accuracy of far-field approximations. *Journal of Fluid Mechanics*, 700:105–147, 2012.

[184] S. Bianchi, F. Saglimbeni, and R. Di Leonardo. Holographic imaging reveals the mechanism of wall entrapment in swimming bacteria. *Phys. Rev. X*, 7(1):011010, 2017.

[185] T. Xu, H. Yu, H. Zhang, C-I Vong, and L Zhang. Morphologies and swimming characteristics of rotating magnetic swimmers with soft tails at low reynolds numbers. In *Intelligent Robots and Systems (IROS), 2015 IEEE/RSJ International Conference on*, pages 1385–1390. IEEE, 2015.

[186] J. W. Shaevitz, J. Y. Lee, and D. A. Fletcher. Spiroplasma swim by a processive change in body helicity. *Cell*, 122(6):941–945, 2005.

[187] W. Ko, S. Lim, W. Lee, Y. Kim, H. C Berg, and C. S. Peskin. Modeling polymorphic transformation of rotating bacterial flagella in a viscous fluid. *Phys. Rev. E*, 95(6):063106, 2017.

[188] G. Rosser, R. E. Baker, J. P. Armitage, and A. G. Fletcher. Modelling and analysis of bacterial tracks suggest an active reorientation mechanism in rhodobacter sphaeroides. *Journal of The Royal Society Interface*, 11(97):20140320, 2014.

[189] C. Li, A. Motaleb, M. Sal, S. F. Goldstein, and N. W. Charon. Spirochete periplasmic flagella and motility. *Journal of molecular microbiology and biotechnology*, 2 (4):345–354, 2000.

[190] S. Jung, K. Mareck, L. Fauci, and M. J. Shelley. Rotational dynamics of a superhelix towed in a stokes fluid. *Physics of Fluids*, 19(10):103105, 2007.

[191] H. Wada and R. R. Netz. Model for self-propulsive helical filaments: kink-pair propagation. *Phys. Rev. lett.*, 99(10):108102, 2007.

[192] B. J. Williams, S. V. Anand, J. Rajagopalan, and M. T. A Saif. A self-propelled biohybrid swimmer at low reynolds number. *Nature communications*, 5:3081, 2014.

[193] H. Zhang, A. Mourran, and M. Moller. Dynamic switching of helical microgel ribbons. *Nano Letters*, 17(3):2010–2014, 2017.

[194] J. G. Shoesmith. The measurement of bacterial motility. *Microbiology*, 22(2): 528–535, 1960.

[195] W. R. Schneider and R. N. Doetsch. Effect of viscosity on bacterial motility. *Journal of Bacteriology*, 117(2):696–701, 1974.

[196] G. E. Kaiser and R. N. Doetsch. Enhanced translational motion of leptospira in viscous environments. *Nature*, 255:656–657, 1975.

[197] A. Klitorinos, P. Noble, R. Siboo, and E. C. S. Chan. Viscosity-dependent locomotion of oral spirochetes. *Oral microbiology and immunology*, 8(4):242–244, 1993.

[198] S. Nakamura, Y. Adachi, T. Goto, and Y. Magariyama. Improvement in motion efficiency of the spirochete brachyspira pilosicoli in viscous environments. *Biophysical journal*, 90(8):3019–3026, 2006.

[199] J. Pande, L. Merchant, T. Krüger, J. Harting, and A. S. Smith. Setting the pace of microswimmers: when increasing viscosity speeds up self-propulsion. *New Journal of Physics*, 19(5):053024, 2017.

[200] W. Foissner. An updated compilation of world soil ciliates (protozoa, ciliophora), with ecological notes, new records, and descriptions of new species. *European Journal of Protistology*, 34(2):195–235, 1998.

[201] V. Kantsler, J. Dunkel, M. Polin, and R. E. Goldstein. Ciliary contact interactions dominate surface scattering of swimming eukaryotes. *Proceedings of the National Academy of Sciences*, 110(4):1187–1192, 2013. ISSN 0027-8424.

[202] L. Zhu, E. Lauga, and L. Brandt. Low-reynolds-number swimming in a capillary tube. *Journal of Fluid Mechanics*, 726:285–311, 2013.

[203] R. Ledesma-Aguilar and J. M. Yeomans. Enhanced motility of a microswimmer in rigid and elastic confinement. *Phys. Rev. lett.*, 111(13):138101, 2013.

[204] E Lauga and T. R. Powers. The hydrodynamics of swimming microorganisms. *Reports on Progress in Physics*, 72(9):096601, 2009.

[205] E. Lauga, W. R. DiLuzio, G. M. Whitesides, and H. A. Stone. Swimming in circles: motion of bacteria near solid boundaries. *Biophysical journal*, 90(2):400–412, 2006.

[206] H. O. Caldag, A. Acemoglu, and S. Yesilyurt. Experimental characterization of helical swimming trajectories in circular channels. *Microfluidics and Nanofluidics*, 21(8):136, 2017.

Acknowledgements

First of all, I would like to acknowledge Prof. Dr. Gerhard Gompper, Prof. Dr. Jan K. G. Dhont, and Dr. Marisol Ripoll for the enjoyable time working under their supervision. I am grateful for the countless hours of helpful advise and discussions, their constructive suggestions, and their endless patience. Furthermore, I would like to thank Prof. Dr. Matthias Sperl and Prof. Dr. Ulrich Deiters for being my defense committee members and their valuable time spent on reviewing my thesis.

I thank my colleagues at the Forschungszentrum Jülich for all the stimulating discussions and the precious moments we shared during, but also outside of work. A special thanks goes to Dr. Zihan Tan, Dr. Kai Qi, Dr. Sebastian Rode for their helpful suggestions and discussions. I like to thank Christian Phillip and Andrea Bräutigam for their help on the German abstract. Moreover, I would like to thank Prof. Dr. Christian Clasen, Prof. Dr. Zeger Hans, and Dr. Naveen Reddy for the excellent collaboration during the project of quantum dots. Moreover, I thank Frau Meike Kleinen and Frau Roswitha Gielen for their help in my living in Germany. Furthermore, I deeply acknowledge my officemates Sebastian Rode, Rapheal hornung, Nirmalendu Ganai, Debarati Sarkar for the many hours together: chatting, discussing, but most importantly, the always friendly atmosphere.

Last but not least, I'm deeply grateful to Horizon 2020 project under the DiStruc Marie Sklodowska Curie innovative training network (grant agree ment no. 641839), which provids funding to support my first 3-years study. I'd like to acknowledge the coordinator Prof. Dr. Dirk Aarts in Oxford university, other supervisors and fellows in this netwrok for their generous help, comments and suggestions on my work.

Eigenhändigkeitserklärung

Ich versichere, dass ich die von mir vorgelegte Dissertation selbständig angefertigt, die benutzten Quellen und Hilfsmittel vollständig angegeben und die Stellen der Arbeit − einschlieβlich Tabellen, Karten und Abbildungen − , die anderen Werken im Wortlaut oder dem Sinn nach entnommen sind, in jedem Einzelfall als Entlehnung kenntlich gemacht habe; dass diese Dissertation noch keiner anderen Fakultat oder Universität zur Prüfung vorgelegen hat; dass sie − abgesehen von unten angegebenen Teilpublikationen − noch nicht veröffentlicht worden ist, sowie, dass ich eine solche Veröffentlichung vor Abschluss des Promotionsverfahrens nicht vornehmen werde. Die Bestimmungen der Promotionsordnung sind mir bekannt. Die von mir vorgelegte Dissertation ist von Prof. Dr. Gerhard Gompper und Dr. Marisol Ripoll betreut worden.

(Ort, Datum) (Unterschrift)

Teilpublikation

Run Li, Marisol Ripoll, Naveen Reddy, Jan K.G. Dhont, Ruben Dierick, Zeger Hens, and Christian Clasen. Tumbling of Quantum Dots: Rheo-Optics. *Langmuir* 2018 34 (48), 14633-14642